DETECTION, SOURCE LOCATION, AND ANALYSIS OF VOLCANO INFRASOUND

By

Kathleen F. McKee, M.S.

A Dissertation Submitted in Partial Fulfillment of the Requirements

for the Degree of

Doctor of Philosophy

in

Geophysics

University of Alaska Fairbanks

December 2017

APPROVED:

Dr. David Fee, Committee Chair
Dr. Matthew Haney, Committee Member
Dr. Curt Szuberla, Committee Member
Dr. Carl Tape, Committee Member
Dr. Michael West, Committee Member
Dr. Paul McCarthy, Chair
Department of Geosciences
Dr. Paul Layer, Dean
College of Natural Science and Mathematics
Dr. Michael Castellini, Dean
Graduate School

Abstract

The study of volcano infrasound focuses on low frequency sound from volcanoes, how volcanic processes produce it, and the path it travels from the source to our receivers. In this dissertation we focus on detecting, locating, and analyzing infrasound from a number of different volcanoes using a variety of analysis techniques. These works will help inform future volcano monitoring using infrasound with respect to infrasonic source location, signal characterization, volatile flux estimation, and back-azimuth to source determination.

Source location is an important component of the study of volcano infrasound and in its application to volcano monitoring. Semblance is a forward grid search technique and common source location method in infrasound studies as well as seismology. We evaluated the effectiveness of semblance in the presence of significant topographic features for explosions of Sakurajima Volcano, Japan, while taking into account temperature and wind variations. We show that topographic obstacles at Sakurajima cause a semblance source location offset of ~360-420 m to the northeast of the actual source location. In addition, we found despite the consistent offset in source location semblance can still be a useful tool for determining periods of volcanic activity.

Infrasonic signal characterization follows signal detection and source location in volcano monitoring in that it informs us of the type of volcanic activity detected. In large volcanic eruptions the lowermost portion of the eruption column is momentum-driven and termed the volcanic jet or gas-thrust zone. This turbulent fluid-flow perturbs the atmosphere and produces a sound similar to that of jet and rocket engines, known as jet noise. We deployed an array of infrasound sensors near an accessible, less hazardous, fumarolic jet at Aso Volcano, Japan as an analogue to large, violent volcanic eruption jets. We recorded volcanic jet noise at 57.6° from vertical, a recording angle not normally feasible in volcanic environments. The fumarolic jet noise was found to have a sustained, low amplitude signal with a spectral peak between 7-10 Hz. From thermal imagery we measure the jet temperature (~260 °C) and estimate the jet diameter (~2.5 m). From the estimated jet diameter, an assumed Strouhal number of 0.19, and the jet noise peak frequency, we estimated the jet velocity to be ~79 – 132 m/s. We used published gas data to

then estimate the volatile flux at ~160 – 270 kg/s (14,000 – 23,000 t/d). These estimates are typically difficult to obtain in volcanic environments, but provide valuable information on the eruption.

At regional and global length scales we use infrasound arrays to detect signals and determine their source back-azimuths. A ground-coupled airwave (GCA) occurs when an incident acoustic pressure wave encounters the Earth's surface and part of the energy of the wave is transferred to the ground. GCAs are commonly observed from sources such as volcanic eruptions, bolides, meteors, and explosions. They have been observed to have retrograde particle motion. When recorded on collocated seismo-acoustic sensors, the phase between the infrasound and seismic signals is 90°. If the sensors are separated wind noise is usually incoherent and an additional phase is added due to the sensor separation. We utilized the additional phase and the characteristic particle motion to determine a unique back-azimuth solution to an acoustic source. The additional phase will be different depending on the direction from which a wave arrives. Our technique was tested using synthetic seismo-acoustic data from a coupled Earth-atmosphere 3D finite difference code and then applied to two well-constrained datasets: Mount St. Helens, USA, and Mount Pagan, Commonwealth of the Northern Mariana Islands Volcanoes. The results from our method are within ~<1° - 5° of the actual and traditional infrasound array processing determined back-azimuths. Ours is a new method to detect and determine the back-azimuth to infrasonic signals, which will be useful when financial and spatial resources are limited.

Table of Contents

List of Figures

Page

List of Tables

Page

Acknowledgments

This dissertation documents four years of hard work, but it would not have been possible without the support of many different people. First and foremost, I thank my advisor, David Fee, for the opportunity to earn my PhD with him, for the guidance, funding, fieldwork, conference travel, weekly meetings, impromptu meetings, listening ear, emails, edits, encouragement, having my back, being gracious when I pushed back, knowledge, support, and time. Thank you to my committee members, Matt Haney, Curt Szuberla, Carl Tape and Mike West for your feedback, time and meeting attendance. Special thanks to Mike for telling me what I needed to hear after I passed my comprehensive exams. I was getting signatures and feeling like I was going to collapse and he said, "We don't pass everyone, we conditional pass plenty of people. You passed. Hold your head up high. You're a PhD candidate."

Thank you to my coauthors Akihiko Yokoo, Colin Rowell, Robin Matoza, Keehoon Kim, Matt Haney and John Lyons for your thoughtful comments, suggestions, edits and feedback. Special thank you to Matt and his family for hosting me while I worked with Matt in Anchorage my first summer. Thank you to Yokoo-san for hosting me at the Aso Volcanological Laboratory for a summer to conduct fieldwork and research at Aso Volcano.

Thank you, thank you, thank you to my parents for putting me in preschool science, soccer, dance, swim team, and science camps. Thank you to my Mother for being my Girl Scout Leader for twelve years and making that program an amazing, empowering experience that encouraged exploration, leadership, service, and self-reliance. Thank you for kicking me out the door and then continuing to support me when I was running out the door farther and farther away from home. Thank you for making sure that I knew from an early age that I could do and be whatever I wanted if I set my mind to it and worked hard. For making me try new things even when I did not want to, so that now trying new things is second nature.

Thank you to my brothers for their continued love and support. For being curious about what I do, for always asking, "Which volcano is yours?" and bragging to their friends about me. You've always made me feel cool even though for many years my peers definitely thought otherwise.

Thank you to John Lyons and Cara Shonsey, who I regularly refer to as my Anchorage friends. Your friendship and support during our shared days at Michigan Tech, through my Peace Corps service and now Alaska has meant the world to me, helped me through hard times and made the good times great. Your company and spare room have provided a refuge for me over the years. Thank you for including me on some of your Alaska adventures. Thank you to John for all the shop talk and to Cara for all the non-shop talk!

Thank you to Sarah Albert for being a partner in crime through classes, homework, ASRA, and an all-nighter, and being advisees of David Fee. Thank you for the encouragement and never doubting. Thank you for listening and for running with me!

Thank you Amanda Lindoo for your friendship and teaching me the ways of Fairbanks and an arctic winter. An extra special thank you for visiting the DMV multiple times to help me get my car registered before having met me!

Thank you to Christina Carr for strongly encouraging Sarah and I to start running and to run in the Beat Beethoven Race. Thank you to all the women who have run with me over the years: Christina Carr, Sarah Albert, Amanda Lindoo, Cassandra Dahl, Kimber DeGrandpre, Demi Mixon, April Knox, Shanshan Li, Emilie Sinkler, Jessie Turner, Megan O'Sadnick, Qingping Yu, Helena Buurman, Annie Wordan, Wenyu Gong, Molly Staats, Cara Shonsey, Sara Dykstra and Portia Collette!

Thank you to my fellow grad students and friends for the quick, "Hi, how are you?", for the long conversations about the meaningful and trivial, for never doubting, for commiserating, for perspective, for the Sunday afternoon 'Craft Beer', for the summertime Cheats, for the hikes, for rock climbing and cross-country skiing outings, for brunches and bonfires, for fishing and berry picking and for all the times in between.

Lastly, thank you to my previous advisors: Bryan Tapp and Greg Waite. Thank you for your time, geoscience and life lessons, encouragement, and recommendation letters. Your advisement prepared me to be successful for the next step. Thank you!

This dissertation is comprised of three manuscripts for which I am the first author. I conducted the majority of the research, data analysis, interpretation, and writing for each of the papers. For McKee et al. (2014), I participated in the data collection effort at Sakurajima Volcano, Japan. I led the data collection at Aso Volcano, Japan with help from my host scientist and coauthor, Akihiko Yokoo (McKee et al., 2017). John Lyons contributed data from Pagan Volcano and Robin Matoza and David Fee contributed data from Mount St. Helens for McKee et al. (submitted). David Fee, Akihiko Yokoo, Colin Rowell, Robin Matoza, Keehoon Kim, Matthew Haney, and John Lyons read the manuscripts and contributed edits and constructive criticism.

Chapter 1

General Introduction

My overall research interest is to improve our understanding of volcanic systems and detection of activity to improve monitoring capabilities using infrasound and seismic data. My master's thesis focused on seismic noise observations of volcanoes and my doctoral work on infrasonic detection and characterization of volcanic activity. From here, my postdoctoral research will be a seismo-acoustic examination of Stromboli Volcano's system. Simply put, I study volcano acoustics, the science of volcanic sound. More often than not, that sound is below human hearing, termed volcanic infrasound.

1.1 Infrasound

Infrasound is low frequency sound below the audible limit of ~20 Hz. It is a mechanical/pressure wave that travels at the speed of sound, usually around 343 m/s through the atmosphere. The speed of sound varies with air temperature and wind speed. Perturbing the atmosphere produces infrasound like dropping a stone in water creates ripples on the surface and through the water below. A variety of natural and anthropogenic sources produce infrasound, and examples include, but are not limited to, aurorae, oceans, winds, volcanoes, thunderstorms, meteors, bolides, explosions, vigorously closed doors, rockets and jet engines, satellite reentries, and cities. Infrasound parallels seismology in its use as a monitoring tool and geophysical method for improved understanding of volcanic processes. An explosive source near the surface, be it volcanic or otherwise, will radiate energy through the atmosphere as a sound wave and through the Earth as a seismic wave. We use microphones sensitive to low frequency sound to record the pressure changes as infrasonic waves pass by. Sound speed increases with increases in air temperature. Wind changes the speed of sound relative to the velocity of the wind. We refer to the speed of sound plus the wind velocity as the effective sound speed. If the wind is blowing in the same direction the sound wave is propagating, then the wind speed increases the speed of the sound wave. If it is perpendicular then it has no effect on the sound speed and if it is blowing in

the opposite direction then it decreases it. While the effective sound speed is unchanged by a perpendicular wind vector, sound propagation direction can change toward the direction a perpendicular wind is blowing (Fee et al., 2011).

As air temperature and wind speed govern the speed at which acoustic waves travel, changes in temperature and wind speed alter the wave's path. A simple source, a monopole, radiates sound equally in all directions such that the pressure is strictly a function of distance from the source (Russell et al., 1999). Additional sources with decreasing sound radiation efficiency are the dipole and quadrupole. A dipole is comprised of two equal-strength monopoles with opposite phase and separated by a small distance and in the same manner a quadrupole is comprised of two identical dipoles (Russell et al., 1999). For a single monopole source, there is a net injection of fluid that produces sounds. For a dipole, there is not a net injection of fluid, rather the movement of fluid back and forth between the sources exerting a force on the fluid and ultimately radiates energy as sound. As such, a dipole does not radiate sound equally in all directions; the pressure has a radial and angular dependence (Russell et al., 1999). For a quadrupole source, there is neither a net injection of nor a net force on the fluid; sound is produced by the fluctuating stress on the fluid. There are two types of quadrupoles, lateral and longitudinal, and these are defined by the arrangement of the dipoles. For a lateral quadrupole the dipoles are parallel and for longitudinal they are in series. As follows, the two different types have two different radiation patterns, both of which are angularly dependent. The lateral quadrupole radiation pattern has four equal lobes and four planes in which no sound radiates. The radiation pattern for the longitudinal quadrupole is similar to that of a dipole (Russell et al., 1999). How sound propagates farther afield is generally predicted by Snell's Law. Snell's law describes the angle at which a wave will be transmitted (pass through), reflected (bounce off) or refracted (bend) when it encounters a medium with a different sound speed. This change in sound speed can be abrupt (i.e. atmosphere to earth) or gradual (i.e. temperature change with altitude).

Earth's atmospheric layers are defined by their temperature gradients (Fee and Matoza, 2013). From Earth's surface upward, the first layer is the troposphere from the surface to ~7-17 km height which has decreasing temperature and in turn sound speed with height. Next is the

stratosphere, ~7-17 to 50 km height, with increasing temperature with height. These layers are followed by the mesosphere (~50 to ~85 km), which has decreasing temperature with height and the thermosphere (~85 to 350-800 km), which has increasing temperature with height. The final layer is the exosphere from 350-800 to 10,000 km, but due to significant attenuation above ~140 km it is not relevant to infrasound studies. Attenuation is the loss of acoustic energy due to geometric spreading and absorption (Cowan, 2014; Pierce, 2014). If a wave propagates away from its source and encounters an atmosphere at a higher temperature and thus sound speed (such as near the top of the stratosphere) than that near the source, then it will refract back down toward Earth's surface (Fee and Matoza, 2013). The refraction at the stratopause, top of the stratosphere where the temperature gradient changes from increasing to decreasing temperatures with altitude, and/or mesopause, top of the mesosphere, and subsequent reflection off the ground creates a waveguide. This, along with low attenuation of low frequency sound waves, allows infrasound waves to propagate great distances. We generally describe the distance traveled by an infrasonic wave with three terms: local, regional, and global. Local infrasound has traveled <~15 km, regional has traveled between ~15 km and ~250 km, and global infrasound >~250 km (Fee and Matoza, 2013). The work herein is focused around local infrasound and therefore the recorded waveforms are more influenced by local topographic features than by global scale propagation paths.

An unintended, but recurring theme throughout this dissertation is the interaction between infrasound waves and the ground surface. When an infrasound wave encounters the ground or a topographic feature, such as a mountain peak or crater wall, some of the energy will diffract around the obstacle, some of it will reflect off it and some of it will be transmitted to the ground. In the case that a wave diffracts around an obstacle it will increase the travel time from the source to the receiver as the path has been lengthened. The waveform's shape and spectral content will also likely be altered (Kim and Lees, 2011; Lacanna and Ripepe, 2013). When the wave reflects off a topographic obstacle, this can add complexity to the waveform as reflections may add additional arrivals and/or amplify the acoustic energy opposite the obstacle as it focuses the waves in that direction (Kim et al., 2012). Today numerical modeling of wave diffraction around a volcanic crater rim (Kim and Lees, 2011) and along the propagation path (Kim and Lees, 2014) is used to account for topographic path effects. The angle in which the wave contacts

the surface and the velocity contrast between the atmosphere and ground dictates how the wave will be reflected, refracted and transmitted. In the case the wave is transmitted, it couples to the ground and can propagate as a seismic wave. If it encounters the ground at near vertical it can trigger a compressional seismic wave (P-wave) (Tauzin et al., 2013) or at near horizontal it can couple and have retrograde particle motion, known as a ground-coupled airwave (Edwards et al., 2007).

1.2 Volcanoes

Volcanoes are created and volcanic eruptions, in general, are driven by buoyancy, the phenomena where a lower density material experiences an upward force when surrounded by a higher density material in a gravitational field (Parfitt and Wilson, 2008). In Alaska, like many other places around the globe, volcanoes are formed due to an oceanic plate subducting beneath a continental plate, the Pacific and North American plates, respectively. The tectonic plates, whether oceanic (thin and higher density) or continental (thick and lower density) "float" on the mantle. When the water-rich Pacific plate subducts, it brings water and water-rich sediments down with it into the mantle (Perfit and Davidson, 2000; Parfitt and Wilson, 2008). As the plate goes deeper, the pressure and temperature increase. The increased temperature causes the water to be released from the subducting slab into the overlying plate (Fig. 1). An increase in water content causes the melting point of rock to decrease (Asimow, 2000). The added water to the mantle causes it to melt. Molten rock in the subsurface, called magma, is less dense than solid rock and thus it is buoyant and begins to rise. As the magma rises through the mantle and continental crust, the pressure decreases, allowing for some elements to exsolve, or separate, from the magma to create gas bubbles filled with gases such as carbon dioxide, water vapor, and sulfur dioxide (Sparks, 1978; Cashman et al., 2000). This gas-

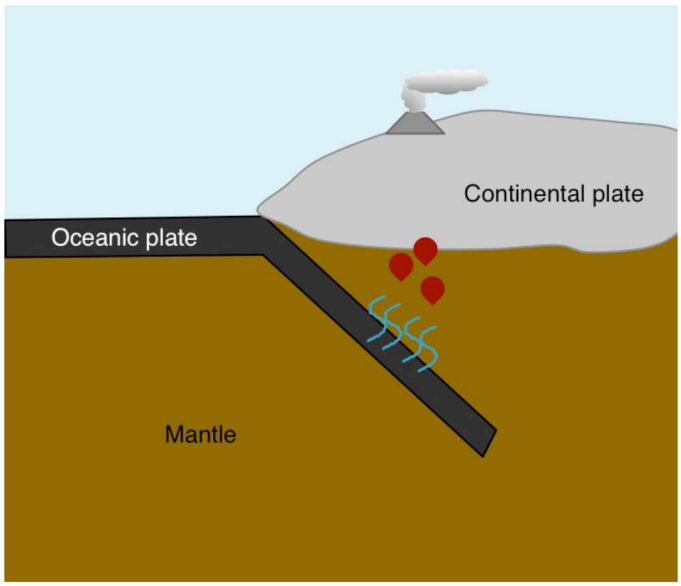

Figure 1 Forming volcanoes in a subduction zone

rich magma is now more buoyant and continues to rise. As it rises the pressure continues to drop thus increasing the number and size of the bubbles further decreasing the magma's density (Gonnermann and Manga, 2007). This process ultimately drives the magma to the surface. When it reaches the surface it effuses passively or erupts, ejecting gas, ash, fragmented rock, blocks, and bombs. This eruptive process occurs at a variety of scales from small explosions lasting seconds and hurling material 10's to 100's of meters into the air, to sustained eruptions lasting minutes to days and thrusting material 10's of kilometers into the atmosphere (Pyle, 2000; Parfitt and Wilson, 2008).

Explosive volcanic eruptions are classified into six different eruptive styles based on their fragmentation and dispersion: Hawaiian, Strombolian, Vulcanian, Sub-Plinian, Plinian, and Ultra-Plinian (Parfitt and Wilson, 2008). Magma composition and its subsequent properties, most notably viscosity and gas content, strongly influence eruption style (Gonnermann and Manga, 2007; Parfitt and Wilson, 2008). Magma viscosity is controlled by volatile content, silica content, temperature, crystal content and gas bubble content. In general, as silica content increases the magma viscosity increases. Magma viscosity changes eruption style by affecting gas bubble mobility and magma rise speed. Bubble ascent slows relative to magma ascent as viscosity increases, which decreases the likelihood of bubble coalescence (Parfitt and Wilson, 2008). Magma rise also slows with increased viscosity. Increased magma rise gives more time for bubbles to rise and coalesce within the magma (Parfitt and Wilson, 2008). Magma gas content influences bubble coalescence; as gas content increases, number density of bubbles and bubble growth increases, which can increase bubble coalescence (Parfitt and Wilson, 2008). In the order listed above, Hawaiian-style eruptions have the least fragmentation and dispersion where Ultra-Plinian have the greatest. The characteristic feature of Hawaiian-style eruptions, named after eruptions observed at Hawaii, is lava fountaining, when molten rock is ejected at speeds of ~100 m/s to heights of tens to hundreds of meters above the vent (Head and Wilson, 1989; Vergniolle and Mangan, 2000; Parfitt and Wilson, 2008). After the lava falls to the ground, it is often still hot enough to coalesce and flow away from the vent for kilometers to tens of kilometers. If the lava has cooled such that it cannot flow, it often builds up a spatter cone around the vent. Strombolian-style eruptions have repeated explosions lasting around 1-2 seconds, which generate small ash plumes hundreds of meters in height and eject bombs

(Blackburn et al., 1976; Vergniolle and Mangan, 2000; Parfitt and Wilson, 2008). Vulcanian and Strombolian style eruptions are similar, but the magmas that feed Vulcanian eruptions usually have higher silica content than Strombolian ones (Morrissey and Mastin, 2000; Parfitt and Wilson, 2008). These explosions last seconds to minutes and with inter-eruptive times lasting tens of minutes to hours. With Vulcanian eruptions, usually the longer repose times lead to more violent explosions. Plinian eruptions, which range from Sub-Plinian to Ultra-Plinian, are named after Pliny the Younger who described the AD 79 eruption of Mount Vesuvius that destroyed Pompeii and Herculaneum (Cioni et al., 2000; Parfitt and Wilson, 2008). The most well known Plinian eruption in the United States is the 1980 Mt. St. Helens eruption. In a Plinian eruption, gas and magma jet from the vent at speeds ranging from 100 m/s to 600 m/s (Parfitt and Wilson, 2008). This jet flow of gas and particles feeds a plume that can rise tens of kilometers above the jet due to convection (Carey and Bursik, 2000; Cioni et al., 2000; Parfitt and Wilson, 2008). Plinian eruptions are subdivided into sub-Plinian, Plinian, and ultra-Plinian by their mass flux and plume heights (Parfitt and Wilson, 2008).

From an infrasound perspective and considering how volcanoes produce sound, these eruptive styles could be categorized on a spectrum with two end members: discrete (short duration) and sustained (long duration). This simple break down of eruptive styles has to do with the distinct difference in waveform characteristics and source processes between discrete and sustained events. Discrete explosions often have similar waveforms from explosion to explosion and from volcano to volcano. The waveforms often look like simple sine waves with a positive pulse followed by an equal rarefaction. The similarities between explosions have become more apparent with increased understanding of and accounting for how topographic features between the source and our receivers influence the acoustic wave (Kim and Lees, 2011; Lacanna and Ripepe, 2013; Kim and Lees, 2014). The two common ways volcanoes produce sound are through expansion of air (e.g. bubble bursts and explosions) and sub- or supersonic flow (e.g. gas jetting and Plinian eruptions) (Rossing, 2014). In the first case, a pocket of hot gas under pressure reaches the surface and expands rapidly. This expansion accelerates the atmosphere creating a pressure wave that moves outward, likely equally in all directions (Buckingham and Garcés, 1996). An explosion is commonly recorded with an impulsive compression followed by an equal rarefaction similar to a sine wave. In the second case, a sustained flow of gas or gas and

particles through a nozzle or vent, termed jet noise, perturbs the atmosphere and creates turbulence, which in turn produces sound (Tam, 1998). A jet noise source has a much more complex, sustained waveform and does not radiate sound equally in all directions. These two ways of producing sound could be considered the end members, as there are examples where discrete explosions are followed by jetting, such as at Halema'uma'u, Karymsky or Santiaguito Volcanoes, and where sustained eruptions have discrete explosions within them (Fee and Matoza, 2013).

1.3 Infrasound as a volcano-monitoring tool

Acoustic or sound waves have been widely studied and used in many fields; here we focus on their application to volcanology and thus infrasound as most of the acoustic energy produced by volcanoes is in the infrasonic band (<20 Hz). Volcano observers utilize both seismic and infrasound waves by looking at frequency content, waveform characteristics, signal duration, recurrence intervals and more to elucidate and monitor volcanic systems. For example, long period earthquakes have specific frequency and waveform characteristics that have been quantitatively linked to fluid migration, such as magma, within the volcanic edifice (Chouet, 1996; Chouet and Matoza, 2013). This is one of the strengths of seismic volcano monitoring. However, seismic networks are limited to specific volcanoes and do not provide global coverage of all active volcanoes. Also, seismic data primarily provide information on subsurface processes, while infrasound informs us about processes at or above the vent.

Infrasound has been shown effective in detecting and locating volcanic eruptions up to thousands of kilometers away (Fee et al., 2010b; Fee and Matoza, 2013; Fee et al., 2013a; Fee et al., 2013b) and therefore, plays a key role in keeping scientists and observers informed of global volcanic activity. Recent efforts in remote infrasound have automated detection and characterization of volcano infrasound (Matoza et al., 2017) and used seismically recorded ground-coupled airwaves (GCAs) to detect and locate volcanic explosions (Fee et al., 2016). GCAs occur when an incident atmospheric acoustic wave encounters the Earth's surface and part of the energy of the wave is transferred to the ground (i.e. coupled to the ground) as a seismic wave (Ben-Menahem and Singh, 2000). Today the Alaska Volcano Observatory (AVO) uses infrasound to aid in monitoring through remote detection of volcanic eruptions (De Angelis et al., 2012). For

example, in the Aleutian Island volcanic arc where limited resources prevent full seismic coverage and the weather limits satellite remote sensing, infrasound can still be used to detect and characterize volcanic activity (Fee et al., 2010b; Fee et al., 2013b). While infrasound continues to prove a useful tool, it has a couple disadvantages. Like seismic data, infrasound is susceptible to wind noise. Unlike seismic waves in the Earth, infrasound travels at the speed of sound in the atmosphere, which means it can take significantly longer for those waveforms to reach deployed sensors. The time between the start of an event and its detection is called latency. The farther a wave travels before it is recorded and detected the higher the signal latency. Unfortunately, detecting activity is not enough to assess the hazard and make decisions about people's safety. For this, we need more detailed, quantitative information on the eruption such as location, eruption style and mass flux. Mass flux, also termed mass eruption rate, is the flow rate of gas and particles exiting a volcano.

The production and subsequent detection of infrasound signals tells us there is activity and the characteristics of the waveforms themselves hold information about eruption style and flux. This relationship needs additional study and validation. As previously mentioned, recent work has shown the contribution of topographic path effects to recorded waveforms (Kim and Lees, 2011; Lacanna and Ripepe, 2013). This contribution complicates interpretation of source processes from waveforms. To address this, Kim et al. (2015) compute numerical Green's functions with a high-resolution digital elevation model by 3D finite-difference time-domain modeling. A Green's function is the component of an infrasonic or seismic record that describes the path the waveform travels (Stein and Wysession, 2003). These Green's functions are then incorporated into an acoustic waveform inversion technique to determine the infrasonic source location (Kim and Lees, 2014) and estimate volume flux (Kim et al., 2015). Estimating eruption volume flux is of particular use as these estimates can be used in plume modeling to estimate plume dynamics and eruption hazards. Recent work has validated infrasound derived eruption flow rate estimates to within an order of magnitude gas and ash measurements at Sakurajima Volcano, Japan (Fee et al., 2017). These advances have been made for Strombolian and Vulcanian style explosions modeled as simple, monopole sources, but further work is needed for more complex acoustic sources such as volcanic jet noise. Recent work has also shown that the spectral content of infrasound recorded from volcanic jet flows, such as from subplinian to plinian eruptions, is

similar to that of manufactured jet flows from jet and rocket engines (Matoza et al., 2009; Fee et al., 2010a; Fee et al., 2010b; Fee et al., 2013a). For a monopole source, sound radiates equally in all directions and as such a sampling of the acoustic wavefield from any point at distance r is equal and can be used to estimate total acoustic power using the power laws from Lighthill (1963). For complicated sources with directional radiation patterns, such as a dipole or quadrupole, more samples of the wavefield are required to estimate total acoustic power. Previous work suggested that the total acoustic power of volcanic jet noise could be estimated by using the power laws (Lighthill, 1952; Woulff and McGetchin, 1976). Recent work has shown this is not the case for jet noise, be it volcanic (Matoza et al., 2013) or artificial (Tam, 1998). Jet noise is directional relative to the jet axis; therefore microphones need to be deployed at many angles relative to the jet axis to better sample the jet noise wavefield. This is a challenge in volcanic jet noise observations as our instruments are deployed at the ground surface. Through many studies of manufactured jet noise, equations relating recorded sound to jet parameter have been empirically derived e.g. (Tam and Burton, 1984; Tam and Chen, 1994; Tam, 1995; Tam et al., 1996; Tam et al., 2008). Matoza et al. (2013) suggest that to derive volcanic jet noise equations or test those derived from artificial jets more field studies and laboratory experiments are needed with simultaneous high-speed visible or infrared imagery and gas observations to independently validate jet parameters. Recent works have used Large Eddy Simulations (Cerminara et al., 2016) and high-speed imagery (Taddeucci et al., 2014) to advance our understanding of volcanic jet flow and noise. Volcanic jet parameter estimation using infrasound, high-speed imagery and other observables would be useful for plume and hazard modeling.

The principal goals of the volcano acoustics community are to 1) detect and locate volcanic activity at local, regional, and global distances, 2) determine type of activity from characteristics of acoustic data, and 3) quantify volcanic emissions using acoustic data to assist with hazard mitigation. The work described herein aids in achieving all three of these goals. Chapter 2 evaluates a local infrasound source location technique in the presence of significant topographic features, which contributes to the first goal. In Chapter 3 we characterize fumarolic jet noise and use infrasound, thermal and gas data to estimate jet velocity and volatile flux. This work aids in the second and third goals. Lastly, Chapter 4 develops a seismo-acoustic technique to detect and characterize ground-coupled airwaves. In addition to contributing to the first goal, this work

provides a possible solution to the challenge of limited resources available for monitoring volcanoes, as it uses less instrumentation than traditional monitoring. This dissertation is laid out in six parts. To begin, an introduction to volcano infrasound was given here, three chapters follow, each detailing my research projects, and finally chapters discussing conclusions and future work.

1.4 Overview of Chapters

1.4.1 Chapter 2: Semblance method at Sakurajima Volcano, Japan

An important step in advancing the science and application of volcano infrasound is improved source location and characterization. Semblance is a commonly used technique for determining both seismic and infrasound source locations at volcanoes. The method uses a grid search in which each unique sensor pair is time-shifted for each grid node, and then cross-correlated to determine which time-shift and respective node provides the best fit. Chapter 2 evaluates the infrasonic source location at Sakurajima Volcano, Japan using the semblance method on data collected in July 2013. The activity at Sakurajima Volcano consisted of strombolian to vulcanian style explosions. Five sensors were deployed in a network configuration (i.e. source is within network or array geometry) around Sakurajima with vent to sensor distances ranging from 2.3 to 6.2 km and a maximum vertical relief across the network of 356 m. All sensors were deployed at elevations below that of the active vent. We investigated semblance in 2D and 3D to assess the necessity of considering 3D sensor and vent locations. Semblance-derived infrasonic source locations showed a clear offset up to ~420 m from the actual vent. To determine the cause of the source location offset we evaluated semblance in multiple frequency bands, as diffraction around topography should be more severe at high frequencies. We also incorporated influences on sound speed such as diurnal temperature variations and wind speed, and tracked changes in the travel time associated with peak semblance over the dataset period. The source location offset is likely the result of significant local topography as the volcanic edifice lies between the vent and the sensor for two stations. This is evidenced by differences in frequency content across the network and consistent travel-time differences. We also found that even though the source location estimate is offset, semblance can also be used to track and characterize volcanic activity, as periods of high semblance correspond to the eruption of ash and gas.

1.4.2 Chapter 3: Jet Noise at Aso Volcano, Japan

In Chapter 3 we work to advance the scientific community's ability to quantify sustained emissions from an active volcanic vent by studying a volcanic fumarole at Aso Volcano, Japan. Quantification of volcanic emissions using sound, particularly in near real-time, would advance gas and ash emission modeling for hazard mitigation. Recent infrasonic observations of sustained volcanic eruptions at Tungurahua Volcano, Ecuador and Mt. St. Helens Volcano, USA showed a similarity in the frequency characteristics between the volcanic eruptions and human-made jet noise, albeit in different frequency bands. This work suggested that volcanoes produce low frequency jet noise, and that we could apply lessons learned from the human-made jet noise research to volcanoes. Jet noise is produced by momentum-driven fluid flow through a nozzle, in particular by shearing the atmosphere and producing turbulence. The human-made jet noise community has derived equations from numerous experiments to determine jet flow parameters (i.e. jet velocity, etc.) from acoustic recordings. One of the challenges in applying the human-made jet noise lessons to volcanoes is that our observations are generally limited to one plane, the ground's surface, where human-made jet noise research samples the acoustic wavefield at many angles relative to the jet axis. Also, large-scale volcanic eruptions do not happen very often, and are dangerous to study up close. Volcanic eruptions are also complex flows of gas and tephra, fine-grained, fragmented volcanic rock (Parfitt and Wilson, 2008). In Chapter 3, we characterize the sound from a gas jetting fumarole within the crater of Aso Volcano. Audible fumaroles have been observed to sound similar to jet engines, but the sounds have not been deeply investigated. Fumaroles are also more frequently active and safer to study. We deployed an array of microphones on Aso's crater rim and recorded days of highly correlated signal. Thermal images were captured and the fumarole sounded like a jet to those in the field. The acoustic data were observed to be low amplitude, broadband and sustained. While the frequency content was broadband, similar to jet noise, the spectral shape had some discrepancies that we infer are likely related to local topography. Modeling of a simple, broadband acoustic source propagating from the fumarole to our sensors suggests near-vent features and the crater wall significantly influence the acoustic wavefield. Using the acoustic and thermal data and an assumed Strouhal number we estimated the fumarolic jet velocity. We then used the estimated jet velocity and previously published gas data to estimate volatile flux. Our volatile flux estimates were similar to those derived using other techniques. This work was funded by an NSF-EAPSI

(East Asia Pacific Summer Institute) fellowship awarded to the author, based on a peer-reviewed proposal.

1.4.3 Chapter 4: Ground-coupled airwave detection and back-azimuth determination method

In Chapter 4 we develop a minimalist infrasonic signal detection and back-azimuth determination technique requiring just one microphone and one three-component seismometer. GCAs are commonly sourced from volcanic eruptions, bolides, meteors and explosions and detected 100s of kilometers away across seismic networks and infrasound arrays. This GCA typically propagates through the subsurface with retrograde particle motion detected on a three-component seismometer (Edwards et al., 2007; Ichihara et al., 2012). When acoustic waves propagate along the surface they excite the ground causing retrograde particle motion in the subsurface and are recorded on a collocated microphone and seismometer. These waves are often coherent and have a 90° phase difference between the two sensors. If the sensors are separated, usually 10s to 100s of meters, then recorded wind noise becomes incoherent relative to wind speed and frequency and an additional phase shift is present due to the separation distance.

We show that determining a unique source back-azimuth is possible using a nearly-collocated, single seismo-acoustic sensor pair by utilizing the coherence, phase difference, and exploiting the characteristic particle motion. The phase difference from 90° depends on the direction the pressure wave arrives from, as each back-azimuth will have a different apparent distance between the sensors. However, the apparent sensor separation determined from the additional phase alone does not provide a unique source azimuth. In turn, we incorporate the particle motion to determine a unique solution. Here we use synthetic seismo-acoustic data generated by a coupled Earth-atmosphere 3D finite difference code to test and tune the detection and back-azimuth determination method. These simulations have the expected high coherence and elliptical retrograde particle motion. The method is then further tested with success using various well-constrained sources (e.g. Mt. Pagan, CNMI and Mt. St. Helens, USA Volcanoes) and existing high signal-noise data (e.g. USGS volcano monitoring networks). The technique developed in Chapter 4 provides a new method to detect infrasound signals and determine their back-azimuth, and would be particularly useful in situations where resources are limited and large sensor networks or arrays are not feasible.

Chapter 2

Network-Based Evaluation of the Infrasonic Source Location at Sakurajima Volcano, Japan[1]

2.1 Introduction

A variety of techniques have been employed to locate seismic and acoustic signals at volcanoes. A common source location method in volcano acoustics at local distances (e.g., <10 km) is semblance, a forward grid-search technique modified for volcano seismic signals by Kawakatsu et al. (2000) and Almendros and Chouet (2003). Other techniques for source location include Bayesian infrasonic source location (Modrak et al., 2010) and time-reversal acoustics (Kim and Lees, 2014). The semblance coefficient, on which this method is based, was first introduced by Neidell and Taner (1971) and defined as a time-domain measure of the coherency (i.e., the similarity) of multichannel data. This method is attractive for volcano acoustic source localization, as it does not rely on a detailed velocity model, which is generally not available around volcanoes. The computation is also straightforward, and the resulting semblance maps provide an intuitive visualization of the source location. Semblance has been applied in 2D and 3D at a number of volcanoes, including Stromboli (Ripepe and Marchetti, 2002; Ripepe et al., 2009), Etna (Montalto et al., 2010; Cannata et al., 2011), Erebus (Jones et al., 2008), Santiaguito (Johnson et al., 2011; Jones and Johnson, 2011), and Karymsky (Rowell et al., 2014). Rowell et al. (2014) also used a time-difference-of-arrival localization method at Karymsky Volcano, with mixed results. At greater distances (e.g., >10 km), localization from back-azimuth cross-bearings from multiple arrays has been an effective technique (Matoza et al., 2011; Johnson et al., 2013) but typically requires accounting for wind and atmospheric structure. In addition to source localization, semblance has also been shown effective at identifying a variety of eruption phenomena (i.e., explosive eruptions, degassing events, and rockfalls) (Johnson et al., 2011). All of the aforementioned methods are often limited by a relatively small number of stations and poor vertical resolution.

---

[1] McKee, K., D. Fee, C. Rowell, and A. Yokoo (2014), Network-Based Evaluation of the Infrasonic Source Location at Sakurajima Volcano, Japan, *Seismological Research Letters*, *85*(6), 1200–1211, doi: 10.1785/0220140119

Here, we apply the semblance technique to locate the acoustic source at the very active Sakurajima Volcano, Japan. Although extensive seismic and acoustic research has been performed at Sakurajima (Iguchi et al., 2008), source localization has not been examined in detail. Sakurajima is well known for repeated Vulcanian explosions that produce high-amplitude infrasound signals, providing an excellent volcano acoustic dataset. Sakurajima also provides an interesting opportunity, as the active crater is not at the summit of the volcano and vent-station propagation paths are obstructed by topography. For comparison, Kim and Lees (2014) utilize the same dataset as we do and apply a time-reversal source imaging technique to back-propagate the acoustic wavefield and locate the acoustic source at Sakurajima Volcano.

2.2 Sakurajima Volcano

Sakurajima Volcano is the island-turned-peninsula due east of the city of Kagoshima on the island Kyushu, Japan (Fig. 2.1a,b). This andesitic stratovolcano has repeating Vulcanian eruptions and makes up part of the southern rim of Aira caldera (Iguchi et al., 2008). In June 2006, Showa crater (denoted by the black triangle in Fig. 2.1b), located downslope and to the east of the summit crater, reactivated after a 58-year hiatus (Yokoo et al., 2013). The transition of activity from the summit to Showa crater was gradual. Initial activity ejected ash hundreds of meters into the air. As activity increased, starting in 2008, explosions produced ash plumes 1–4 km above the crater, with bombs and occasional pyroclastic density currents extending no more that 1.5 km from the crater rim. The activity at Showa crater has been more frequent and of smaller scale than that of the summit crater. Since activity recommenced, Showa crater has expanded in size; it was reported to be 289 m × 375 m in diameter in October 2013 (Japanese Ministry of Land, Infrastructure, Transport, and Tourism, unpublished data).

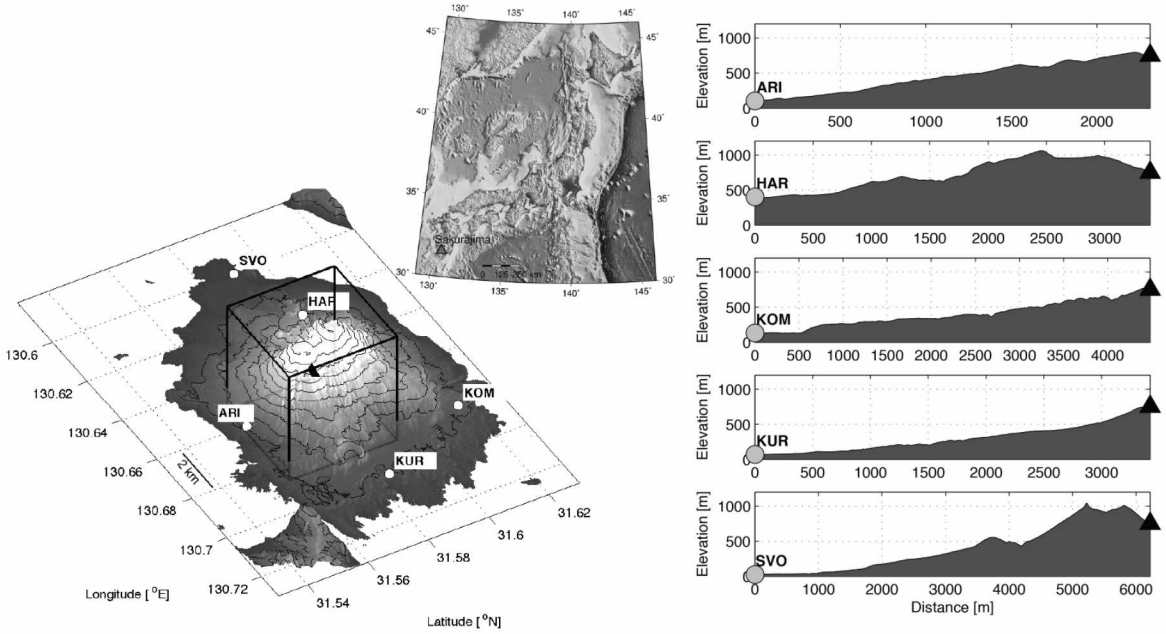

Figure 2.1 Map and Topographic Profiles of Sakurajima Volcano, Japan (a) A map of Japan with Sakurajima Volcano highlighted by the triangle. (b) 3D view of Sakurajima Volcano, with infrasound network station locations denoted by dots and the vent denoted by triangle. The initial search for infrasound sources was within the 2 × 2 × 2 km^3 box. (c) Sensor-to-vent profiles for each network station. Note the significant topographic obstructions present for stations SVO and HAR.

In recent work, Yokoo et al. (2013) used a variety of instruments to improve understanding of the process leading to eruption at Showa crater: tiltmeters and extensometers (ground deformation in strain), visual and infrared thermal cameras (temperature variations), high-sensitivity TV cameras (visual observations), broadband and short-period seismometers with some of the latter situated in boreholes (earthquakes), low-frequency microphones (infrasound waves), and miniature ultraviolet spectrometers (sulfur dioxide [SO_2] emissions). They observed three distinct and repetitive stages leading to and followed by explosions, which we summarize here. Stage 1 starts a few hours prior to eruption (PTE) with the observance of extension in the radial and contraction in the tangential components of strain and occasionally small BH-type earthquakes (i.e., long-period earthquakes with spectral peaks in the 3–8 Hz range), which is interpreted as magma migration within Sakurajima. Stage 2 is marked by several observations in the tens of to a few minutes PTE: a distinct acceleration in strain and tilt in the same regime as stage 1, accompanied by the disappearance of glowing at the crater and a decrease in SO_2 release. The source of these observations is thought to be the sealing of the crater by a lava plug and the subsequent formation of a gas pressure pocket. It is the plugging of the system that builds a pocket of gas, increasing the pressure, thus accelerating the strain and tilt and preventing the

escape of SO_2. Stage 3 commences when the tremor amplitude increases, followed by strain and tilt inversion from radial extension to contraction and tangential contraction to extension and a temperature increase observed with infrared video at a few minutes PTE. Yokoo et al. (2013) suggest the increased tremor amplitude is the result of the plug fracturing by gas pressure exceeding the rock's strength. The fractures allow gas to escape, which causes decompression that propagates down the conduit, resulting in the degassing, expansion, and rising of the magma.

After the three stages, the eruption follows, which consists of an explosion earthquake accompanied by a preceding and main phase infrasound signal. The preceding and main phases of the infrasound are thought to be due to two components of the eruption. First, as the magma expands and rises up the conduit, the resulting pressure and movement pushes the plug upwards, perturbing the atmosphere and resulting in the preceding infrasonic phase. Then, the gas pocket bursts through the plug, launching rock fragments and creating the main phase of the infrasound wave. This two-phase infrasound signal is detailed in Yokoo et al. (2009, 2013) and highlighted in Fee et al. (2014). It is this main phase waveform that is used in the source location method described herein. Shortly following this, fragmentation occurs and an ash-rich volcanic cloud is erupted. This type of activity occurs regularly at Sakurajima.

During the field campaign, discussed in the next section, Sakurajima's activity was similar to that described above and by Yokoo et al. (2013). Vulcanian-style explosions of varying size and duration were accompanied by ash-laden plumes, ash fall, meter-sized blocks, and occasional volcanic lightning. Sometimes the explosions were audible with a thunder-like sound, most notably at station ARI and KUR. For the approximately 34 explosions recorded, the coincident ash-rich plumes ranged from 1.8 to 6.1 km above sea level (Fee et al., 2014). In many cases, these explosions were followed by periods of tremor or jetting on the order of minutes to hours. A notable observation was the lack of infrasound for minutes to hours before the larger explosive events, which was also observed and in turn attributed to vent sealing by Yokoo et al. (2013).

2.3 Field Campaign

On 18 July 2013, we deployed five sensors in a network configuration around Sakurajima as shown in Fig. 2.1b. At ARI, KOM, and SVO, National Center for Physical Acoustics (NCPA)

digital infrasound sensors (DIS) were used; while HAR and KUR used Hyperion IFS-5201 DIS. Both sensor types have self-contained digitizers and Global Positioning System timing clocks and have flat frequency responses between ~0.02 and 250 Hz. The NCPA sensors have a pressure range of ±1190 Pa, whereas the Hyperion sensors have a less dynamic range of ±1000 Pa. Over the nine-day deployment, the NCPA instruments recorded at 250 Hz and the Hyperion sensors recorded at 500 Hz. All the data were later down-sampled to 200 Hz for uniformity. As shown in Fig. 2.1b, the network was deployed below the active vent; the maximum vertical relief across the network was 356.5 m, between sensors HAR and SVO. In addition to the network configuration itself, the topographic profiles in Fig. 2.1c show that in two cases the volcanic edifice is between the active vent and the sensor. The location of Showa crater and nearby topography make Sakurajima an ideal location for evaluating the effectiveness of the semblance method in determining the infrasonic source location in the presence of topography.

2.4 Semblance Source Location

Here, we use semblance to locate the source of infrasound signals at Sakurajima Volcano, Japan. The semblance method is a forward grid search in which the waveforms from a pair of sensors are either evaluated for coherency at each grid node (as in Ripepe and Marchetti, 2002 and Montalto et al., 2010) or the error function is determined for each grid node (as in Johnson et al., 2003 and Jones et al., 2008). The node maximizes coherency or minimizes the error function is assumed as the source. The waveforms are time-aligned, assuming the signal propagates along a straight, unobstructed path between the respective grid node and sensor. Because of the straightforward application of the method, it has been applied in various volcano seismic and acoustic studies. For example, Dawson et al. (2004) used radial semblance to define the shallow magmatic conduit at Kilauea Volcano by locating very-long-period seismic events in near real-time. With infrasound data, Jones and Johnson (2011) were able to locate subevents (different pulses) within an explosion sequence at Santiaguito Volcano, Guatemala, with the semblance method. We apply the semblance method to individual explosive events at Sakurajima, as determined by Fee et al. (2014), as well as to consecutive time windows on the entire dataset.

The semblance calculation that we use follows Rowell et al. (2014), in which the methods of Almendros and Chouet (2003), Ripepe et al. (2007), and Jones and Johnson (2011) are

combined. Almendros and Chouet (2003) calculate a single 3D semblance map by averaging the cross-correlation coefficients for all station pairs. Ripepe et al. (2007) and Jones and Johnson (2011) then incorporated a modification. Instead of calculating semblance for all the channels at once, semblance is evaluated for each unique station pair, producing semblance maps that are then multiplied together for a single map. The benefit of calculating semblance with this modification is that it suppresses side lobes and enhances the maximum semblance (S_m) location. Rowell et al.'s (2014) technique takes these previous methods one step further in using a full 3D source space rather than holding one spatial coordinate constant and calculating semblance over flat grids. The resulting single map is made up of stacked or exponential semblance values Se. For each station pair, the semblance values range from 0.5 for uncorrelated white noise to 1 for perfect coherence. When the station pair maps are stacked for the 10 unique station pairs we have at Sakurajima, the S_e values range from $0.5^{10} = 9.77 \times 10^{-4}$ to $1^{10} = 1$. The infrasonic source location is assumed to be at the location of the peak semblance. Because of the exponential nature of the semblance values we often refer to "adjusted semblance," that is,

$$S_a = e^{\frac{ln(S_m)}{N}}, \tag{2.4.1}$$

to have a more intuitive number. (N is the number of unique station pairs.) Adjusted semblance ranges from 0.5 to 1, the same as the values for a single station pair semblance map.

A variety of influencing parameters need to be accounted for when evaluating infrasonic source location using semblance; these include air temperature, wind, infrasound frequency, grid spacing, and window length. To start, a grid position and volume are established. We begin with a 2.0 km cubic grid (i.e., 8 km^3) centered about the Showa crater of Sakurajima Volcano (Fig. 2.1b). The center point was determined by picking the hottest pixel from the thermal infrared Landsat 8 image (taken in August 2013) and then matching the latitude and longitude with a digital elevation model to find the elevation. We initially chose a 50 m grid-node spacing and later decreased it to 10 m for improved resolution, but for explosive events with peak frequencies between 0.5 and 5 Hz (wavelengths ~680–68 m, respectively), the former is sufficient as it is less than the peak acoustic wavelength (Rowell et al., 2014). Part of the versatility in the

semblance method is that it can be tuned to different frequencies of interest, and in turn the grid-node spacing can be adjusted such that it is less than the peak acoustic wavelength (Rowell et al., 2014). In other words, higher (lower) frequencies require finer (coarser) grid-node spacing for accurate locations. With an established grid the straight-line travel times (*dt*) from each node to each sensor are calculated with respect to current air temperature as the sound speed (*c*) varies with temperature:

$$c = 331.3 + (0.606T), \tag{2.4.2}$$

in which T is temperature in degrees Celsius. Over the nine days of data collected at Sakurajima, the air temperature was recorded at the Japan Meteorological Agency (JMA) station near Kagoshima (11.6 km west-southwest of the crater) every 10 minutes and ranged from 25°C to 35.6°C (mean of 29.7°C). This temperature variation translates to a sound speed variation of 346–353 m/s (mean of 349 m/s). For individual event source location, the most recent temperature within 10 minutes was used to calculate sound speed, but for time-series semblance calculations, we used the average air temperature. We evaluate the effect of different sound speeds on the infrasonic source location in the Results and Discussion section. Wind can also alter sound propagation and can thus influence the acoustic travel time. Here we incorporate wind into *dt* by using the effective sound speed:

$$c_{eff} = c + w, \tag{2.4.3}$$

and

$$w = \mathbf{v}_w \cdot \mathbf{u}, \tag{2.4.4}$$

in which ω is the dot product between $\mathbf{v}_w$, the wind velocity, and $\mathbf{u}$, the unit vector for a given grid node–to–sensor combination. We then compute the effective sound speed for each grid node and sensor path using a 2D wind velocity vector. The wind speed in Kagoshima ranged from 0.3 to 8.1 m/s and varied diurnally, with higher speeds at midday to early afternoon. Wind direction ranged from westerly to northerly, in which "westerly" indicates wind coming from the west and

blowing towards the east. The effect of wind on the infrasonic source location is evaluated for the selected explosive events, and we use the wind speed and direction closest to the explosion time.

Prior to applying the semblance technique, we filter the infrasound data between 0.5 and 5 Hz. This band encompasses the majority of the acoustic energy from Sakurajima without including the energy from the microbarom (Fig. 2.2b). For explosive events, we analyze 30 s data segments starting 3 s before the event times listed in table 2 of Fee et al. (2014). This window length and start time were selected to encompass the majority of the explosion waveform across the network. For the time-series semblance, we also used a 30 s sliding window as in Rowell et al. (2014); however, we used nonoverlapping windows.

The sensor locations are well distributed, with respect to azimuth, around Sakurajima for x (easting) and y (northing) resolution of the source epicenter (Fig. 2.1b) but have little vertical relief between sensors across the network (<10% of network dimensions) (Fig. 2.1c). In addition, all the sensors are below the active vent, which is not uncommon for volcano sensor networks. This network configuration likely results in poor resolution in the vertical component of the source location.

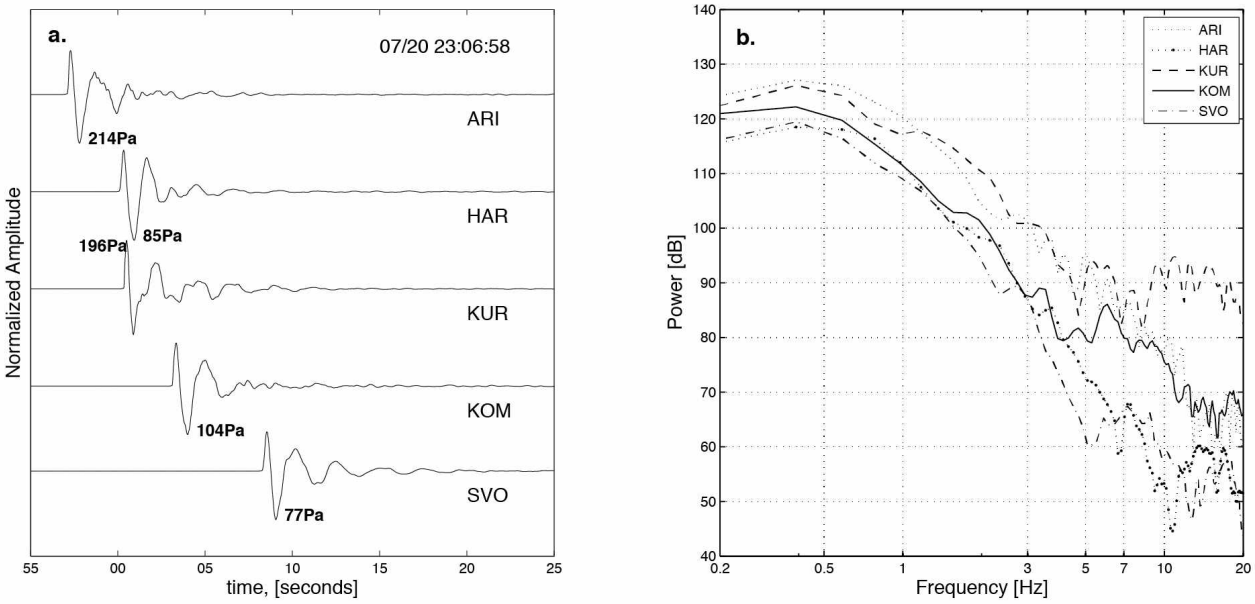

Figure 2.2 Example Waveforms and Spectral Content (a) Normalized waveform from each network station for the explosive event on 20 July 23:06:58 UTC, filtered from 0.5 to 5 Hz. The stated amplitudes are the peak pressures at each station for the event. Waveforms are shown in order of increasing distance from the vent. (b) Power spectral density for the event in Fig. 2.2a.

2.5 Results and Discussion

Our computed semblance source locations have a general offset of ~420 m to the northeast of Showa crater (Fig. 2.3). The locations vary from explosion to explosion by tens of meters, but all have a similar trend. Fig. 2a shows the filtered and normalized waveforms, and Fig. 2.3d shows the source location for one event (7 July 23:06:58; event 11) in the form of a 3D perspective of the three geographic planes: xy (Fig. 2.3a), xz (Fig. 2.3b), and yz (Fig. 2.3c), with x corresponding to east–west and y corresponding to north–south semblance slices. The maximum semblance value is included in each plane and noted by a white star; in plotting, the planes have been scaled such that the nodes with the lowest semblance values are transparent for improved viewing. The peak semblance location for this event is (70x, 60y, 250z) m, and the peak semblance value is 0.48 (corresponding to cross correlation or adjusted semblance value of 0.93). After initial results using the coarse grid showed a general location northeast of the vent, we downsized the grid to x = [−0.2, 0.4] km, y = [−0.2, 0.4] km, and z = [−1, 1] km, in which the vent is located at (0x, 0y, and 0z) km, and decreased the node spacing to 10 m. The average location for all the explosive events using the finer grid and input parameters is approximately (80x, 70y, 10z) m, which is 123 m horizontally out from and ~769 m below the vent (779 meters above sea level [m.a.s.l.]). The average azimuth from the assumed source location to the semblance calculated source location is 47°, and the average straight-line offset (or slant misfit) is 780 m. The first column of Table 2.1 lists the average semblance and location values for the 34 explosive events.

Table 2.1 Semblance location summary for the 34 explosive events with respect to different temperature parameters and wind

	20 C	10 min Mean Temperature 29.7 C	10 minute Variation	10 minute Variation with wind
Adjusted Peak Semblance, Average	0.863 +/- 0.061	0.852 +/- 0.064	0.851 +/- 0.064	0.847 +/- 0.065
Horizontal Misfit, Average [m]	120 +/- 40	130 +/- 40	130 +/- 40	130 +/- 50
Slant Misfit, Average [m]	780 +/- 160	370 +/- 100	360 +/- 110	420 +/- 140
Azimuth, Average	47 +/- 24	67 +/- 26	68 +/- 26	57 +/- 28
Vertical Location, Average [mASL]	10 +/- 170	450 +/- 130	460 +/- 150	410 +/- 210

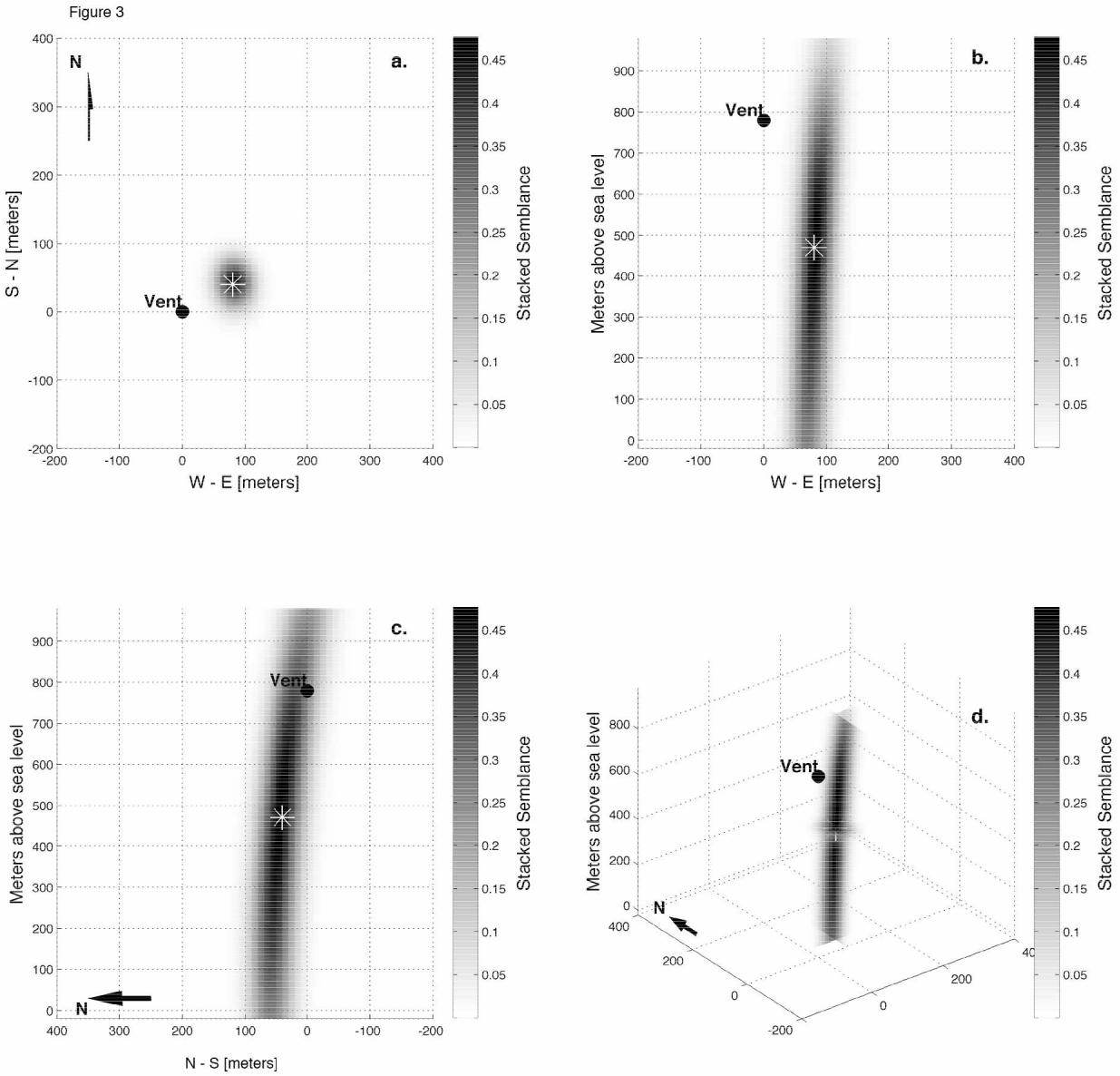

Figure 2.3 Source location and semblance maps for an explosive event on 20 July 23:06:58 UTC. The white star denotes the location of peak semblance in (a) the map view, (b) the east–west and vertical map, (c) the north–south and vertical map, and (d) the 3D perspective of the semblance source location map with the three planes that contain the peak semblance values displayed. Note the semblance values have been transparently scaled such that the lowest values are not visible.

In an effort to improve the source location for the explosions and find the cause of the location offset, we integrated local temperature data to improve estimates of the sound speed. We first determined the location of peak semblance using the average temperature (29.7°C), which corresponds to a sound speed of 349.3 m/s, as shown in Fig. 2.4a (open circles) and listed in Table 2.1. Fig. 2.4a is a 3D perspective of the peak semblance locations for the 34 explosive

events; three locations are plotted for each event, corresponding to the different input temperatures used to calculate sound speed: 20°C, 29.7°C, and current temperature within 10 minutes. Incorporating local temperature data instead of using the generic 20°C improved the average vertical component of the location from 10 to 450 m.a.s.l. (769–329 m below the vent) and the average straight-line distance from 780 to 370 m. In Fig. 2.4, the three source locations for event 28 have been connected by a line to highlight the change in source location, particularly in the vertical, by incorporating local temperature data. The adjusted peak semblance and horizontal distance changed only slightly, as shown in Table 2.1 and Fig. 2.4a. The source location remained offset to the northeast, suggesting the offset is not due to variations in temperature (and hence sound speed).

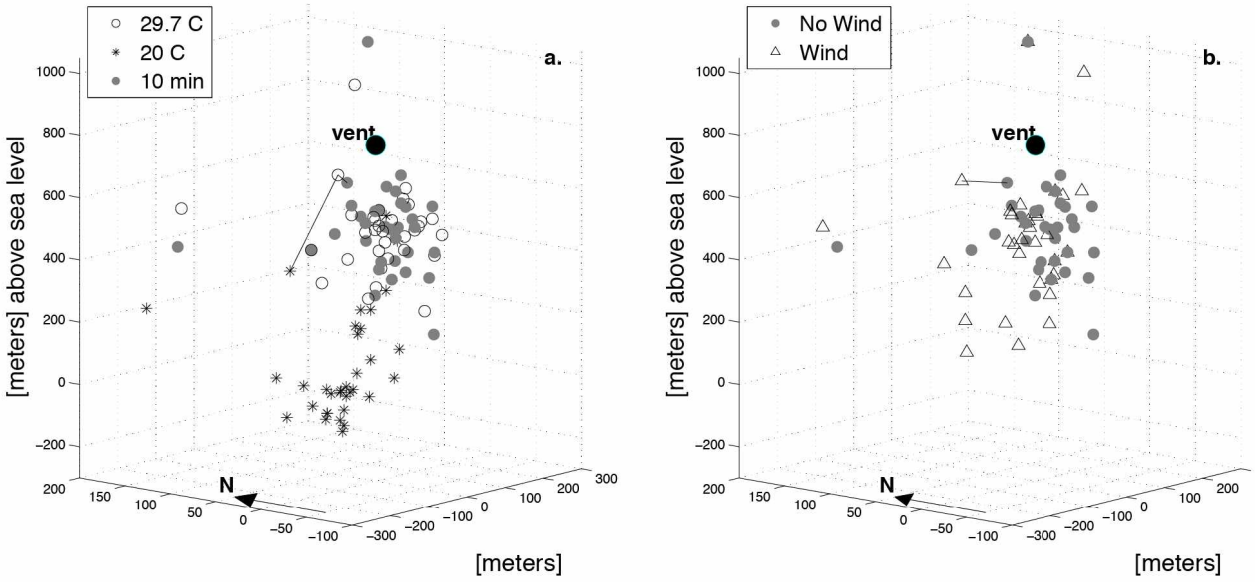

Figure 2.4 Semblance source locations plotted for the 34 explosive events. The large black circle with the gray outline denotes Showa crater. (a) Source locations for various temperature parameters: 20°C (stars), 29.7°C—average temperature (open circles), and 10-minute temperature data (closed circles). (b) The source location comparison between 10-minute temperature data (closed circles) and incorporating 10-minute wind data (open triangles). In both (a) and (b), a single event's source location has been connected by a line to highlight how the location varies after incorporating local temperature and wind data.

Wind speed and direction data from a JMA station in Kagoshima were also incorporated into the semblance location calculation. To evaluate the necessity of including wind data, we first compared semblance locations with the explosive events occurring at times of high and low wind (i.e., daytime and nighttime, respectively, due to natural diurnal wind fluctuations). Fig. 2.5a displays source locations for the 34 explosive events; daytime events are plotted as open circles,

whereas nighttime events are solid circles. The nighttime locations labeled as b, c, and d correspond to the waveforms from station ARI in Fig. 2.5b–d and have adjusted semblance values of 0.86, 0.86, and 0.78, respectively. The seemingly similar conditions (nighttime events suggesting little to no wind and consistent explosive activity from the same vent) and high-semblance values (i.e., high-waveform similarity) would suggest they have similar locations; however, their straight-line distances vary by tens to hundreds of meters: 480, 360, and 310 m, respectively. These variations in the location may be due to a number of factors, such as the inherent uncertainty in the location method, network setup, and variability in the actual source location. The variation in the waveforms for these three events (Fig. 2.5b–d) suggests complex source processes at the vent that may result in differences in the actual source location. The nighttime events are evenly distributed horizontally and vertically in comparison with the daytime events. Because of the ambiguity of this comparison, we incorporated 10-min wind data into the infrasound semblance location calculation. Fig. 2.4b shows the locations for 10 min temperature variation (solid circles) and those that also include 10 minute wind variation (open triangles). The added wind component significantly alters the source location. The event on 19 July 02:19:11 UTC had a corresponding temperature of 32.6°C and was located at (90x, 10y, 650z) m. We incorporate a wind speed of 3.6 m/s with a direction of 315° and the location changes to (10x, 80y, 70z) m. The peak semblance value remained virtually unchanged (0.932 to 0.934), but the straight-line distance from the actual vent changed from 160 to 710 m. For a different event, 20 July 23:21:50 UTC, the addition of wind (1.6 m/s, 67.5°) improves the straight-line offset distance by ~230 m (450 to 220 m). After incorporating wind, the average semblance value changes from 0.851 to 0.847. There are small changes in the average horizontal location, and the average straight-line offset distance drops from 360 to 420 m (Table 2.1 and Fig. 2.4b). The addition of wind into the semblance calculation influences the source location a significant amount, but it does not account for the general offset to the northeast.

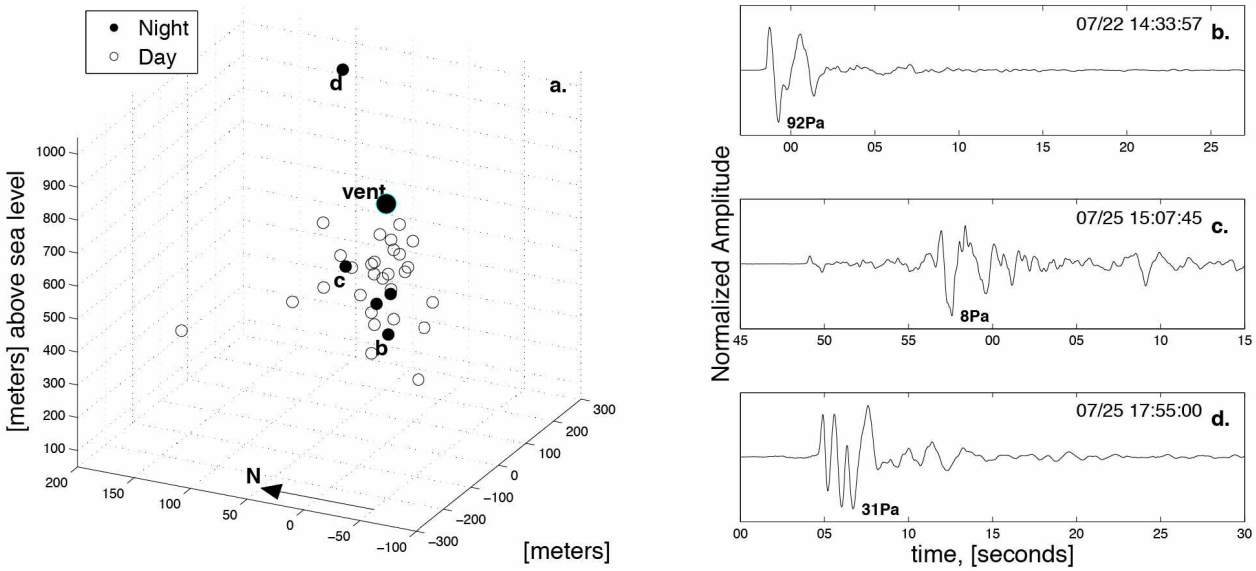

Figure 2.5 Day versus Nighttime Semblance Source Location Results (a) Comparison of the semblance source locations for events that occurred during the day (open circles) and night (closed circles) using 10-min temperature data. (b) Waveforms from three nighttime events; the time is the start of the window, with the time axis in turn being absolute time. The waveforms correspond to the black dots labeled as (b), (c), or (d) in the location plot.

In the travel-time calculation for aligning the waveforms, the assumption is that the sound wave travels in a straight line from the source to the receiver. At Sakurajima Volcano, there are two source–receiver propagation paths (vent to HAR and vent to SVO) that are not line-of-sight due to the volcano summit (Fig. 2.1c). In these cases, the sound wave must diffract around the obstruction to reach the sensors. This diffraction results in the sound energy taking a longer propagation path, resulting in a greater travel time than that assumed in the semblance calculation. To evaluate the travel-time offset for each station, we calculated semblance from 22 to 24 July in 30-s nonoverlapping windows between 0.5 and 5 Hz, with a grid of x = [0, 0.3] km, y = [0, 0.2] km, and z = [−1, 1] km (i.e., a grid spacing of 10 m), and set an adjusted semblance threshold value of 0.7 to eliminate sources other than the volcano. We assumed an air temperature of 29.7°C, a corresponding sound speed of 349.3 m/s, and no wind. The left side of Fig. 2.6 shows the difference between the travel time from the peak semblance location and the straight-line travel time from vent to sensor for each network station. The right side of Fig. 2.6 shows the distribution of travel-time differences for each station. The average positive travel-time differences for stations HAR and SVO are ~0.2 and 0.22 s, respectively, and average negative differences for ARI, KUR, and KOM are ~0.09, 0.53, and 0.32 s, respectively). These consistent, positive and negative time differences reveal the travel time from the source location

to HAR and SVO is longer than the straight-line propagation, whereas it is shorter to KOM and KUR. The travel-time differences are consistent and do not show diurnal variation. This suggests the source of the differences is time invariant, with the obvious cause being topography. The lack of diurnal variation further supports temperature and wind variation as unlikely causes for the northeast location offset.

Diffraction previously was shown to be significant in volcano acoustic scenarios (Kim and Lees, 2011; Lacanna and Ripepe, 2013). Sound waves will diffract around a barrier, such as topographic obstacles, with the amount of the diffraction related to source–receiver position and the relative sizes of the acoustic wavelength and the obstacle. The longer the acoustic wavelength is, the greater proportion of sound that will refract around the obstacles (Hadden and Pierce, 1981; Pierce, 1981). Lower frequency waves should thus be less sensitive to changes in topography. To examine the frequency dependence of diffraction at Sakurajima, we filtered various explosion event waveforms in multiple frequency bands: 0.1–1 Hz, 1–5 Hz, 5–10 Hz, and 10–20 Hz (corresponding to the wavelengths 3493–349.3 m, 349.3–69.8 m, 69.9–34.9 m, and 34.9–17.5 m, respectively, for sound speed of 349.3 m/s at 29.7°C) (Fig. 7). The topographic obstacles between the vent and sensors HAR and SVO are several hundred meters high and several kilometers in length (Fig. 2.1b,c). The scale of this topographic obstacle suggests there should be significant diffraction for the frequencies of interest at Sakurajima. Examination of the explosion signal arrival times reveals they are similar for each individual station and for all the frequency bands of interest. This suggests these frequencies and corresponding wavelengths are all influenced by the topography (i.e., have a similar ray path).

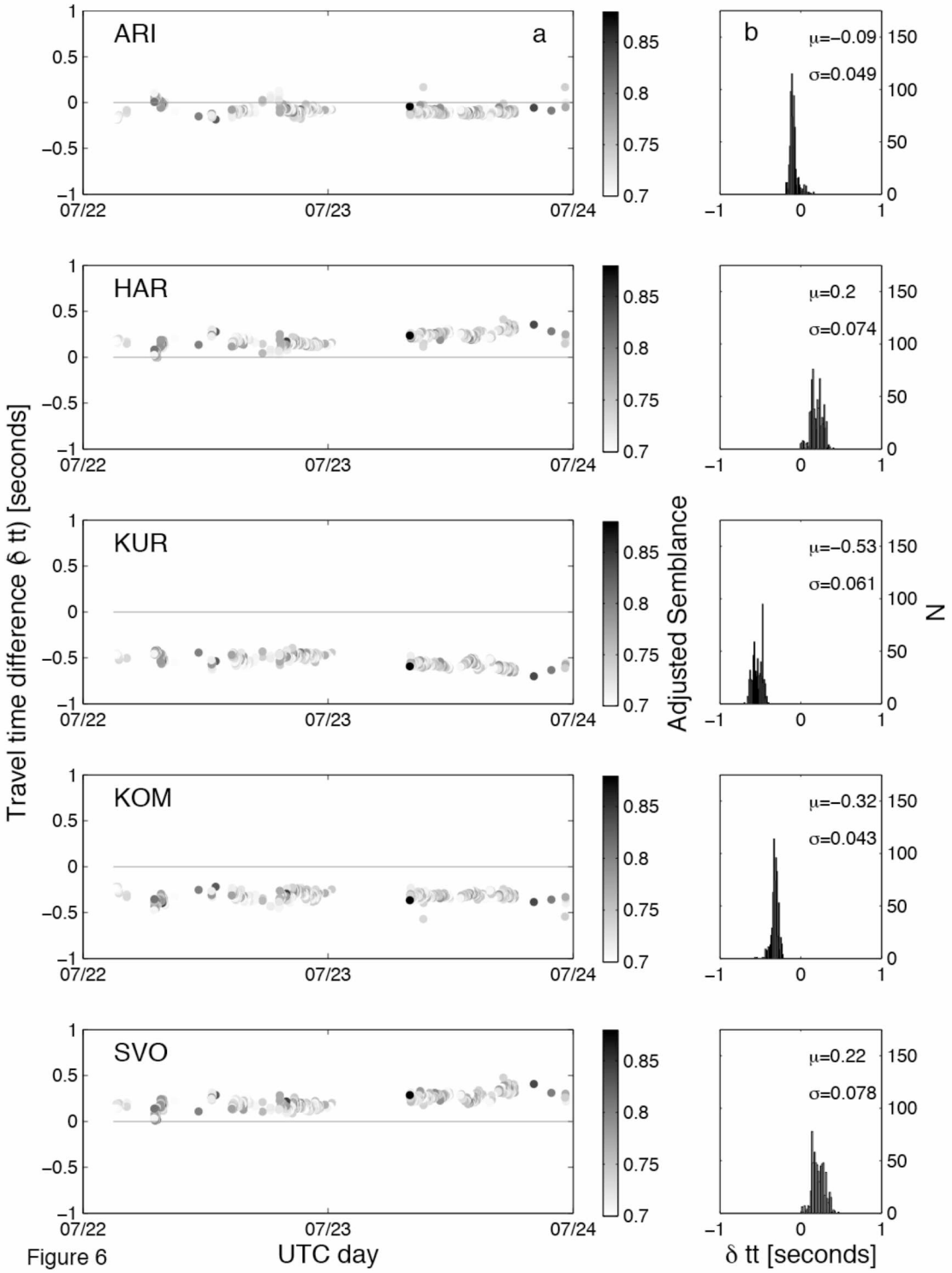

Figure 6

Figure 2.6 Travel Time Comparison: Travel-time difference between the expected source location and the calculated source location for each station. The left column shows the change in relative travel time (travel time found by semblance minus straight line) in seconds for each network station for a two-day period, 22 July 03:00:00–24 July 00:00:00 UTC. The right column is the distribution of the change for each station, where μ is the mean, σ is the standard deviation, and δtt stands for relative change in travel time. N is the number of 30-s windows that semblance was calculated above the threshold.

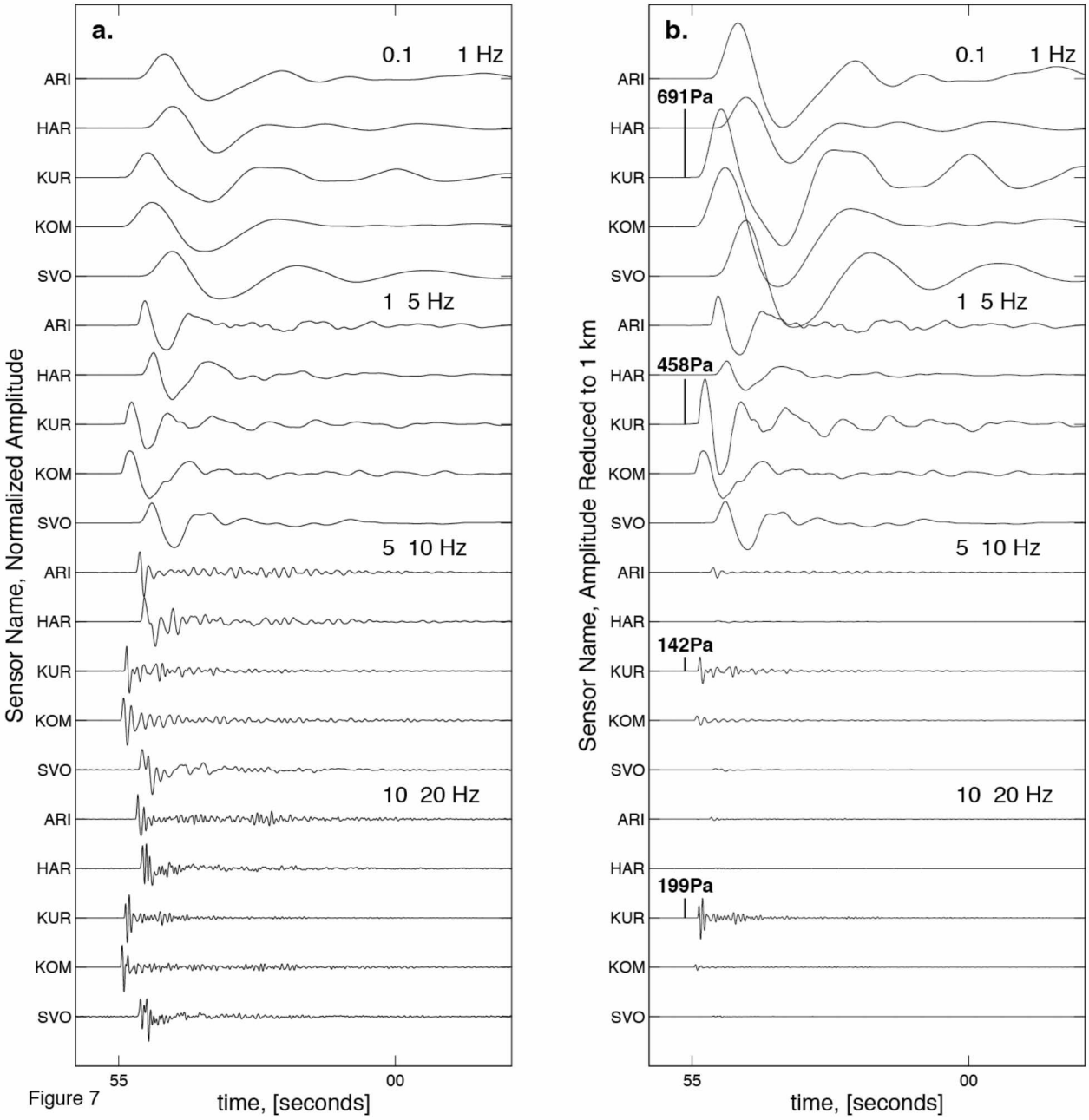

Figure 7

Figure 2.7 Normalized and Reduced Amplitude Waterfall Plots: Waterfall plots of straight-line, time-shifted waveforms for the explosive event on 20 July 23:06:55 in four different frequency bands: (a) amplitude normalized and (b) amplitude reduced to 1 km. The time axes are absolute time.

There is other evidence of diffraction influencing the infrasound signals at Sakurajima, which we discuss here, although more in-depth discussion may be found in Fee et al. (2014), Kim and Lees (2014), and Yokoo et al. (2014). Infrasonic waveforms have been shown to be altered due to diffraction around the crater rim (Kim and Lees, 2011) and topography between the source and receiver (Lacanna and Ripepe, 2013). Fig. 2.2a shows example waveforms from each network

sensor filtered from 0.5 to 5 Hz. We observe greater high-frequency content in the waveforms from ARI and KUR compared with HAR and SVO, which is also present in the power spectral density (Fig. 2.2b). This is clear for an example explosion waveform in Fig. 2.7b, in which we observe significant differences in amplitude at higher frequencies across the network. Fig. 2.7b shows the same frequency bands as Fig. 2.7a, but here the amplitudes have been reduced to 1 km instead of normalized. Varying degrees of reduced rarefaction have also been observed in the Sakurajima waveforms, with stations HAR and SVO being the most significant (Fee et al., 2014), which also suggests the influence of diffraction. Topography or a source located lower in the crater could cause this reduced rarefaction. However, we observe less high-frequency content and a greater rarefaction at stations SVO and HAR, suggesting the topography of Sakurajima summit plays a more significant role in diffracting the infrasound signals.

Although the semblance-derived source location is not very accurate in the presence of significant topography at Sakurajima, semblance itself may still be a useful tool. Johnson et al. (2011) used semblance to detect a variety of eruptive phenomena, even during periods of low signal-to-noise. Fig. 2.8 is a pseudohelicorder plot of 0.5–5 Hz data from station ARI for 23 July, overlain with 30-s nonoverlapping windows of peak semblance near Showa crater using the same parameters and threshold as in Fig. 2.6. The scale used is adjusted semblance from 0.5 to 1, in which 0.5 corresponds to incoherent noise. We observe that times of eruptive activity have high-semblance values whereas times of inactivity (or noise) have low values. This network-derived plot compares well with the pseudohelicorder plot in figure 3 of Fee et al. (2014), where they used small-scale infrasound array data to detect coherent infrasound signals from the active vent. The explosive events at 08:00, 20:08, 21:51, and 23:11 are well picked with high adjusted semblance values: 0.89, 0.87, 0.84, and 0.78, respectively. The longer duration tremor is also highlighted well by semblance with an average adjusted semblance value of 0.75. This suggests semblance can be used as a tool to detect times of volcanic activity even in the presence of significant local topography.

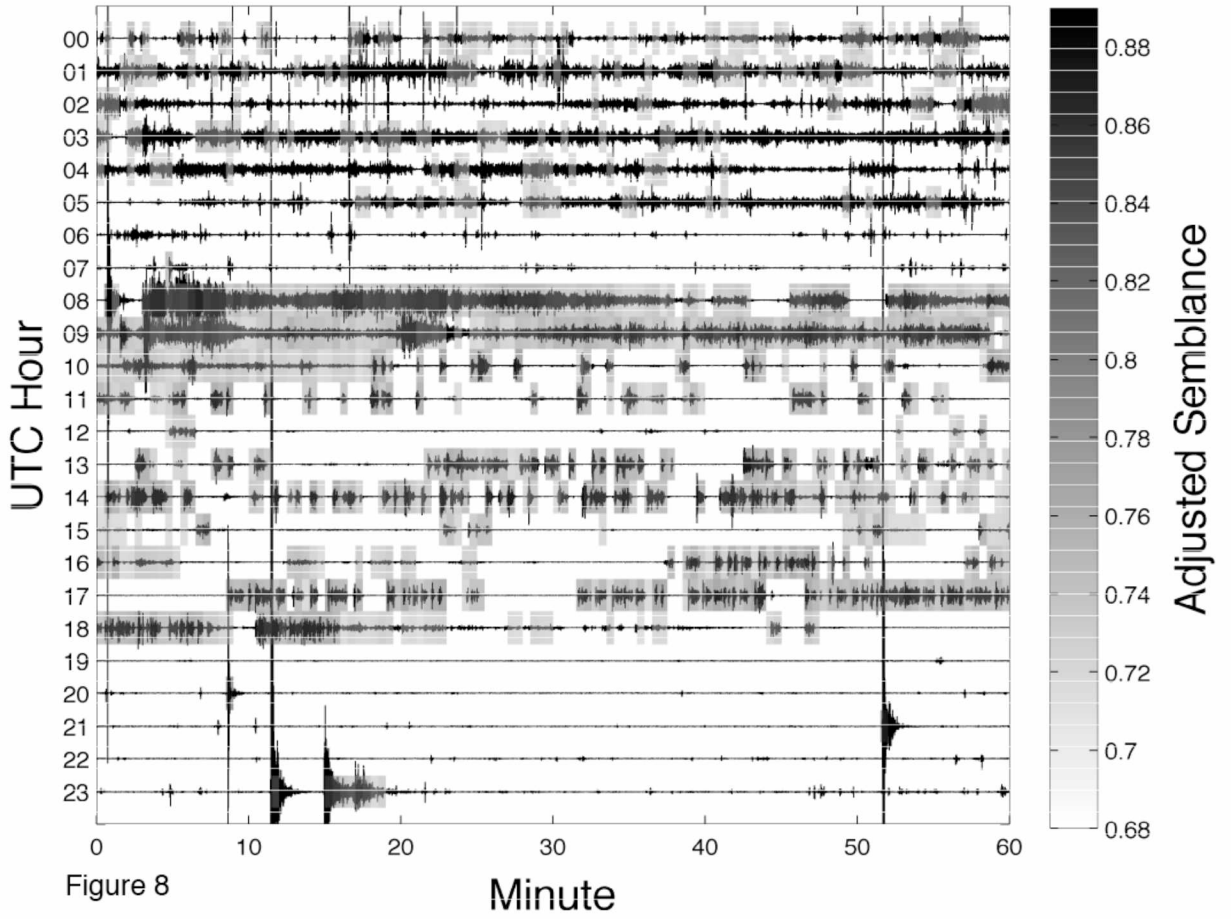

Figure 2.8 Psuedohelicorder Plot Overlain with Adjusted Semblance: Pseudohelicorder plot of data from station ARI on 23 July 2013. Data are filtered from 0.5 to 5 Hz and overlain with 30-s windows of semblance results. The scale is adjusted semblance, such that 0.5 corresponds to incoherent noise and 1 is perfect coherency. The lower bound of the scale bar is set below the threshold so that values at or above the threshold are shaded.

2.6 Conclusions

We performed network-based 3D location of infrasound sources at Sakurajima Volcano using the semblance technique. The source locations are generally offset to the northeast of the active vent (Showa crater) by ~130 m in the xy plane, with a straight-line offset of 360–420 m. Vertical resolution of the source location is poor, likely due to a generally 2D network all located below the vent. We incorporated 10-minute temperature data to estimate more realistic sound speeds, which improved the source locations but did not correct the offset. Wind speed and direction are also integrated into the semblance method and reveal that although wind can significantly influence the source location at Sakurajima Volcano, it also does not account for the general location offset. These results suggest realistic temperature and wind estimates should be

considered in future volcano acoustic source localization techniques. Analysis of the travel-time variance between each network station and the vent shows consistent time differences at each station and no diurnal variation. This evidence, along with analysis of the frequency content of the waveforms from each station and the station–vent profiles, suggests diffraction around topography plays a significant role in the semblance location offset at Sakurajima.

Ultimately, semblance is limited in regions of complex topography in which there is not a direct acoustic propagation path between source and receiver, and modified propagation paths need to be used. Other methods such as full waveform simulation and time-reversal source imaging (Kim and Lees, 2014) should be used in these scenarios. The semblance technique can still be useful for identifying times of coherent infrasound and effective at other locations with less significant topography and direct propagation paths.

2.7 Acknowledgments

We would like to thank the Sakurajima Volcano Research Center, Mie Ichihara, and Yuki Abe for assistance with data collection and planning, as well as Jeff Johnson, Philippa Demonte, Brian Terbush, and Robin Matoza. Funding was provided by National Science Foundation Grant EAR-1113294 and the Geophysical Institute. The manuscript was significantly improved by two helpful reviews.

2.8 References

Almendros, J., and B. Chouet (2003). Performance of the radial semblance method for the location of very long period volcanic signals, Bull. Seismol. Soc. Am. 93, 1890–1903, doi: 10.1785/0120020143.

Cannata, A., P. Montalto, M. Aliotta, C. Cassisi, A. Pulvirenti, E. Privitera, and D. Patanè (2011). Clustering and classification of infrasonic events at Mount Etna using pattern recognition techniques, Geophys. J. Int. 185, 253–264, doi: 10.1111/j.1365-246X.2011.04951.x.

Dawson, P., D. Whilldin, and B. Chouet (2004). Application of near real-time radial semblance to locate the shallow magmatic conduit at Kilauea Volcano, Hawaii, Geophys. Res. Lett. 31, doi: 10.1029/2004GL021163.

Fee, D., A. Yokoo, and J. B. Johnson (2014). Introduction to an open community infrasound dataset from the actively erupting Sakurajima Volcano, Japan, Seismol. Res. Lett. 85, no. 6, doi: 10.1785/0220140051.

Hadden,W. J., and A. D. Pierce (1981). Sound diffraction around screens and wedges for arbitrary point-source locations, J. Acoust. Soc. Am. 69, 1266–1276, doi: 10.1121/1.385809.

Iguchi, M., H. Yakiwara, T. Tameguri, M. Hendrasto, and J.-i. Hirabayashi (2008). Mechanism of explosive eruption revealed by geophysical observations at the Sakurajima, Suwanosejima and Semeru volcanoes, J. Volcanol. Geoth. Res. 178, 1–9, doi: 10.1016/j.jvolgeores.2007.10.010.

Johnson, J. B., J. F. Anderson, R. E. Anthony, and M. Sciotto (2013). Detecting geyser activity with infrasound, J. Volcanol. Geoth. Res. 256, 105–117, doi: 10.1016/j.jvolgeores.2013.02.016.

Johnson, J. B., R. C. Aster, M. C. Ruiz, S. D. Malone, P. J. McChesney, J. M. Lees, and P. R. Kyle (2003). Interpretation and utility of infrasonic records from erupting volcanoes, J. Volcan. Geoth. Res. 121, 15–63, doi: 10.1016/S0377-0273(02)00409-2.

Johnson, J. B., J. Lees, and N. Varley (2011). Characterizing complex eruptive activity at Santiaguito, Guatemala, using infrasound semblance in networked arrays, J. Volcanol. Geoth. Res. 199, 1–14, doi: 10.1016/j.jvolgeores.2010.08.005.

Jones, K. R., and J. B. Johnson (2011). Mapping complex vent eruptive activity at Santiaguito, Guatemala using network infrasound semblance, J. Volcanol. Geoth. Res. 199, 15–24, doi: 10.1016/j.jvolgeores.2010.08.006.

Jones, K. R., J. B. Johnson, R. Aster, P. R. Kyle, and W. C. McIntosh (2008). Infrasonic tracking of large bubble bursts and ash venting at Erebus Volcano, Antarctica, J. Volcanol. Geoth. Res. 177, 661–672, doi: 10.1016/j.jvolgeores.2008.02.001.

Kawakatsu, H., S. Kaneshima, H. Matsubayashi, T. Ohminato, Y. Sudo, T. Tsutsui, K. Uhira, H. Yamasato, H. Ito, and D. Legrand (2000). Aso94: Aso seismic observation with broadband instruments, J. Volcanol. Geoth. Res. 101, 129-154, doi: 10.1016/S0377-0273(00)00166-9.

Kim, K., and J. M. Lees (2011). Finite-difference time-domain modeling of transient infrasonic wavefields excited by volcanic explosions, Geophys. Res. Lett. 38, doi: 10.1029/2010gl046615.

Kim, K., and J. M. Lees (2014). Local volcano infrasound and source localization investigated by 3D simulation, Seismol. Res. Lett. 85, no. 6, doi: 10.1785/0220140029.

Lacanna, G., and M. Ripepe (2013). Influence of near-source volcano topography on the acoustic wavefield and implication for source modeling, J. Volcanol. Geoth. Res. 250, 9–18, doi: 10.1016/j.jvolgeores.2012.10.005.

Matoza, R. S., A. Le Pichon, J. Vergoz, P. Herry, J.-M. Lalande, H.-I. Lee, I.-Y. Che, and A. Rybin (2011). Infrasonic observations of the June 2009 Sarychev peak eruption, Kuril Islands: Implications for infrasonic monitoring of remote explosive volcanism, J. Volcanol. Geoth. Res. 200, 35–48, doi: 10.1016/j.jvolgeores.2010.11.022.

Modrak, R. T., S. J. Arrowsmith, and D. N. Anderson (2010). A Bayesian framework for infrasound location, Geophys. J. Int. 181, 399–405, doi: 10.1111/j.1365-246X.2010.04499.x.

Montalto, P., A. Cannata, E. Privitera, S. Gresta, G. Nunnari, and D. Patanè (2010). Towards an automatic monitoring system of infrasonic events at Mt. Etna: Strategies for source location and modeling, Pure Appl. Geophys. 167, 1215–1231, doi: 10.1007/s00024-010-0051-y.

Neidell, N. S., and M. T. Taner (1971). Semblance and other coherency measures for multichannel data, Geophysics 36, 482–497, doi: 10.1190/1.1440186.

Pierce, A. D. (1981). Acoustics: An Introduction to Its Physical Principles and Applications, McGraw-Hill, New York, New York.

Ripepe, M., and E. Marchetti (2002). Array tracking of infrasonic sources at Stromboli volcano, Geophys. Res. Lett. 29, 33-1–33-4, doi: 10.1029/2002gl015452.

Ripepe, M., D. Delle Donne, G. Lacanna, E. Marchetti, and G. Ulivieri (2009). The onset of the 2007 Stromboli effusive eruption recorded by an integrated geophysical network, J. Volcanol. Geoth. Res. 182, 131–136, doi: 10.1016/j.jvolgeores.2009.02.011.

Ripepe, M., E. Marchetti, and G. Ulivieri (2007). Infrasonic monitoring at Stromboli volcano during the 2003 effusive eruption: Insights on the explosive and degassing process of an open conduit system, J. Geophys. Res. 112, doi: 10.1029/2006JB004613.

Rowell, C., D. Fee, C. A. Szuberla, K. M. Arnoult, R. S. Matoza,P. P. Firstov, K. Kim, and E. Makhumdov (2014). Three-dimensional volcano-acoustic source localization at Karymsky Volcano, Kamchatka, Russia, J. Volcanol. Geoth. Res. 283, 101–115, doi: 10.1016/j.jvolgeores.2014.06.015.

Yokoo, A., M. Iguchi, T. Tameguri, and K. Yamamoto (2013). Processes prior to outbursts of Vulcanian eruption at Showa crater of Sakurajima Volcano, Bull. Volcanol. Soc. Jpn. 58, 163–181.

Yokoo, A., Y. J. Suzuki, and M. Iguchi (2014). Dual infrasound sources from a Vulcanian eruption of Sakurajim volcano inferred from cross-array observation, Seismol. Res. Lett. 85, no. 6, doi: 10.1785/0220140047.

Yokoo, A., T. Tameguri, and M. Iguchi (2009). Swelling of a lava plug associated with a Vulcanian eruption at Sakurajima Volcano, Japan, as revealed by infrasound record: Case study of the eruption on January 2, 2007, Bull. Volcanol. 71, 619–630, doi: 10.1007/s00445-008-0247-5.

Chapter 3

Analysis of Gas Jetting and Fumarole Acoustics at Aso Volcano, Japan[2]

3.1 Abstract

The gas-thrust region of a large volcanic eruption column is predominately a momentum-driven, fluid flow process that perturbs the atmosphere and produces sound akin to noise from jet and rocket engines, termed "jet noise". We aim to enhance understanding of large-scale volcanic jets by studying an accessible, less hazardous fumarolic jet. We characterize the acoustic signature of ~ 2.5-meter wide vigorously jetting fumarole at Aso Volcano, Japan using a 5-element infrasound array located on the nearby crater. The fumarole opened on 13 July 2015 on the southwest flank of the partially collapsed pyroclastic cone within Aso Volcano's Naka-dake crater and had persistent gas jetting, which produced significant audible jet noise. The array was ~ 220 m from the fumarole and 57.6° from the vertical jet axis, a recording angle not typically feasible in volcanic environments. Array processing is performed to distinguish fumarolic jet noise from wind. Highly correlated periods are characterized by sustained, low-amplitude signal with a 7–10 Hz spectral peak. Finite difference time domain method numerical modeling suggests the influence of topography near the vent and along the propagation path significantly affects the spectral content, complicating comparisons with laboratory jet noise. The fumarolic jet has a low estimated Mach number (0.3 to 0.4) and measured temperature of ~ 260 °C. The Strouhal number for infrasound from volcanic jet flows and geysers is not known; thus we assume a peak Strouhal number of 0.19 based on pure-air laboratory jet experiments. This assumption leads to an estimated exit velocity of the fumarole of ~ 79 to 132 m/s. Using published gas composition data from 2003 - to 2009, the fumarolic vent area estimated from thermal infrared images, and estimated jet velocity, we estimate total volatile flux at ~ 160 – 270 kg/s (14,000 –23,000 t/d).

[2] McKee, K., D. Fee, A. Yokoo, R. S. Matoza, and K. Kim (2017), Analysis of gas jetting and fumarole acoustics at Aso Volcano, Japan, *Journal of Volcanology and Geothermal Research*, 1–14, doi: 10.1016/j.jvolgeores.2017.03.029

3.2 Introduction

The sound produced by jet flow from human-made jet engines and rockets is called jet noise. Research on jet noise shows that its signal characteristics depend upon the jet's velocity, temperature, and nozzle diameter (Woulff and McGetchin, 1976; Tam, 1995; Tam, 1998). Human-made jets and their noise spectra exhibit self-similarity, with the spectral shape remaining relatively constant and scaling according to frequency, diameter, and velocity (Tam et al., 1996). Volcanoes generate jet flows at a variety of scales, from low-level gas jetting to violent subplinian-plinian volcanic jets. Recent investigations into infrasonic signals associated with volcanic jet flows have suggested that the self-similarity of jet noise may extend even to large (meters to hundreds of meters) volcanic length scales (Matoza et al., 2009; Fee et al., 2013; Matoza et al., 2013). Thus, similar relationships are hypothesized to exist between volcanic jet noise and volcanic jet flow parameters (e.g. vent diameter and jet velocity and temperature) (Matoza et al., 2009; Fee et al., 2013; Matoza et al., 2013). However, it is recognized that volcanic jet noise is more complicated than the case of human-made jet noise, since volcanic jet flows are multiphase and involve flow through complex vents that may also evolve with time during an eruption (Matoza et al., 2013). In this study we investigate these relationships empirically using field observations of a relatively small-scale volcanic jet flow: a fumarole.

In addition to being an analog to larger-scale volcanic jets, fumaroles are important to study in their own right. Fumaroles are a common outlet for volatiles at volcanoes, and changes in their activity may indicate changes in the volcanic system. From a monitoring perspective, detecting changes in fumarolic activity via infrasound, seismic, or a remote sensing method could provide critical information on the volcanic system in real-time. However, to use them in this capacity first requires a clear understanding of the geophysical signals they produce including detection and characterization. To date the work done towards characterization of fumarolic acoustics is an estimation of total acoustic power from gas jetting fumaroles by Woulff and McGetchin (1976).

A current goal of volcano infrasound research is to quantitatively relate recorded infrasound to the mass eruption rate of gas and tephra (Kim et al., 2015; De Angelis et al., 2016; Fee et al., 2017). Such quantitative relationships would greatly enhance hazard mitigation efforts through improved input parameters for plume modeling and near real-time estimates of erupted material.

Recent work has pointed out that previously proposed connections between acoustic power and volcanic gas exit velocity (Woulff and McGetchin, 1976) are likely not valid for volcanic jet noise, and can lead to significant errors in eruption parameter estimation (Matoza et al., 2013). Matoza et al. (2013) suggested that the relationship between volcanic jet noise and flow parameters such as jet velocity should be empirically derived through experiments and comprehensive field observation. Human-made jet noise is highly directional with respect to angle from the jet axis; thus, sampling over this angular range is necessary to accurately characterize the sound produced by the jet. Matoza et al. (2013) highlighted a challenge in realistic volcanic environments: limited angular sampling of the acoustic wavefield since infrasound sensors are usually deployed on the ground surface.

Fumaroles are more accessible and less hazardous than large-scale volcanic jets in the form of plinian eruption columns (Matoza et al., 2009; Fee et al., 2010a, Matoza et al., 2013); thus we investigate fumarole noise as a small-scale analog of large scale volcanic jet noise. Sound from fumaroles has previously been recorded and investigated using equivalent source theory (Woulff and McGetchin, 1976). In this study, we use campaign infrasound and thermal data to characterize the acoustic signal from a gas-jetting fumarole at Aso volcano, Japan (Fig. 3.1). We also evaluate the fumarolic jet noise scaling and jet parameters and use an assumed Strouhal number to estimate volatile mass flux. Aso Volcano was selected for this investigation because recent activity included gas-jetting fumaroles and provided a location where we could sample natural jet noise at a smaller angle relative to most studies, which are typically $> 90°$ from the jet axis. Our ultimate aim is to improve the relationship between acoustics and volcanic jetting.

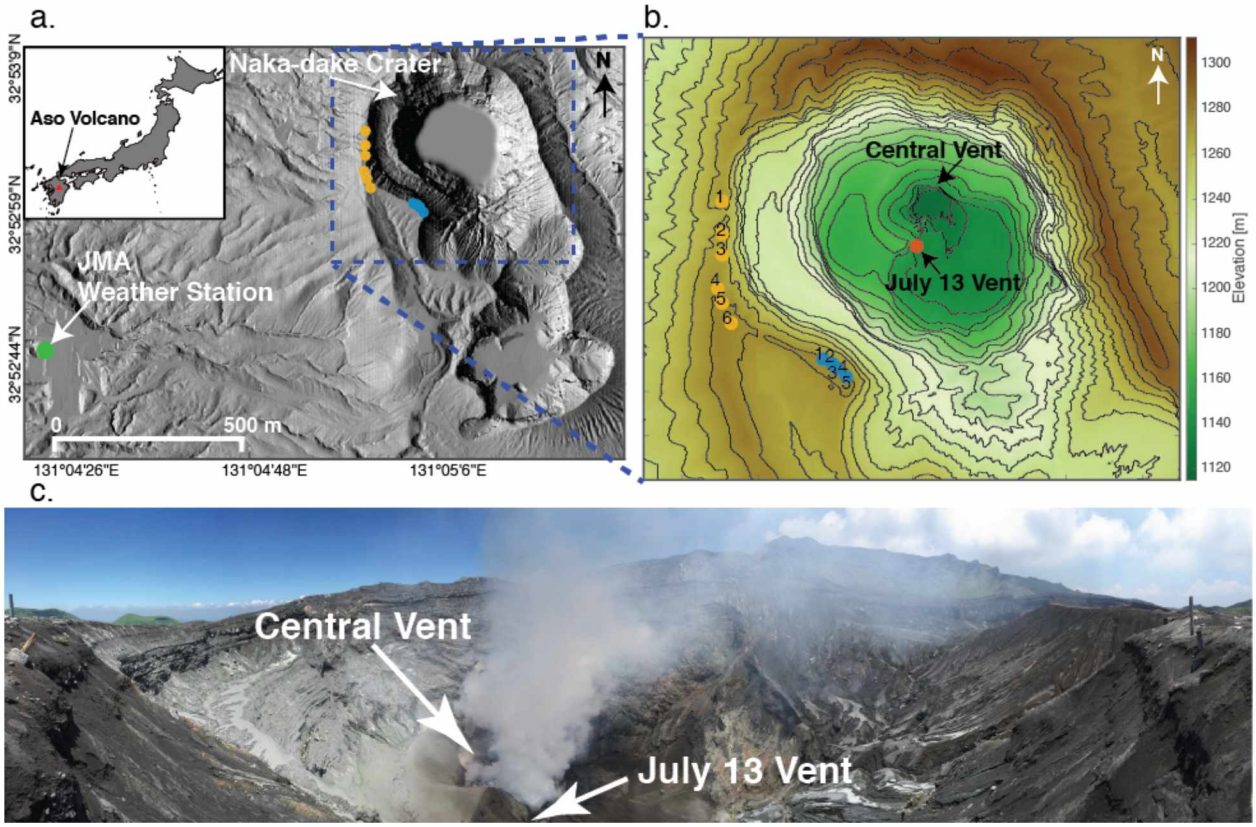

Figure 3.1 Maps and Photograph of Aso Volcano, Japan a) Location of Aso Volcano, Japan. Shaded relief map rendered from a 2012 1m-resolution digital elevation model of the active summit of Aso volcano. The green circle highlights the location of the JMA weather station. The gold circles are the locations of the first array deployment on the western crater edge and the blue circles are the second deployment locations. b) Combined contour and shaded relief map of Naka-dake crater created by combining three 1m-resolution DEMs. The central vent, July 13 vent (red circle), western array (gold circles) and southwestern array locations (blue circles) are shown. c) Panoramic photograph of Naka-dake crater taken ~10 m southeast of array element 5.

3.3 Background

3.3.1 Fumaroles

A fumarole is a vent in an active volcanic environment that issues steam and other volatiles (i.e. carbon dioxide, sulfur dioxide, etc.) at temperatures > 100 °C (Allaby and Allaby, 2003). They are found at volcanic summits and flanks, and their gasses are typically sampled to determine volatile species, ratios and flux as these hold information about the presence of magma at depth (Wallace, 2005; Fischer, 2008). Fumaroles are known to produce significant sound. Volcanologists often report audible jetting of volatiles from fumaroles. In seminal work, Woulff and McGetchin (1976) estimated the total acoustic power of fumarolic jets near the summit of Acatenango volcano, Guatemala using the power laws of Lighthill (1952). Lopez et al. (in prep.) report audible jetting of fumaroles at Mount Martin as far away at 16 km, which they suggest as

an indicator of high pressure degassing. Matoza et al. (2010) recorded sustained, audible sound from a vent in a lava tube at Kilauea Volcano on several occasions with a nearby infrasound array, and likened the sound to jet noise. While the lava tube vent is not a fumarole as it is described as jetting gas and spattering lava, it is a relevant comparison as it could be another example of a smaller scale volcanic jet. The sound from the lava tube vent was predominantly in the 5–10 Hz band, which was higher in frequency than the infrasonic tremor from the Pu'u 'O'o crater. It was suggested that the frequency content was higher due to the smaller diameter of the lava tube vent. While regular observations are made that fumaroles produce jet noise, little work as of yet has characterized fumarolic sound with respect to jet noise.

3.3.2 Jet Noise

A jet, whether human-made or natural, is the flow of momentum-driven fluid from a nozzle. Jet flow has three salient regions: core, transition and fully developed (Tam and Burton, 1984; Depuru Mohan et al., 2015). The core has nearly uniform fluid velocity with little turbulence. The transition region has a sharp drop in velocity from the jet axis outward and then self-similarity is reached in the fully developed region. The momentum-driven flow of a fluid into a quiescent fluid creates a velocity shear, which causes turbulence and mixing of the fluids (Kundu and Cohen, 2008). Turbulent jets can be conceptually decomposed into two components: fine-scale (FST) and large-scale (LST). The FST is randomly distributed eddies in the jet that are small relative to the jet diameter, while LST consists of coherent turbulent structure comparable in size to the jet diameter. Jet noise is the sound produced by the fluid flow downstream of the nozzle and is comprised of jet mixing noise, broadband shock associated noise, and screech tones (Tam, 1995), with FST and LST producing the two dominant components of jet mixing noise (Tam et al., 1996). Sound radiation from a jet is often characterized as a function of θ, relative to the jet axis and parallel to the overall jet flow (Fig. 3.2). LST noise is generally strongest in the downstream direction at small angles (~ 20°–40°) in a cone about the jet axis. FST noise is typically dominant at higher angles (~ 60°–96°), further upstream from the nozzle (Tam et al., 1996). In other words, jet noise is highly directional (Tam and Chen, 1994). Jet mixing noise spectra are broadband with power decay away from a broad peak frequency. FST and LST noise spectra both have a peak and fall-off in power at high and low frequencies away from the peak, but with different spectral shapes (Tam, 1995; Tam et al., 1996; Tam, 1998). The LST spectrum

is narrower while the FST spectrum is broader (Tam et al., 1996). A key characteristic of jet flows is their self-similarity, meaning jets have geometric, kinematic, and dynamic scaling and scale through time (Pritchard, 2011). Geometric scaling or similarity means if the nozzle diameter is increased then the length scale of the other jet components will increase by the same scaling factor while preserving all angles and flow directions. Kinematic scaling is when velocities at corresponding points have the same direction and their magnitudes have a constant scale factor. Dynamic scaling is met when the forces are parallel and are related by a constant scale factor. Since jet flows are self-similar, jet-noise is also proposed to be self-similar (Tam et al., 1996). This means that while experimental and human-made jets may range from centimeter to meter scale, the same features have been observed and in turn the recorded sounds have a similar spectral shape. For supersonic jets, the downstream movement of LST at supersonic speeds is considered the source of sound (Tam et al., 2008). However, for subsonic jets the growth and decay of LST at supersonic speeds perturbs the atmosphere to create acoustic pressure waves (Viswanathan, 2009). Jet noise is typically identified by its frequency content, features such as crackle for supersonic jets, and its distinct audible signature (Tam, 1995; Tam et al., 1996; Tam, 1998).

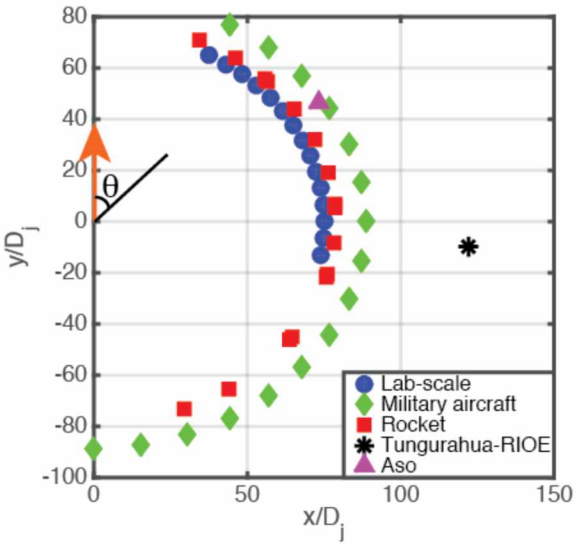

Figure 3.2 Comparison of acoustic observation angles and distances for lab-scale (blue circles), military aircraft (green diamonds), rocket engines (red squares), volcanic (Tungurahua-RIOE, black asterisk), and Aso fumarolic (purple triangle) jets. The x and y distances are scaled by the jet nozzle diameter, D_j. The nozzle is at (0, 0) and flows in the direction of the orange arrow. The black line highlights the angle θ relative to the jet axis. Figure modified from Matoza et al. (2013).

Volcanic jet noise from sustained sub-plinian and plinian eruptions has been observed to be high-amplitude, long-duration, emergent and broadband (Matoza et al., 2009; Fee et al., 2010a; Fee et al., 2010b). Jet noise from volcanoes spans infrasonic to audible frequencies, as audible jetting was noted at Karymsky volcano, Kamchatka (Lopez et al., 2013; Rowell et al., 2014). Volcanic jet noise is thought to be predominantly comprised of jet mixing noise. Broadband shock and screech tones are unlikely to be produced by volcanoes because of the natural, dynamic elements of a volcanic jet: irregular nozzle, tephra, and changing vent shape (Matoza et al., 2009). Taddeucci et al. (2014) recently observed high-frequency jet noise at Stromboli volcano, which may be related to shock waves emanating from the jet. Recent work has compared the PSD curves (Matoza et al., 2009) and skewness of the waveform probability density functions (Fee et al., 2013; Goto et al., 2014) of human-made jet noise with volcanic jet noise; this is possible because of the self-similarity of jets and jet noise. To compare different jet noise spectra the Strouhal number, St, is used. It is a dimensionless number of the form $St = \frac{fD_j}{U_j}$, where f is the peak jet frequency, D_j is the expanded jet diameter and U_j is the jet velocity. The Strouhal number is valuable for the analysis of unsteady, oscillating fluid flows, such as from jets. Comparison of human-made and volcanic jet spectra can be performed by evaluating the Strouhal numbers of the flows, assuming that both types of flows have a peak Strouhal number. Tam et al. (1996) observed that as jet velocity decreased towards ambient sound speed the Strouhal number asymptotically approaches a constant of ~ 0.19, independent of jet temperature. Some estimates of Strouhal numbers of volcanic jet flows have been made at Tungurahua, Ecuador: 0.4, and Mount St. Helens, USA: 0.06 (Matoza et al., 2009) and numerically modeled at 0.4 (Cerminara et al., 2016).

3.3.3 Aso Volcano

Aso Volcano, one of Japan's most active volcanoes and a popular tourist destination, is located in central Kyushu, the southern-most of the four main islands of Japan (Fig. 3.1a). It is an 18 × 25 km caldera with current activity focused at the northernmost crater of a north-south trending line of craters (Fig. 3.1a) (Kaneko et al., 2007). Fig. 3.1 shows a map view into the active crater at Naka-dake summit (Yokoo and Taniguchi, 2004; Takagi et al., 2006). From the southwestern rim, the crater is about 115 m deep with near vertical walls. Historic eruptions have consisted of basaltic to basaltic-andesite ash emissions with periods of strombolian and phreatomagmatic

activity (Kaneshima et al., 1996). After a 22 years hiatus, eruptive activity returned in November 2014 and lasted for 6 months. Fig. 3.3a shows an image of the crater taken in 2011 with two distinct degassing areas: the center and the south-southeast crater wall. This eruptive period included periods of strombolian to vulcanian, ash-poor to ash-rich explosions; gas jetting; and fumarolic degassing (Yokoo and Miyabuchi, 2015). Deposits from repeated strombolian explosions built a pyroclastic cone within the active crater (Fig. 3.3b, c). At its maximum in March 2015, the cone was ~ 20 m in height and had a ~ 200 m diameter at the base. On 3 May 2015 part of the cone collapsed into the central vent ending the strombolian activity. From this point, the central vent degassed without any ash and began to fill with water. On 13 July 2015 a new small vent opened at the edge of the partially collapsed pyroclastic cone, highlighted by the red circle and named July 13 vent in Fig. 3.1b. The July 13 vent is considered to be a large fumarole as it issued steam and other volatiles with no evidence of ash (Fig. 3.3c, d). The SSE wall fumaroles in Fig. 3.3a–c have been present for years, contribute to the total volatile flux, are not vigorous (Mori, 2012; Shinohara et al., 2015), and do not seem to produce audible or low frequency sound.

Aso Volcano was selected for this research project for several reasons. First, it is an accessible (i.e. road and cable car) volcano with both audible jet noise and continuous, vigorous degassing as observed by the scientists of the nearby Aso Volcanological Laboratory (AVL). This type of activity and access is unusual. Second, given the activity and access it is a relatively safe environment to work compared to more hazardous eruptions. Finally, the topographic setting at Aso allowed for unique sensor locations such that the microphones were deployed above the fumarole at a smaller angle to the jet axis than previously achieved in volcano studies (Matoza et al., 2009; Rowell et al., 2014).

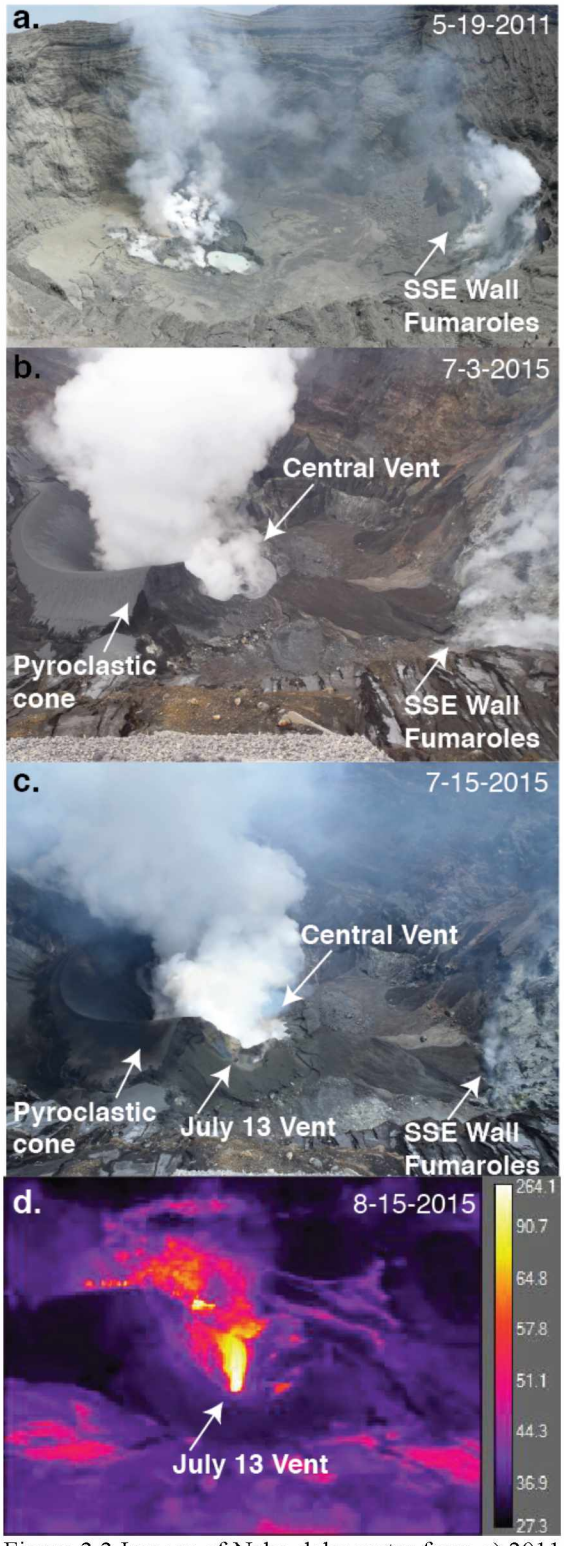

Figure 3.3 Images of Naka-dake crater from a) 2011 and b), c) and d) 2015. a–c) show the activity at the center of the crater and the fumaroles on the southeastern crater wall. c) Visible and d) thermal infrared images of the July 13 vent with steam plume rising from the central vent in the background. The warm spots in the foreground are due to correcting the entire TIR image by the distance from the camera to the July 13 vent. Images were taken from the southwestern array location.

3.4 Data

In July 2015 we deployed a 6-element array of infrasound sensors along the western rim of the active crater of Aso (Fig. 3.1a, b). The microphones, referred to as Volcano Differential Pressure (VDP) sensors, (Thelen and Cooper, 2015) have a sensitivity of 10 mV/Pa. The sensors have a flat response between 0.0125 and 25 Hz and data were recorded on a 6-channel Geotech SMART-24 digitizer at 250 Hz, permitting sampling of both the infrasonic and lower audible frequency range. Sensor responses were verified in huddle tests before and after the experiment. The array was initially deployed along the western crater rim to get as much azimuthal coverage as possible relative to the permanent infrasound network run by AVL.

During the deployment the aforementioned July 13 vent opened at approximately 17:00 UTC 13 July 2015, and is shown in visible and infrared images in Fig. 3.3c, d. The local, permanent seismoacoustic network did not detect the opening of the fumarolic vent, nor did the temporary acoustic array on the western crater rim. AVL observed its presence with the local web camera. When in the field, standing where the July 13 vent was visible, this vent clearly produced audible sound akin to jet noise. However, this audible noise was not heard on the west rim of the caldera where the array was located, nor was coherent sound detected in initial processing of these data. Therefore, we moved the array to the southwestern rim to better capture the sound produced by the July 13 vent. The array was at the western rim from 3 July to 3 August 2015 and at the southwestern rim from 3 to 13 August 2015. Fig. 3.1b shows the locations of the first and second array locations, central vent, and July 13 vent. While at the second location, the array was 216.9 m from the July 13 vent and positioned 57.6° from the vertical jet axis, a recording angle usually not feasible in volcanic environments. The inter-element spacing was about 10 m, with five sensors aligned along the crater rim. The July 13 vent was visible from elements 2–5 but not from element 1, as the crater rim topography blocked line-of-sight.

In addition to the infrasound data, four thermal infrared (TIR) images were captured just after the deployment period by AVL. A FLIR T440 camera was used to take images at the locations of array elements 1, 2, 3 and 5 on 14 August 2015 (Fig. 3.3d). Note the fumarolic vent was not visible from array element 1, but the heat from the jet was observed in thermal IR. AVL shared

five digital elevation models (DEM): two of the Aso summit region at 1 m (Fig. 3.1a) and 5 m resolution and three of Naka-dake crater at 1 m resolution (Fig. 3.1b). The crater DEMs were collected in March 2015, May 2015 after the cone collapse using an unmanned aerial vehicle, and August 2015 using reconstructed photographs taken on a circumnavigation of the crater rim.

3.5 Methods

To characterize the acoustic signal of Aso's gas jetting fumarole, array-processing methods are applied to determine times of coherent signal. We use the Mean of Cross-Correlation Maxima (MCCM) method as it has been shown to be a robust detector even when the signal-to-noise ratio is low (Lee et al., 2013). To determine times of coherent acoustic signal with MCCM, data are band-pass filtered in frequency bands of interest and then unique sensor pairs are cross-correlated through time with appropriate window lengths relative to signal period. The mean of the peak cross-correlation values for each time window is then taken as the MCCM. For the data recorded at Aso, we use three different frequency bands and a complementary, non-overlapping window length: 0.5 to 5 Hz with a 10 s window, 5 to 15 Hz with a 5 s window, and 15 to 25 Hz with a 2 s window. A 0.5 Hz lower bound was chosen to remove the microbarom influence. The 25 Hz upper limit was selected because topography and other propagation effects increasingly influence shorter wavelengths. An MCCM value of 0.8 or higher was considered indicative of coherent acoustic signal. During the first 4 weeks of the deployment, when the array was on the western rim, no correlated signals were found. The crater rim had high winds during the site visits and the sensors did not have any wind noise suppression installed. To then describe the acoustic characteristics of the fumarole time series, spectrograms and power spectral density (PSD) curves were analyzed for 30 + minute windows where MCCM values were > 0.8. The PSD curves were smoothed once for ease of comparison using a triangular window.

The effects of path to acoustic wave propagation include power loss from increased path length and altering the waveform due to reflections. Recent work has shown that topographic path effects significantly contribute to the recorded acoustic waveforms in volcanic environments (Lacanna and Ripepe, 2013; Fee et al., 2014; Kim and Lees, 2014), and that to account for it, 3-D numerical modeling should be incorporated (Kim et al., 2015). Acoustic waves diffract or bend around obstacles in their path such as topographic structures. This increases the path length and

decreases the recorded amplitude compared to a wave with the same source-receiver distance without an obstacle. Recent work has also shown that as acoustic waves diffract around the crater rim of a volcanic edifice the waveform shape is altered, particularly the initial rarefaction (Kim and Lees, 2011; Lacanna and Ripepe, 2013). For the frequency bands used in our analysis, the corresponding wavelengths range from 13.6 m (25 Hz) to 680 m (0.5 Hz) at a sound speed of 340 m/s. As the crater wall is about 115 m high on the southwestern side and within the range of our wavelengths of interest, it will likely influence the recorded waveforms. Reflections from Aso's crater may also be significant and should be considered. To account for topographic path effects we computed numerical waveforms in three dimensions using the finite difference time domain (FDTD) method of Kim et al. (2015), which incorporates a high-resolution DEM. We assumed a homogeneous atmosphere (density = 1.16 kg/m^3, sound speed = 346 m/s) for numerical simulations as the variation of the speed of sound and air density should be small and their influence on sound propagation minimized at the distances considered here (Johnson and Ripepe, 2011; Kim and Lees, 2014; Kim et al., 2015).

We merged three high resolution DEMs of Naka-dake crater for the synthetic data calculation and to determine a more accurate location of the July 13 vent. This merge was necessary because the May 2015 DEM did not cover a large enough area nor did it contain the July 13 vent and the August 2015 DEM had skewed elevations at the walls due to the acquisition method. The resulting DEM is shown in Fig. 3.1b.

The determination of the jet parameters, specifically the jet diameter, temperature and gas exit velocity, are necessary to facilitate jet noise comparison. We determine the jet diameter and temperature by analyzing infrared thermal images. The raw thermal images were corrected for distance (216.9 m), air temperature (21.1 °C) and local relative humidity (87%) by inputting those parameters into the ResearchIR software. Local air temperature and relative humidity data are from the JMA weather station (Fig. 3.1a). There is uncertainty in using these values as the weather station is not at the Naka-dake crater rim, but we do not expect the differences to significantly affect the results. The default emissivity value (0.95) in ResearchIR was used, as an emissivity value could not be found for water vapor or any other gas. However this value is likely too high as theory suggests pure hot gas emissivity is < 0.2 and invisible in TIR (Yokoo et

al., 2013). The jet diameter is determined by first computing the pixel dimensions in physical space at the July 13 vent. The thermal images are 320 × 240 pixels with a field of view of 25° × 19°. The dimension of a pixel is $x = \left(2d \tan\frac{\alpha}{2}\right)/n_x$ and $y = \left(2d \tan\frac{\beta}{2}\right)/n_y$, where d is the distance from the location the image was taken to the location of a pixel in physical space, α and β are the field of view for a given camera, the FLIR T440 in this case, in the x and y dimensions, and n_x and n_y are the number of pixels in horizontal and vertical dimensions of the image, respectively (Lillesand et al., 2008). The hottest pixel in each image is assumed to be the center of the fumarolic vent. The dimension of the hottest pixel in each image is approximately 0.3 × 0.3 m, giving an estimate of the hottest pixel resolution at the fumarolic vent. As the vent in the images used is ~ 8 pixels across, we assume the dimensions of the hottest pixel is an appropriate approximation for all the pixels near it. We then take a temperature profile from left to right across the images through the hottest pixel. The average width of the temperature peak in the profiles from array elements, 2, 3 and 5 was taken as the jet diameter. The TIR image taken from array element 1 was not used, as the vent was not visible from that position. The average temperature of the hottest pixel from the same three images was used as the jet temperature. To compare different jets we estimated the jet temperature ratio, T_j/T_a, where T_j is jet temperature and T_a is ambient temperature.

Once the jet temperature and peak spectral frequency are determined, the Strouhal number is used to estimate the jet velocity. Assuming the fumarolic jet noise is comprised of mostly jet mixing noise and behaves similar to human-made jets (Matoza et al., 2009), we use a Strouhal number of 0.19 and calculate velocity by $v = \frac{f \times D_j}{St}$, where f is the peak frequency selected from the PSD curves and D_j is the jet diameter determined from the temperature profiles. Like the temperature ratio, another key ratio for comparing jets is the velocity ratio, v_j/v_a, where v_j is the jet velocity and v_a is the speed of sound. This ratio is known as the Mach number, M. A jet with $M < 1$ is labeled subsonic and $M > 1$ is supersonic. Once the jet velocity is estimated, the volatile flux, j_v, is estimated by $j_v = \rho v_j A$, where ρ is the density of the volatiles, v_j is estimated jet velocity, and A is fumarolic vent cross-sectional area. To estimate volatile density in the jet, we used gas composition data in Table 1 of Shinohara et al. (2015), collected at Aso from fumaroles over a five year period, 2004 –2009. They published gas concentrations in μmol/mol for the

following species: H_2O, CO_2, SO_2, H_2S, HCl, HF, and H_2. The gas concentration from 16 samples were averaged and then converted to density using the ideal gas law. For example, the volume can be calculated by converting 980,000 ppm H_2O to 980,000 × 10^{-6} m^3 H_2O per 1 m^3 air. We then calculate the number of moles, n, using $n = PV/RT$, where P is the atmospheric pressure at Naka-dake crater's elevation, 1159.9 m above sea level (88,563 Pa), V is the volume (0.98), R is the ideal gas constant (8.31441 Pa/K•mol), and T is the gas temperature estimated from the thermal images. The number of moles, n, is then multiplied by the molecular weight of water, 18.02 g/mol, which gives the H_2O density, ρ_{H_2O}. This is repeated for each volatile species and then the densities are summed to get the total volatile density, ρ_T. The total volatile density (kg/m^3) is then multiplied by estimated jet velocity (m/s) and vent area (m^2) to estimate total volatile mass flux (kg/s).

3.6 Results

3.6.1 Signal Detection

MCCM analysis of the dataset revealed periods of acoustic signal from Aso's July 13 vent, as well as extensive periods of high noise (wind). Hours to days of correlated signal are detected during the 10 days the array was deployed in the second location, although strong winds still influenced the detections. Fig. 3.4a shows six hours of array acoustic data and Fig. 3.4b the peak cross-correlation values through time for each of the unique sensor pairs. The peak pressure for each trace is listed to the left and highlights the low amplitude of the signal, typically < 1 Pa. Infrasonic amplitude decays at a rate of $1/r$, where r is the distance from the source. To compare pressure amplitudes, the pressures are reduced to a reference distance, r_{ref}, usually 1 or 1000 m from the source, by simply multiplying the pressure by r/r_{ref} distance (Johnson and Ripepe, 2011). Infrasonic tremor from the Halema'uma'u Crater of Kilauea Volcano has pressures of ~ 477 Pa when reduced to 10 m (Fee and Matoza, 2013), which is orders of magnitude larger than the jet noise recorded at Aso (~ 6 Pa when reduced to the same distance). Fig. 3.4c–d, similar to Fig. 3.4a–b, highlights times with larger amplitudes where the traces appear visually similar, but the correlation values are low. This suggests the presence of wind noise as the array elements were spaced far enough apart to reduce wind noise correlation (Walker and Hedlin, 2009). Fig. 3.5a, c, and e shows the MCCM values for the second array location for three different frequency bands over a span of 9 days and Fig. 3.5b, d, and f shows the times series data from array

element 3 for the respective frequency bands. The red dots indicate MCCM > 0.8. Hours to days of correlated signal in the 0.5 to 25 Hz band are present. Fig. 3.5g shows the wind speeds recorded at a Japan Meteorological Agency (JMA) weather station ~ 1 km from Naka-dake crater (Fig. 3.1a). This figure shows that when the wind speed increases, the MCCM values in the three frequency bands drop significantly.

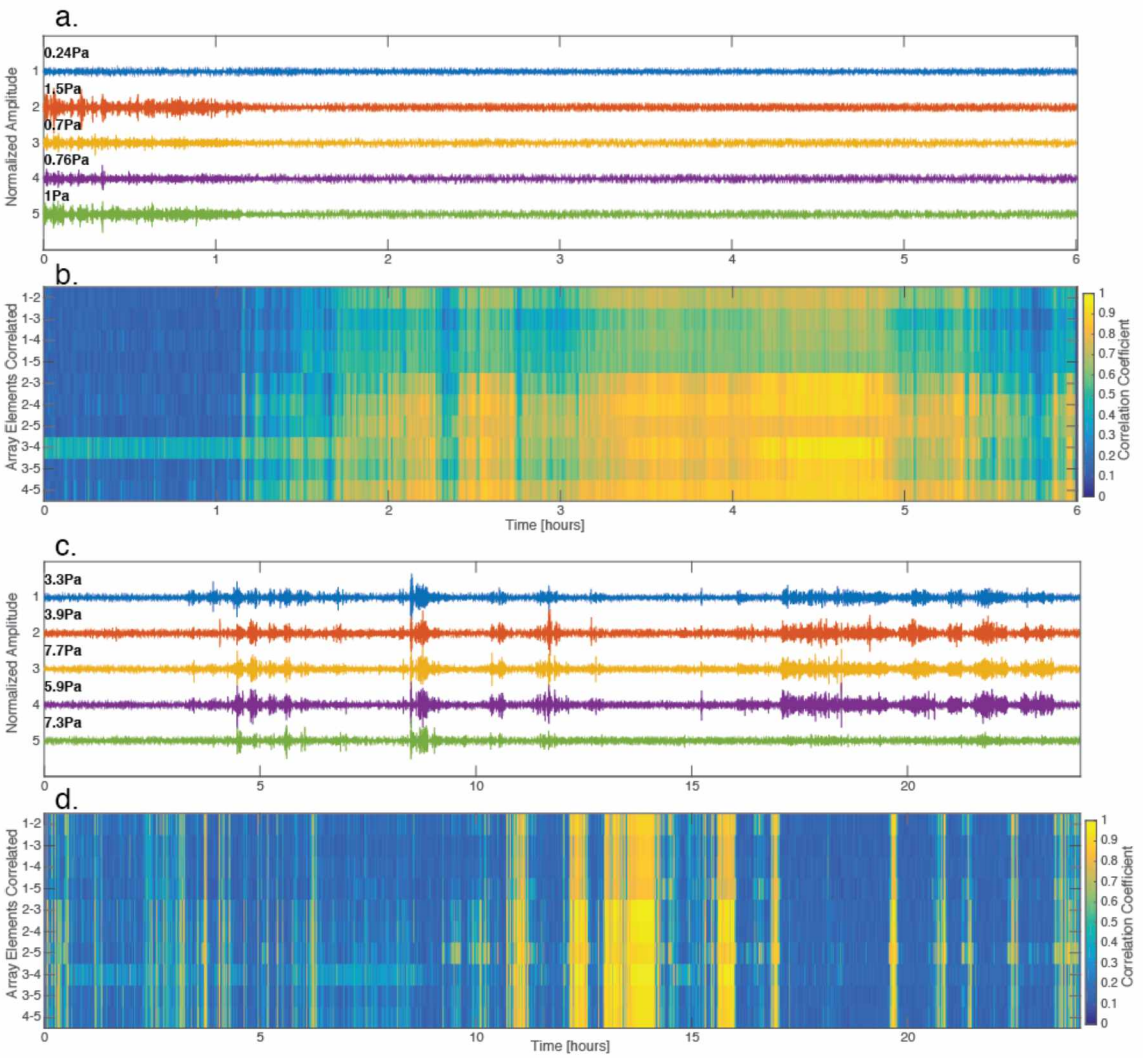

Figure 3.4 Normalized Time Series Data and Peak Cross-correlation Values a) 6 h of normalized acoustic data from array elements 1–5 starting on 4 August 2015 at 17:30 UTC. Data were filtered from 0.5 to 5 Hz. Peak amplitude for each trace is listed at the left. b) Each row represents the peak cross-correlation values though time for each sensor pair in the array. Filtered data from unique element pairs were cross-correlated using a 10-second non-overlapping moving window. c) and d) show time series data and peak cross-correlation values through time as in a) and b), but for 24 h of data starting on 08 August 2015 at 00:00 UTC.

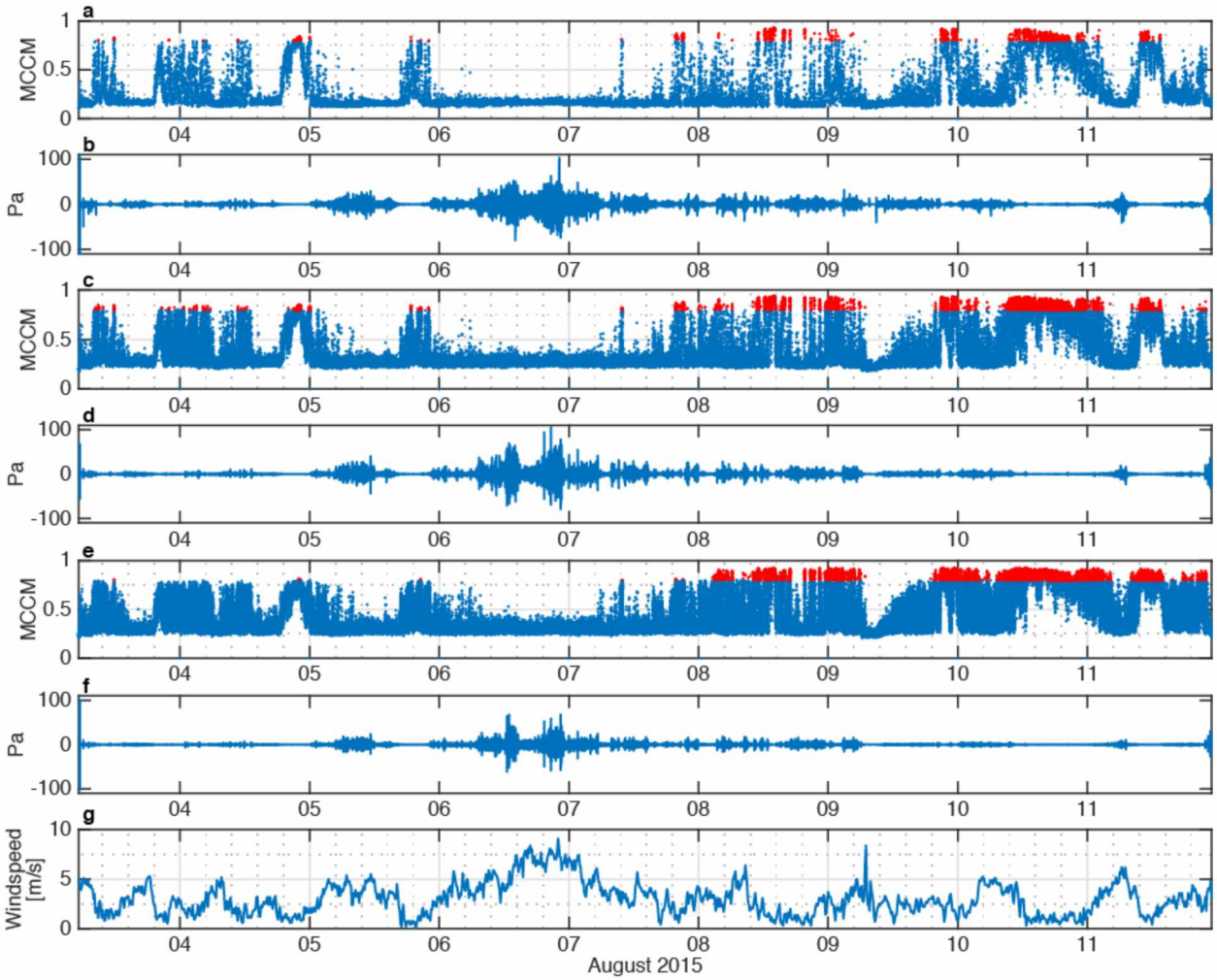

Figure 3.5 Mean cross-correlation maxima (MCCM) and waveforms from array element 3 from 3 to 11 August 2015 for three different frequency bands: a) MCCM filtered from0.5 to 5Hz with a 10-second window and b) waveforms; c) 5 to 15 Hz with a 5-second window and d) waveforms; and e) 15 to 25 Hz with a 2-second window and f) waveforms. Red dots indicate MCCM > 0.8. g) 10-minute averaged wind speed data recorded at a Japan Meteorological Agency weather station ~1 km southwest of Naka-dake crater (Fig. 3.1a).

3.6.2 Spectral Analysis

We analyze the spectra to help identify jet noise from the July 13th fumarole. Fig. 3.6a, b and c shows the time series and spectrogram data from element 3, and PSD curves from elements 1 to 5, respectively, for 30 min of data on 4 August 2015 with MCCM values above the threshold. Fig. 3.6d, e and f are similar, but for a 30-minute window recorded on 8 August 2015. The pressures for both of these have been reduced to 10 m from the source as described previously. These two time series examples show persistent tremor that does not change over the duration shown. The spectrograms show this tremor to be predominantly below 20 Hz, but also present up to 60 Hz. The PSD curves further illustrate the broadband nature of the signal as the power

decays linearly to about 1 Hz, then increases at 2 Hz and decays over a broad curve into the higher frequencies. The signal is low-amplitude, especially compared to the wind noise (Fig. 3.4c), as the amplitude is on the order of 0.1 Pa at ~ 220 m from the source. It is sustained for hours to days with peak frequencies ranging from 2 to 10 Hz. Fig. 3.6c shows a time when the peak frequency is 2–6 Hz and in Fig. 3.6f it is about 6–10 Hz; the latter is more commonly observed in our dataset. We note there is significant structure and differences in power in the PSD curves, particularly at frequencies > 10 Hz.

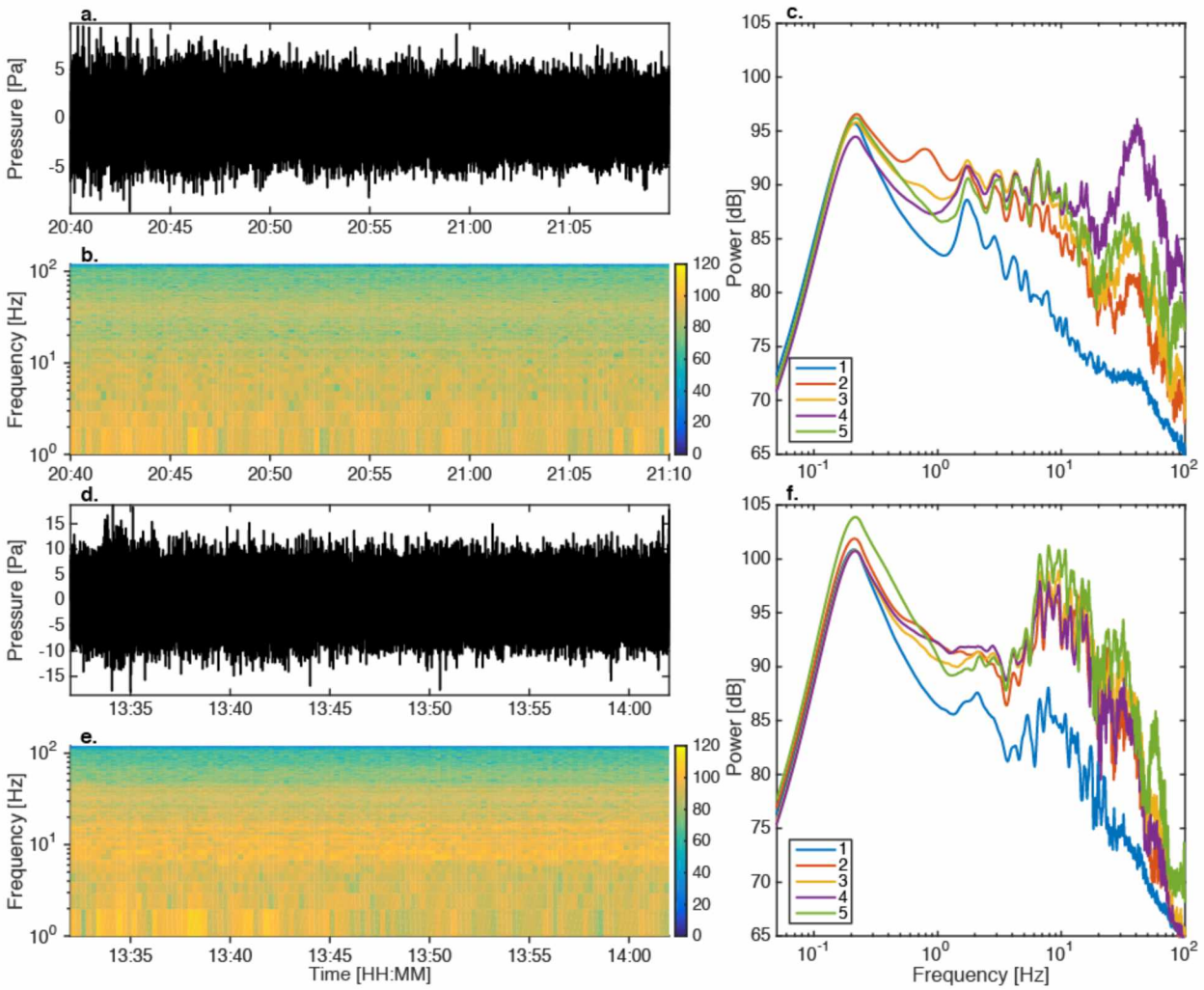

Figure 3.6 Fumarolic Jet Noise Time Series Data, Spectrograms, and Power Spectra a) 30min of times series data and b) the corresponding spectrogram from array element 3 on 4 August 2015 starting at 20:40 UTC. The pressure has been reduced to 10 m from the fumarolic vent. c) Smoothed power spectra for the same 30-minute window of data for array elements 1–5. d), e), and f), show the same information as a), b), and c), respectively for 30 min of sound recorded on 8 August 2015 starting at 13:32 UTC.

3.6.3 Path Effects

Fig. 3.7 shows the topographic profiles from each array element to the fumarolic vent to investigate acoustic propagation and local path effects. We note two items in the topographic profile that may be relevant to the acoustic propagation: 1) the crater wall is a significant feature, ~ 115 m high, on the same order of the acoustic wavelengths of interest and 2) the crater wall does not change significantly between the profiles aside from a small perturbation in profiles 1 and 2 just around 100 m between the sites and vent.

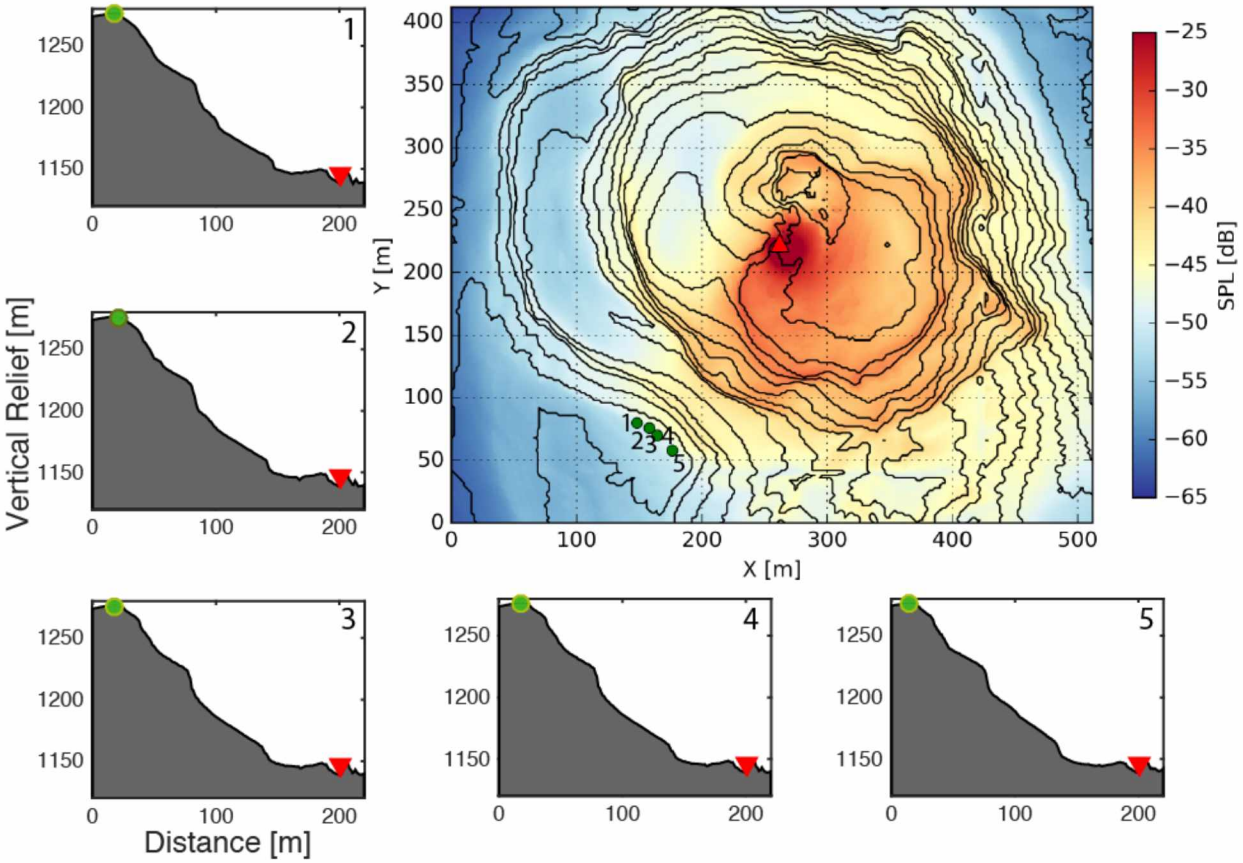

Figure 3.7 Topographic Profiles and Sound Pressure Level (SPL). Topographic profiles 1–5 are from array elements 1–5 (green circles), respectively, to the fumarolic vent (red triangles). The five profiles correspond to the five array elements (green circles) in the central contour map. The contour map of Naka-dake crater is overlain with the total SPL loss for the 4-second SW computation. The red triangle is the location of the fumarolic vent and the point where the source time function is inserted. Array elements 3 and 4 were deployed next two each other and thus appear as a single circle. As the colors approach blue they represent lower sound levels (hence greater sound loss).

Synthetic waveforms, SWs, were computed by the FDTD method to further investigate spectral properties of the observations and influences of acoustic propagation (i.e. topographic propagation effects). We use a simple, impulsive, broadband source (blackman-harris window

function) to excite acoustic wavefields in the modeling (Kim et al., 2015). Fig. 3.8 shows the synthetic source and subsequent SWs. Note that the purpose of this numerical simulation is to generate "pseudo" Green's functions to understand sound propagation effects on sound amplitudes and spectral properties, but is not to reproduce the observed signals. Actual acoustic sources for fumarolic activities should be more complicated than a simple impulse used here. From array element 5, the southeastern most, to 1, the northwestern most, there is increasing loss in amplitude. This loss is reflected in the spectra as well. Fig. 3.9a shows the power spectra for the SWs using Thomson's multitaper method due to the small number of data points. Details of this method are found in Thomson (1982) and Prieto et al. (2007). The source spectra have been deconvolved from the SWs spectra. Fig. 3.9b shows the power difference relative to the first array element. For this plot, the spectrum from SW for element 1 was subtracted from the spectra for SWs for array elements 1–5. There is little difference in the SWs spectral power below about 3 Hz above which the differences are about 1 to 3 dB. The power difference between any given array element and element 1 are not consistent across frequencies. For example, at about 4 Hz the difference between elements 1 and 5 is over 3 dB, while at about 5 Hz it is < 1 dB. The structure in the SWs spectra is similar across the array elements up to about 6 Hz at which point they vary. Fig. 3.7 shows the total sound pressure level (SPL) for an impulsive source initiated at the fumarolic vent, indicated by the red triangle, and propagated out for 4 s. Significant near-source directionality is present in this figure, as the SPL is highest to the south and southeast of the source, with significant loss to the northwest.

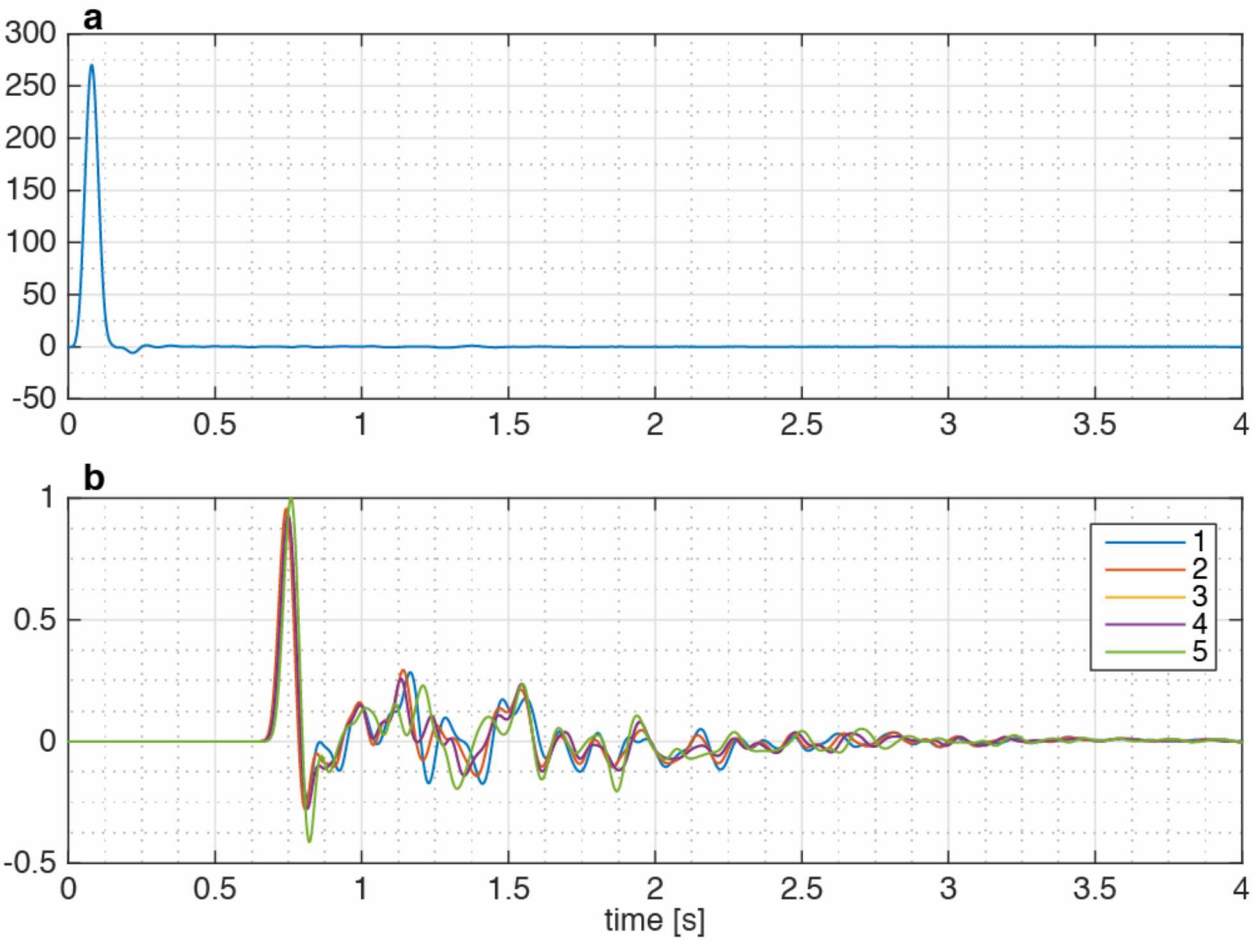

Figure 3.8 Source Function and Synthetic Waveforms a) The source function for computing the synthetic waveforms. b) are the synthetic waveforms for array elements 1–5. The source time and SWs have been normalized by the maximum value in the SWs.

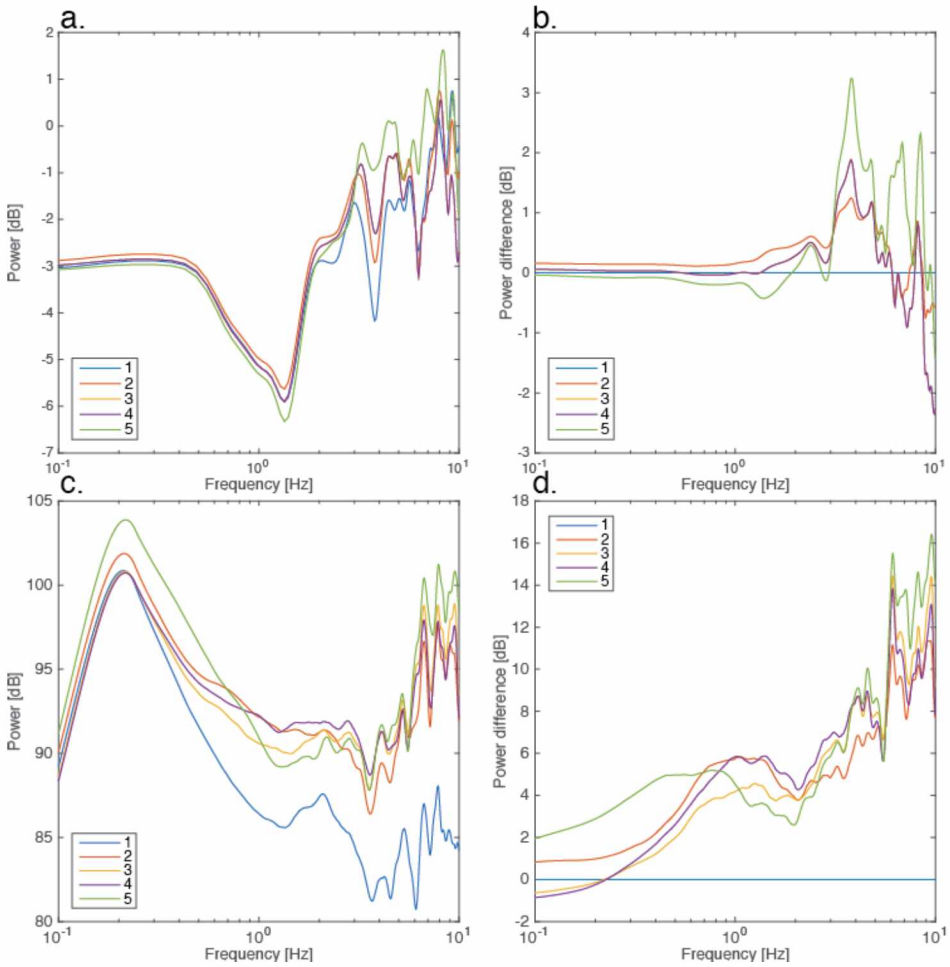

Figure 3.9 Synthetic and Observed Power Spectral Comparison a) Power spectral density curves for the SWs using the multitaper method. b) Power difference relative to array element 1 SW. c and d) are the smoothed power spectra and power differences relative to array element 1 for the same 30 min of data from Fig. 3.6d, e and f.

3.6.4 Volcanic Jet Parameters and Volatile Mass Flux

Volcanic jet diameter and velocity are derived using infrared and acoustic data, respectively. Fig. 10 shows a corrected infrared thermal image from a FLIR camera at ~ 220 m distance and the corresponding temperature profile. The inferred jet diameter and temperature are ~ 2.5 m and ~ 260 °C, respectively. We estimated the fumarolic jet velocity to be 79 to 132 m/s based on the more commonly observed range of peak frequencies, 6–10 Hz (Fig. 3.6) and the assumed St = 0.19. The average air temperature during the second array deployment was 21.8 °C from the local JMA weather station. This results in a temperature ratio of 11.9; a temperature ratio above 1 indicates the jet is hot. The speed of sound given the local average air temperature is 344.5 m/s. This gives a range of Mach numbers from 0.3 to 0.4, where a Mach number < 1 indicates the jet is subsonic.

Volatile flux (Table 1) is estimated using the estimated jet temperature, diameter and velocity, and volatile concentrations from Shinohara et al. (2015). For the flux estimations in Table 1, the jet velocity ranges from 79 to 132 m/s and the vent area is 4.91 m^2, assuming the vent is circular. Water is the most abundant volatile of the total at 11,000 to 18,000 t/day and the SO_2 mass flux is 850 to 1400 t/day.

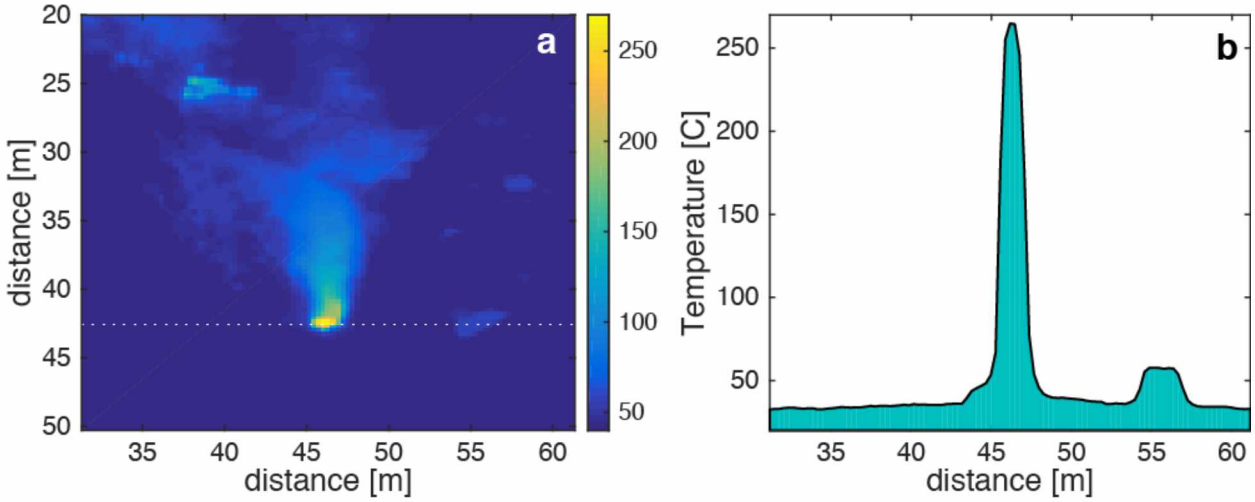

Figure 3.10 Thermal infrared (TIR) observations. a) TIR image captured on 14 August 2015 of the fumarolic vent from array element location 3. The dotted white line is where the temperature profile was taken. b) The temperature profile taken from left to right across the hottest pixel from the TIR image a.

Table 3.1 Volatile species and their estimated fluxes

Volatile Species	Mean Concentration	Molecular Mass	Density	Estimated Flux	Estimated Flux
	[µmol/mol]	[g/mol]	[g/m^3]	[Kg/s]	[tonnes/day]
H_2O	920000 ±32000	18.02	331	130 - 210	11000 - 19000
CO_2	59000 ±22000	44.01	52	20 - 34	1700 - 2900
SO_2	20000 ±7700	64.06	26	9.9 - 17	860 - 1400
H_2S	1200 ±580	34.08	0.82	0.32 - 0.53	27 - 46
HCl	2270 ±1000	36.46	1.7	0.64 - 1.1	55 - 93
HF	510 ±340	20.01	0.20	0.079 - 0.13	6.8 - 11
H_2	2900 ±2900	2.02	0.12	0.045 - 0.076	3.9 - 6.6
			Total:	160 - 270	14000 - 23000

3.7 Discussion

We observed a small vent in the base of a volcanic crater vigorously jetting gas with audible sound akin to jet noise. The temperature contrast between the gasses and ambient atmosphere made the jet easily distinguishable in the thermal IR band, which enabled an estimate of the diameter. The high temperature ratio of the jet is of note as it indicates LST noise will be the dominant noise source over a wider range of observation angles (Tam et al., 1996). Fig. 3.5 shows correlated signal from 0.5 to 25 Hz and Fig. 3.6c, and f shows consistent spectral structure (i.e. the shape of the PSD curve including peaks and troughs) across array elements in the same frequency band and higher. This is evidence that the acoustic signal from the fumarolic jet is broadband and present in the infrasonic (< 20 Hz) to audible range (> 20 Hz). The character of the acoustic data is sustained, low-amplitude and broadband. Given these observations, we infer the sounds observed with microphones and by those in the field at Aso to be jet noise. Assuming it is jet noise, a reasonable jet velocity was estimated (79–132 m/s) based on the assumed St = 0.19.

3.7.1 Wind Noise

Wind can hinder infrasonic detection of low amplitude sources. The lack of correlation between array elements during the initial west crater deployment was likely the result of wind noise overpowering the volcanic signal, as the deployment overlapped with the rainy season in Japan. Fig. 3.5g shows the 10-minute running average wind speed near the summit of Aso from 3 to 11 August 2015. Each time the wind speed increases the MCCM values drop, indicating that the wind masks the jet noise. To reduce wind noise instruments are often deployed in vegetation as this increases surface roughness and reduces wind (Walker and Hedlin, 2009). Other methods for wind noise reduction include arrays of hoses or pipes attached to a sensor or dense arrays of instruments. None of these options were feasible at Aso as there is no vegetation near the summit, as is often the case with active volcanic environments, and space and installation time were limiting factors. Array processing can help reduce wind noise and identify correlated signal. While the wind noise did not correlate between the array elements, there were still times in which it over powered the signal of interest. Wind not only buries signal in noise, but it can also delay or advance the arrival of sound waves particularly when sensors are deployed as a network. These differences in infrasonic arrival time have been used to invert for the wind speed

and direction (Marcillo and Johnson, 2010) and shown to affect source location (McKee et al., 2014). We did not observe altered arrival times at Aso given the microphones were deployed in an array in which sound delay should be minimal. Ultimately, wind noise challenges observance of low amplitude signals and should be accounted for in experiment design.

3.7.2 Jet Noise Spectra

Assuming this fumarolic gas jet behaves similarly to a laboratory jet, certain characteristics are expected in the acoustic spectra. The fumarolic jet has a Mach number of about 0.3 to 0.4 and a high temperature ratio, which suggests the sound is jet-mixing noise and given the small θ, LST is likely the dominant source. Sound from a heated, low Mach jet is not well studied; however, there is a general understanding of the sound mechanisms (Viswanathan, 2004). In supersonic, high Mach number jets, the mechanism for LST sound production is the LST moving and propagating downstream at supersonic speeds. For subsonic jets, the sound is produced by the growth and decay of LST at supersonic speeds. In other words, for supersonic jets the LST has supersonic velocity, while for subsonic jets the LST structures may move downstream at supersonic velocities. LST produces sound primarily at small θ for both subsonic and supersonic jets (Viswanathan, 2009). In turn, spectra dominated by LST are expected at small θ for all jet velocities. The characteristics of jet noise spectra change with respect to θ, D_j, T_j/T_a, and M (Viswanathan, 2004; Viswanathan, 2006; Viswanathan, 2009). While study of hot, low Mach number jets are limited, some trends have been observed. For example as T_j/T_a increases with a small θ, holding all else constant, the sound pressure level decreases at high frequencies, increases at low frequencies, and the spectral peak moves to lower frequencies. If T_j/T_a, D_j, and small θ are held constant and the Mach number decreases, the spectral peak narrows and shifts to lower frequencies (Viswanathan, 2009). The spectral content for Aso's fumarolic jet noise observed at $\theta = 57.6°$ are expected to show a narrowed broadband peak where the low frequencies have higher power than the high frequencies. In other words the spectral shape will not be a mirror image about the peak. This is not observed in the spectra (Fig. 3.6c, f), which suggests the spectral complexity is related to source or path effects, such as reverberations in the crater, or is related to noisy data. As the data are highly correlated for the time periods in which we scrutinize the spectra, it is more likely the spectra are influenced by source or path.

3.7.3 Topography

The propagation path was analyzed to address the spectral structure and differences observed in the data between the array elements. The topographic profiles do not show significant differences between the elements, suggesting along-path variations are not the source of spectral differences (Fig. 3.7). Fig. 3.9c and d show the smoothed spectra from Fig. 3.6f and the power spectral difference between array elements relative to element 1, respectively. In the fumarolic jet spectra there are differences in power between the array elements on the order of 15 dB and distinct peaks (Figs. 3.6c, f and 3.9c, d). For jet noise we would expect little to no power difference and a single broad peak that smoothly decays. The SWs (Fig. 3.8) and their spectra (Fig. 3.9a) show differences in power, particularly between array elements 1 and 5, but at about an order of magnitude less than the data. While the SWs spectra do not account for all the features in the spectra, there are some similar trends between the two that highlight the influence of the local topography. For example, from 0.1 to about 1 Hz the spectral shape and power in the SWs and data are similar across array elements for the synthetic and observed data, respectively. This is likely because the wavelengths are much longer than the length scale of the topographic features and as such the infrasonic waves are not heavily influenced. At frequencies higher than 1 Hz there are more peaks and increased differences in power. The structures in the spectra are consistent across array elements, particularly in the 2–10 Hz range of the data. While this could be a source characteristic, it seems unlikely, as LST jet noise spectra are smooth and we have strong evidence for gas jetting. For that frequency band the wavelengths are 34 (10 Hz) to 170 m (2 Hz) at a sound speed of 340 m/s, which is the same length scale as the crater wall. These consistent structures in the spectra are likely due to waves interacting with the crater wall. Another common trend between the SWs and the data is that at higher frequencies (2–10 Hz) the array elements 2–5 have higher power than element 1, with element 5 having the highest power. This could be due to sound reflecting off the partially collapsed pyroclastic cone and thus amplifying the signal at those frequencies. The vent geometry at Tungurahua Volcano, Ecuador has been shown to amplify the acoustic signal such that it propagates as an effective dipole (Kim et al., 2012). Fig. 3.7 suggests the pyroclastic cone located to the west-northwest of the fumarolic jet is significantly affecting sound propagation. The SPL loss is the lowest to the south and east of the jet and there is a sharp contrast in SPL along the partially collapsed pyroclastic cone wall (10 s of meter high) by about 20 dB. This suggests the sound is being reflected and amplified to

the southeast, which could explain the higher power for the more easterly array elements. The structure in the spectra may be due to the sound interacting with the crater walls and the differences in power related to near vent geometry.

While the SWs and the data have some similar trends in spectral content, they do not match. The SWs are incomplete with respect to the data, which may be due to limitations in the source waveform. However, the source at Aso is likely jet noise, which is broadband and sustained. While the SWs give an initial approximation of the sound radiation and interaction with topography, they do not fully capture the interaction of a sustained, broadband source with the local topography. Future numerical modeling will incorporate more sustained source waveforms functions. Errors or unresolved topography in the DEM may also contribute to the spectral complexity.

3.7.4 Volcanic Jet Noise

Our purpose in analyzing fumarolic jet noise is to compare it to volcanic jet noise. Unfortunately, direct comparison of the spectra is not particularly useful here as the spectra for Aso are highly complex and likely influenced by the local crater topography. However, a qualitative comparison of spectral content is valuable as well as the comparison of waveform characteristics, Strouhal numbers, and observation angles. Table 3.2 shows the acoustic features determined and observed at several volcanoes where volcanic jet noise has been recorded and for a simulated strong plume (SP) (Cerminara et al., 2016). This table highlights the variability in volcanic jets and their characteristics, as well as the limited infrasonic observations and the challenge in determining jet parameters as only four of the cases prior to this study have all the fields estimated. For the nine cases listed, all are described as sustained, broadband infrasonic signals, but each has a different peak frequency listed under, f [Hz]. Aso's frequency range falls towards the high end, but this is expected, as the jet diameter is likely one to two orders of magnitude smaller than the other examples.

Table 3.2 Comparison of Volcanic Jet Noise Characteristics

Volcano	St	D_j [m]	v_j [m/s]	D_j/v_j [s]	M	θ [deg.]	f [Hz]	r [km]	Phase	Eruptive style
Kasatochi*[a]	0.4	~750	-	~5 - 10	-	-	0.04 - 0.075	2103	Ash, gas	Plinian
Okmok**[a]	-	-	-	-	-	-	-	1706	Ash, gas	Plinian
Nabro[b]	-	-	>~330	-	>1	~1 - 45	<8	264	Ash poor, gas-rich	Vulcanian to subplinian
Karymsky[c]	-	~150	-	-	-	~92 - 108	15 - 25	2.3 - 4.1	Gas	Gas jetting
Tungurahua[d]	0.4	300 - 400	~300	~1 - 1.33	~0.9	~94 - 98	0.4	36.9	Gas, tephra, ballistics	Vulcanian, subplinian, plinian
MSH[d]	0.06	~30	~100	~0.3	~0.3	>90	0.2	13.4	Gas, tephra	Phreatic explosion
Aso***	0.19	2.5	79 - 132	0.02 - 0.03	0.3 – 0.4	57.6	6 - 10	0.22	Gas	Fumarolic gas jetting
Stromboli[e]	1.2 - 1.8	~2	335 - 432	0.0046 - 0.0060	0.98 – 1.26	60	254 - 305	0.34	Gas, bombs to ash	Strombolian to Vulcanian explosions; gas jetting
Simulated SP[f]	0.32	1406	275	5	1.8	90	~0.07	15		Plinian scenario

*Fee et al. (2010) chose St as the eruption was considered to be similar to Tungurahua.
**Fee et al. (2010) could not definitively say whether the recorded infrasound from Okmok was jet noise due to low the S/N.
***The St for Aso was chosen by the authors and not determined by independent means.
Sources: [a](Fee et al., 2010), [b](Fee et al., 2013a), [c](Rowell et al., 2014), [d](Matoza et al., 2009a), [e](Taddeucci et al., 2014), [f](Cerminara et al., 2016)

We now focus on the comparison between Aso and Tungurahua, Mount St. Helens (MSH), Stromboli, and the simulated strong plume from Cerminara et al. (2016), as these examples have all the fields in Table 3.2 and the recordings are made at relatively close ranges, unlike Kasatochi, Okmok and Nabro where the observations were made hundreds to thousands of kilometers away. Aso's angle of observation is the smallest achieved so far in volcanic jet noise studies. The Strouhal number assumed for Aso is also much higher than that of MSH and much lower than Tungurahua's, Stromboli's and the simulated case. Aso has a comparable Mach number to MSH, but much lower than Tungurahua, Stromboli and Simulated SP. While the Mach numbers for Aso and MSH are similar, the Strouhal number shows the difference in length scale between the two. Aso and Stromboli have similar diameters, but vastly different velocities, St and M values. Tungurahua and Simulated SP have much higher Strouhal and Mach numbers, as expected given the significantly larger scale of those eruptions compared to the gas jet at Aso. There are still significant variations between observed and determined jet parameters despite using high-resolution DEMs, numerical modeling, and incorporating visual and IR images. Ultimately, more field observations, simulations, and laboratory experiments are needed to improve our understanding of volcanic jet noise and parameters.

3.7.5 Jet Noise Parameters and Volatile Mass Flux

The Strouhal number for fumaroles is not known. However, the value for pure-air laboratory jet experiments was found to approach 0.19 when the jet velocity decreased towards ambient speed of sound independent of jet temperature (Tam et al., 1996). Since fumaroles are gas-only and contain no particles, we assume St = 0.19 based on the laboratory experiments (Tam et al., 1996). Assuming a Strouhal number of 0.19 results in an estimated velocity of ~ 79–132 m/s for the peak frequency range 6–10 Hz, which seems realistic. We note that St numbers of 0.06 (MSH) and 0.4 (Tungurahua) produce less realistic predictions of velocity, particularly for St = 0.06 as this estimated supersonic velocities. If the jet velocity were supersonic, we might expect supersonic spectral features such as crackle, which were not observed. By varying the Strouhal number from 0.1 to 0.3 for a peak frequency of 7 Hz, the estimated jet velocity ranges from ~ 58 to 175 m/s. These estimated velocities are reasonable and highlight the variability in estimated velocity relative to the assumed Strouhal number. In future work, constraining the St for fumaroles (using for example controlled laboratory experiments) would allow us to make more accurate estimates of velocity.

Gas flux is now estimated using the jet velocity and diameter derived from infrasound and thermal data. Table 1 shows our flux estimations for the volatile concentrations available from Shinohara et al. (2015). For comparison and validation purposes we focus on SO_2 as it is more commonly discussed and validated. Our acoustically-derived SO_2 flux of ~ 850 to 1400 t/day is high compared to that found by Shinohara et al. (2015) (200–400 t/d SO_2). However, this high SO_2 flux may be reasonable as the activity at Aso was higher in 2014–2015 than during the Shinohara et al. (2015) study period (2003–2009). From 2003 to 2005, Naka-dake crater lake level dropped and then dried up, followed by some minor ash emissions. From 2006 to 2009, the water returned to its prior level. The fumaroles along the southeastern crater wall are described as high temperature, but not as vigorous or jetting. JMA measured SO_2 flux at Aso on 6 August 2015 at an average of 1100 t/d (with 1600 t/d maximum and 800 t/d minimum detected). As seen in Fig. 3.3a, b, and c, the southeastern wall of the crater has degassing fumaroles. Recent work has shown the SSE wall fumaroles, active during this study, contribute ~ 12.5% to the total SO_2 flux for the crater (Mori, 2012). Thus we remove their contribution to the total SO_2 flux for

comparison (962.5 t/d avg., 1400 t/d max. and 700 t/d min. SO_2 flux). Aso's activity in the year prior to this study included regular strombolian and phreatic explosions. On 14 September 2015, about a month after the infrasound campaign, there was a large phreato-magmatic eruption with an ash plume reaching ~ 2 km above the crater and pyroclastic flows. Gorely Volcano, Kamchatka is similar to Aso in that they are both calderas with chains of active cones at the center, similar recent explosive activity, regular presence of acidic crater lakes and vigorous fumarolic activity from a relatively large (meter-sized) fumarole. Our estimated volatile fluxes are similar in magnitude to those recently reported for Gorely Volcano (Aiuppa et al., 2012). Error in our flux estimates could be due to the estimated velocity being too high, poorly picked peak frequencies due to the complex spectra, and low jet temperature due to a high emissivity value. The volatile concentrations in Shinohara et al. (2015) are determined from sampling the plume sourced from several fumaroles. In turn, the concentrations may inflate our flux estimates for just one fumarole.

3.7.6 Fumaroles and Future Volcanic Jet Noise Research

The motivation for this project and investigating fumarolic jet noise was to see if fumaroles could be used as proxies for larger volcanic jets as they more closely mimic the complex, high temperature, volcanic jet than a laboratory jet does. The jet noise at Aso was low amplitude in the infrasound band with energy concentrated at higher frequencies. Higher frequencies (shorter wavelengths) are more influenced by local topography. In turn, path effects are present in the recorded data and their spectra, making comparisons between fumarolic and laboratory high frequency jet noise difficult. At Aso the topography afforded a smaller observation angle, but added complexity to the spectra. Perhaps this is the trade-off between noise and observation angle until we can better account for a sustained, broadband, higher frequency source interacting with local topography. Although they occur less frequently, larger jets with longer wavelengths observed at higher angles may be simpler to investigate for future studies. Another suggested natural test jet are geysers (Demonte and Johnson, 2013). Geysers have been recorded with microphone arrays in Yellowstone National Park, but the multiphase fluid jetting geysers observed were found to be inefficient at perturbing the atmosphere, particularly in the infrasonic band (Johnson et al., 2013). In the same study, some more energetic jetting geysers were observed for a short duration and found to have lower power in the infrasonic band and higher in

the acoustic. This suggests geysers may be good analog volcanic jets, but may have similar challenges with topographic features complicating the acoustic wavefield.

3.8 Conclusions

We have characterized a fumarolic jet at Aso Volcano, Japan using infrasonic and TIR observations. The jet noise produced by a gas jetting fumarole in Naka-dake crater is low amplitude, sustained, and broadband (0.5 to 25 + Hz). These acoustic observations were made at an unusually small angle to the jet axis (57.6°) at relatively close range (~ 220 m). The spectra were complex with significant structure and power differences likely due to the large, complex crater and near vent topography. Numerical waveforms were computed to investigate this complexity; however frequency limitations and a simple source time function did not fully account for the propagation and reverberation of a sustained, broadband source within a crater. Even given the complex spectra, we derived a reasonable jet velocity (79–132 m/s) using TIR images and acoustic data. For future work, it will be important to have an additional data source such as TIR video or high-speed imaging as used by Taddeucci et al. (2014) to estimate jet velocity in order to independently determine the Strouhal number as it is valuable for comparison. Using these values we estimated the total volatile flux at ~ 14,000 to 23,000 t/day with ~ 850 to 1,400 t/day in SO_2. While these fluxes are high compared to previous measurements at Aso, the current activity was also higher and our estimates are similar to similar volcanoes worldwide. This marks the first volatile flux estimates using recorded volcanic jet noise with an assumed St and TIR data. Future studies can incorporate more detailed estimates of jet properties, such as composition and velocity, by simultaneously deploying infrasonic microphones across a greater angular range, TIR high-speed video and UV camera. The combination of these data would enable independent estimates of jet velocity with the TIR video and SO_2 flux with the UV camera, which could be combined with infrasound data to estimate *St* directly.

3.9 Acknowledgments

The authors extend a special thank you to Yu-Chih Huang, Shin Yoshikawa, Mitsuru Utsugi, Takuto Minami, and Takahiro Ohkura, and the AVL for their assistance with fieldwork. Thank you to T. Kazama and T. Ohkura for sharing the March 2015 and the May 2015 1 m-resolution

DEMs of Nakadake crater, respectively. The 2012 1 m and 5 m resolution DEMs were provided by the Geospatial Information Authority of Japan. Thank you to Guy Tytgat for teaching K.M. to solder and in help preparing the equipment. Thank you to Taryn Lopez for discussing volatile flux with K.M. This work was supported by the Japan Society for the Promotion of Science and the National Science Foundation, specifically NSF grants EAPSI-1515624 and NSF-EAR-1113294. Helpful reviews from Wes Thelen and an anonymous reviewer greatly improved the manuscript.

3.10 References

Aiuppa A., Giudice G., Liuzzo M., Tamburello G., Allard P., Calabrese S., Chaplygin I., McGonigle A.J.S. and Taran Y., First volatile inventory for Gorely volcano, Kamchatka, Geophys. Res. Lett. 39 (6), 2012, 1–5, http://dx.doi.org/10.1029/2012gl051177

Allaby A. and Allaby M., A dictionary of earth sciences, In: Allaby A. and Allaby M., (Eds.), Oxford Paperback Reference, 2003, Oxford University Press; Oxford.

Cerminara M., Esposti Ongaro T. and Neri A., Large Eddy simulation of gas-particle kinematic decoupling and turbulent entrainment in volcanic plumes, J. Volcanol. Geotherm. Res. 2016, 1–29, http://dx.doi.org/10.1016/j.jvolgeores.2016.06.018

De Angelis S., Lamb O.D., Lamur A., Hornby A.J., von Aulock F.W., Chigna G., Lavallée Y. and Rietbrock A., Characterization of moderate ash-and-gas explosions at Santiaguito volcano, Guatemala, from infrasound waveform inversion and thermal infrared measurements, Geophys. Res. Lett. 2016, 1–8, http://dx.doi.org/10.1002/2016GL069098

Demonte P.J. and Johnson J.B., Characterization and Quantification of Geyser Eruptions: Insights From Infrasound Monitoring at Yellowstone National Park IAVCEI Scientific Assembly, 2013, (pp. 1-1).

Depuru Mohan N.K., Prakash K.R. and Panchapakesan N.R., Mixing augmentation by multiple lobed jets, Am. J. Fluid Dyn. 5 (2), 2015, 55–64, http://dx.doi.org/10.5923/j.ajfd.20150502.03

Fee D. and Matoza R.S., An overview of volcano infrasound: from Hawaiian to Plinian, local to global, J. Volcanol. Geotherm. Res. 249, 2013, 123–139, http://dx.doi.org/10.1016/j.jvolgeores.2012.09.002

Fee D., Garces M. and Steffke A., Infrasound from Tungurahua Volcano 2006–2008: strombolian to plinian eruptive activity, J. Volcanol. Geotherm. Res. 193 (1–2), 2010a, 67–81, http://dx.doi.org/10.1016/j.jvolgeores.2010.03.006

Fee D., Steffke A. and Garces M., Characterization of the 2008 Kasatochi and Okmok eruptions using remote infrasound arrays, J. Geophys. Res. 115, 2010b, http://dx.doi.org/10.1029/2009jd013621

Fee D., Matoza R.S., Gee K.L., Neilsen T.B. and Ogden D.E., Infrasonic crackle and supersonic jet noise from the eruption of Nabro Volcano, Eritrea, Geophys. Res. Lett. 40 (16), 2013, 4199–4203, http://dx.doi.org/10.1002/grl.50827

Fee D., Yokoo A. and Johnson J.B., Introduction to an open community infrasound dataset from the actively erupting Sakurajima Volcano, Japan, Seismol. Res. Lett. 2014, http://dx.doi.org/10.1785/0220140051

Fee D., Haney M.M., Matoza R.S., Van Eaton A.R., Cervelli P., Schneider D.J. and Iezzi A.M., Volcanic tremor and plume height hysteresis from Pavlof Volcano, Alaska, Science 355 (6320), 2017, 45–48, http://dx.doi.org/10.1126/science.aah6108

Fischer T.P., Fluxes of volatiles (H2O, CO2, N2, Cl, F) from arc volcanoes, Geochem. J. 42 (1), 2008, 21–38, http://dx.doi.org/10.2343/geochemj.42.21

Goto A., Ripepe M. and Lacanna G., Wideband acoustic records of explosive volcanic eruptions at Stromboli: new insights on the explosive process and the acoustic source, Geophys. Res. Lett. 41 (11), 2014, 3851–3857, http://dx.doi.org/10.1002/2014GL060143

Johnson J.B. and Ripepe M., Volcano infrasound: a review, J. Volcanol. Geotherm. Res. 206 (3–4), 2011, 61–69, http://dx.doi.org/10.1016/j.jvolgeores.2011.06.006

Johnson J.B., Anderson J.F., Anthony R.E. and Sciotto M., Detecting geyser activity with infrasound, J. Volcanol. Geotherm. Res. 256, 2013, 105–117, http://dx.doi.org/10.1016/j.jvolgeores.2013.02.016

Kaneko K., Kamata H., Koyaguchi T., Yoshikawa M. and Furukawa K., Repeated large-scale eruptions from a single compositionally stratified magma chamber: an example from Aso volcano, Southwest Japan, J. Volcanol. Geotherm. Res. 167, 2007, http://dx.doi.org/10.1016/j.jvolgeores.2007.05.002

Kaneshima S., Kawakatsu H., Matsubayashi H., Sudo Y., Tsutsui T., Ohminato T., Ito H., Uhira K., Yamasato H., Oikawa J., Takeo M. and Iidaka T., Mechanism of phreatic eruptions at Aso Volcano inferred from near-field broadband seismic observations, Science 273, 1996, 642–645, http://dx.doi.org/10.1126/science.273.5275.642

Kim K. and Lees J.M., Finite-difference time-domain modeling of transient infrasonic wavefields excited by volcanic explosions, Geophys. Res. Lett. 38 (L06804), 2011, http://dx.doi.org/10.1029/2010gl046615

Kim K. and Lees J., Local volcano infrasound and source localization investigated by 3D simulation, Seismol. Res. Lett. 2014, http://dx.doi.org/10.1785/0220140029

Kim K., Lees J.M. and Ruiz M., Acoustic multipole source model for volcanic explosions and inversion for source parameters, Geophys. J. Int. 191, 2012, 1192–1204, http://dx.doi.org/10.1111/j.1365-246X.2012.05696.x

Kim K., Fee D., Yokoo A. and Lees J.M., Acoustic source inversion to estimate volume flux from volcanic explosions, Geophys. Res. Lett. 42 (13), 2015, 5243–5249, http://dx.doi.org/10.1002/2015GL064466

Kundu P.K. and Cohen I.M., Fluid Mechanics, 2008, Academic Press.

Lacanna G. and Ripepe M., Influence of near-source volcano topography on the acoustic wavefield and implication for source modeling, J. Volcanol. Geotherm. Res. 250, 2013, 9–18, http://dx.doi.org/10.1016/j.jvolgeores.2012.10.005

Lee D.-C., Olson J.V. and Szuberla C.A.L., Computationally robust and noise resistant numerical detector for the detection of atmospheric infrasound, J. Acoust. Soc. Am. 134 (1), 2013, 862–868, http://dx.doi.org/10.1121/1.4807802

Lighthill M.J., On sound generated aerodynamically. I. General theory, Proc. R. Soc. Lond. A 211 (1107), 1952, 564–587, http://dx.doi.org/10.1098/rspa.1952.0060

Lillesand T.M., Kiefer R.W. and Chipman J.W., Remote Sensing and Image Interpretation, 2008, John Wiley & Sons, Inc.; USA, (756 pp).

Lopez T.M., Fee D., Prata F. and Dehn J., Characterization and interpretation of volcanic activity at Karymsky Volcano, Kamchatka, Russia, using observations of infrasound, volcanic emissions, and thermal imagery, Geochem. Geophys. Geosyst. 14 (12), 2013, 5106–5127, http://dx.doi.org/10.1002/2013GC004817

Lopez, T.M., Tassi, F., Aiuppa, A., Galle, B., Rizzo, A., Fiebig, J., Capecchiacci, F., Giudice, G., Caliro, S., Ketner, D., Tamburello, G. and Paskievitch, J.F.. Geochemical constraints on volatile sources and subsurface conditions at Mount Martin, Mount Mageik, and Trident Volcanoes, Katmai Volcanic Cluster, Alaska. J. Volcanol. Geotherm. Res. (in prep).

Marcillo O. and Johnson J.B., Tracking near-surface atmospheric conditions using an infrasound network, J. Acoust. Soc. Am. 128 (1), 2010, 14–19, http://dx.doi.org/10.1121/1.3442725

Matoza R.S., Fee D., Garcés M.A., Seiner J.M., Ramón P.A. and Hedlin M.A.H., Infrasonic jet noise from volcanic eruptions, Geophys. Res. Lett. 36 (8), 2009, http://dx.doi.org/10.1029/2008gl036486

Matoza R.S., Fee D. and Garces M.A., Infrasonic tremor wavefield of the Pu'u 'O'o crater complex and lava tube system, Hawaii, in April 2007, J. Geophys. Res. Solid Earth 2010, 115, http://dx.doi.org/10.1029/2009jb007192

Matoza R.S., Fee D., Neilsen T.B., Gee K.L. and Ogden D.E., Aeroacoustics of volcanic jets: acoustic power estimation and jet velocity dependence, J. Geophys. Res. 118, 2013, 6269–6284, http://dx.doi.org/10.1002/2013JB010303

McKee K., Fee D., Rowell C. and Yokoo A., Network-based evaluation of the infrasonic source location at Sakurajima Volcano, Japan, Seismol. Res. Lett. 85 (6), 2014, 1200–1211, http://dx.doi.org/10.1785/0220140119

Mori T., Measurement of SO2 flux ratio between two plumes of the 1st crater of Nakadake, Aso volcano, Japan, Chikyu 34, 2012, 732–737.

Prieto G.A., Parker R.L., Thomson D.J., Vernon F.L. and Graham R.L., Reducing the bias of multitaper spectrum estimates, Geophys. J. Int. 171 (3), 2007, 1269–1281, http://dx.doi.org/10.1111/j.1365-246X.2007.03592.x

Pritchard P.J., Dimensional Analysis and Similitude, Fox and McDonald's Introduction to Fluid Mechanics, 2011, John Wiley & Sons, Inc.; Hoboken, NJ, 290–327

Rowell C., Fee D., Szuberla C.A., Arnoult K.M., Matoza R.S., Firstov P.P., Kim K. and Makhumdov E., Three-dimensional volcano-acoustic source localization at Karymsky Volcano, Kamchatka, Russia, J. Volcanol. Geotherm. Res. 283, 2014, 101–115, http://dx.doi.org/10.1016/j.jvolgeores.2014.06.015

Shinohara H., Yoshikawa S. and Miyabuchi Y., Degassing Activity of a Volcanic Crater Lake: Volcanic Plume Measurements at the Yudamari Crater Lake, Aso Volcano, Japan, Volcanic Lakes, 2015, Springer; Berlin Heidelberg, 201–217.

Taddeucci J., Sesterhenn J., Scarlato P., Stampka K., Del Bello E., Fernandez J.J.P. and Gaudin D., High-speed imaging, acoustic features, and aeroacoustic computations of jet noise from strombolian (and vulcanian) explosions Geophys. Res. Lett. 41 (9), 2014, 3096–3102, http://dx.doi.org/10.1002/2014GL059925

Takagi N., Kaneshima S., Kawakatsu H., Yamamoto M., Sudo Y., Ohkura T., Yoshikawa S. and Mori T., Apparent migration of tremor source synchronized with the change in the tremor amplitude observed at Aso volcano, Japan, J. Volcanol. Geotherm. Res. 154 (3–4), 2006, 181–200, http://dx.doi.org/10.1016/j.jvolgeores.2006.02.001

Tam C.K.W., Supersonic jet noise, Annu. Rev. Fluid Mech. 27, 1995, 17–43, http://dx.doi.org/10.1146/Annurev.Fl.27.010195.000313

Tam C.K.W., Jet noise: since 1952, Theor. Comput. Fluid Dyn. 10, 1998, 393–405, http://dx.doi.org/10.1007/s001620050072

Tam C.K.W. and Burton D.E., Sound generated by instability waves of supersonic flows. 2. Axisymmetric jets, J. Fluid Mech. 138 (Jan), 1984, 273–295, http://dx.doi.org/10.1017/S0022112084000124

Tam C.K.W. and Chen P., Turbulent mixing noise from supersonic jets, AIAA J. 32 (9), 1994, 1774–1780, http://dx.doi.org/10.2514/3.12173

Tam C.K.W., Golebiowski M. and Seiner J.M., On the two components of turbulent mixing noise from supersonic jets, AIAA J. 1996, 1–19, http://dx.doi.org/10.2514/6.1996-1716

Tam C.K.W., Viswanathan K., Ahuja K.K. and Panda J., The sources of jet noise: experimental evidence, J. Fluid Mech. 615, 2008, 253–292, http://dx.doi.org/10.1017/S0022112008003704

Thelen W.A. and Cooper J., An Analysis of Three New Infrasound Arrays Around Kīlauea Volcano, 2015, 1253–2014, http://dx.doi.org/10.3133/ofr20141253.

Thomson D.J., Spectrum estimation and harmonic analysis, Proc. IEEE 70 (9), 1982, 1055–1096, http://dx.doi.org/10.1109/PROC.1982.12433

Viswanathan K., Aeroacoustics of hot jets, J. Fluid Mech. 516, 2004, 39–82, http://dx.doi.org/10.1017/S0022112004000151

Viswanathan K., Scaling laws and a method for identifying components of jet noise, AIAA J. 44 (10), 2006, 2274–2285, http://dx.doi.org/10.2514/1.18486

Viswanathan K., Mechanisms of jet noise generation: classical theories and recent developments, Int. J. Aeroacoust. 8 (4), 2009, 355–407, http://dx.doi.org/10.1260/147547209787548949.

Walker K.T. and Hedlin M.A.H., A review of wind-noise reduction methodologies, In: Le Pichon A., Blanc E. and Hauchecorne A., (Eds.), Infrasound Monitoring for Atmospheric Studies, 2009, Springer Netherlands, 141–182

Wallace P.J., Volatiles in subduction zone magmas: concentrations and fluxes based on melt inclusion and volcanic gas data, J. Volcanol. Geotherm. Res. 140 (1), 2005, 217–240, http://dx.doi.org/10.1016/j.jvolgeores.2004.07.023

Woulff G. and McGetchin T.R., Acoustic noise from volcanoes: theory and experiment, Geophys. J. Res. 45, 1976, 601–616, http://dx.doi.org/10.1111/j.1365-246X.1958.tb05346.x

Yokoo A. and Miyabuchi Y., Eruption at the Nakadake 1st crater of Aso Volcano started in November 2014, Bull. Volc. Soc. Japan 60 (2), 2015, 275–278, http://dx.doi.org/10.18940/kazan.60.2_275

Yokoo A. and Taniguchi H., Application of video image processing to detect volcanic pressure waves: a case study on archived images of Aso volcano, Japan, Geophys. Res. Lett. 31 (23), 2004, http://dx.doi.org/10.1029/2004gl021183

Yokoo A., Iguchi M., Tameguri T. and Yamamoto K., Processes prior to outbursts of Vulcanian eruption at Showa Crater of Sakurajima Volcano, Bull. Volc. Soc. Japan 58 (1), 2013, 163–181, http://dx.doi.org/10.18940/kazan.58.1_163

Chapter 4

Infrasound signal detection and back-azimuth estimation using ground-coupled airwaves on a seismo-acoustic sensor pair[3]

4.1 Abstract

We present an infrasonic signal detection and back-azimuth determination technique that requires just one microphone and one three-component seismometer. Ground-coupled airwaves (GCAs) occur when an incident atmospheric acoustic wave impinges on the ground surface and is partially transmitted as a seismic wave. GCAs are commonly detected hundreds of kilometers away on seismic networks and are observed to have retrograde particle motion. Horizontally propagating acoustic waves and GCAs have previously been observed on collocated infrasound and seismic sensor pairs as coherent with a 90° phase difference. If the sensors are spatially separated, an additional propagation-induced phase shift is present. The additional phase shift depends on the direction from which the acoustic wave arrives, as each back-azimuth has a different apparent distance between the sensors. We use the additional phase shift, the coherence, and the characteristic particle motion on the 3-component seismometer to determine GCA arrivals and their unique back-azimuth. We test this technique with synthetic seismo-acoustic data generated by a coupled Earth-atmosphere 3D finite-difference code, as well as two seismo-acoustic datasets from Mount St. Helens and Mount Pagan volcanoes. Results from our technique compare favorably with traditional infrasound array processing and provide robust GCA detection and back-azimuth determination. Assuming adequate station spacing and sampling, our technique provides a new and robust method to detect infrasonic signals and determine their back-azimuth, and may be of practical benefit where resources are limited and large sensor networks or arrays are not feasible.

4.2 Introduction

A common goal of the infrasound community is to detect and determine the direction (back-azimuth) from which a signal originated. Typical infrasonic array deployments consist of at least

[3] McKee, K., D. Fee, M. Haney, R. S. Matoza, and J. J. Lyons, (submitted), Infrasound signal detection and back-azimuth estimation using ground-coupled airwaves on a seismo-acoustic sensor pair, *Journal of Geophysical Research: Solid Earth*

three, and usually four to eight, infrasonic microphones distributed on the ground surface to detect and determine the back-azimuth of low frequency acoustic waves [*Christie and Campus*, 2009]. *Green* [2015] shows examples of International Monitoring System (IMS) infrasound arrays deployed with apertures ranging from 1 to 4 km as of March 2014. Traditional methods for detecting and determining back-azimuth to a source are executed in two steps [*Olson and Szuberla*, 2008]. First, frequency-wavenumber (F-k) analysis (similar to delay and sum beamforming in the time domain) or least squares estimation of a plane wave arrival [*Olson and Szuberla*, 2005] is used to determine the back-azimuth for each window of data. The waves are assumed to be planar. Then methods such as Fisher's F-statistic [*Olson and Szuberla*, 2008; *Smart and Flinn*, 1971] or mean cross-correlation maxima (MCCM) [*Lee et al.*, 2013] are used to assess whether the data analyzed in each window are highly correlated and can be deemed a detection. The Progressive Multi-Channel Correlation (PMCC) algorithm combines detection and characterization of a signal. PMCC cross-correlates the data from array subsets (triads), computes time delays, and uses the sum of time delays between unique sensor pairs within a triad to establish a closure relationship, [*Cansi*, 1995; *Cansi and Klinger*, 1997]. The analysis progresses as triads are combined to create larger groups. If the closure relationship for a given window of data holds through combining triads then the signal back-azimuth and velocity estimate becomes increasingly accurate. PMCC is applied for a given time window across multiple frequency bands and then advanced to the next window. These methods are conducted using arrays of three or more infrasonic microphones.

A frequently observed phenomenon in infrasonic wave propagation is when an incident acoustic wave traveling through the atmosphere encounters the Earth's surface and part of the wave energy is transferred to the ground as a seismic wave, known as a ground-coupled airwave (GCA). GCAs from a variety of sources including volcanoes, bolides, meteors, and explosions are regularly detected on seismometers [*De Angelis et al.*, 2012; *Edwards et al.*, 2007; *Fee et al.*, 2016; *Fee et al.*, 2017; *Ichihara et al.*, 2012; *Johnson and Malone*, 2007; *Langston*, 2004; *Matoza and Fee*, 2014; *Smith et al.*, 2016; *Tauzin et al.*, 2013; *Walker et al.*, 2010]. Here we present a method to determine the back-azimuth to an acoustic source detected on a nearly collocated 3-component seismometer and infrasonic microphone. This method requires less instrumentation than a traditional infrasonic array. In this manuscript, we describe the GCA

back-azimuth determination (BAD) method, test it using synthetic data from a coupled Earth-atmosphere 3D finite-difference code, and then apply it successfully to two volcanic datasets: Mount St. Helens, USA and Mount Pagan, Commonwealth of the Northern Mariana Islands (CNMI). These applications are followed by a discussion of best practices for using the method.

4.3 Background

In the case where an incident acoustic wave encounters the ground nearly parallel to the surface, referred to as 'grazing incidence' [*Ben-Menahem and Singh*, 2000], the wave couples to the ground and travels through the Earth at approximately the speed of sound in the atmosphere, ~343 m/s. The seismic particle motion is retrograde and elliptical since it is a guided interface wave and it is detectable on a 3-component seismometer [*Edwards et al.*, 2007; *Ichihara et al.*, 2012]. As the particle motion is retrograde, it is recorded on the vertical and horizontal components and points, roughly, back to the source. If the angle of incidence is closer to vertical, the incident pressure wave can induce a P wave and subsequently S and Rayleigh waves, which travel through the subsurface at their respective speeds. This was clearly observed with the breakup of the Chelyabinsk meteor [*Tauzin et al.*, 2013]. The focus of this manuscript is the more typical case where atmospheric pressure waves couple to the Earth at angles near 90° from vertical.

Recent work has shown that in acoustic time-series data, signals may be distinguished from wind noise by cross-correlating the acoustic data with that from a nearly collocated seismometer [*Ichihara et al.*, 2012]. The key factor that makes this possible is separating the microphone and seismometer by a distance greater than the correlation length of wind noise. *Ichihara et al.* [2012] accomplished this by attaching a 4 m long pipe to the microphone, effectively separating the seismic and infrasonic sensors. The separation distance required is dependent upon the frequency of interest and wind speed. Wind noise recorded on two sensors will correlate at a given frequency, f, if the interstation distance is one third or less than the wind eddy size (v/f), where v is the wind speed [*Shields*, 2005; *Wilson et al.*, 2007]. By separating the sensors by more than this distance the incident pressure wave will still correlate because the acoustic wavelengths at the same frequency, (c/f), where c is speed of sound, are much longer. For

example, an infrasonic wavelength at 1 Hz is ~343 m and eddy size for a ~3 m/s wind at the same frequency is 3 m.

Ichihara et al. [2012] propose that the dominant terms in the seismic-acoustic cross-correlation function are the incident acoustic pressure wave, p_{in}, and the vertical ground velocity generated by the acoustic pressure wave, $H_{pw}p_{in}$, where H_{pw} is the transfer coefficient. From *Ben-Menahem and Singh* [2000], assuming the incident acoustic wave propagates along the surface, the transfer coefficient can be estimated using:

$$H_{pw} = \frac{e^{-i\pi/2}c_a}{2(\lambda+\mu)}\frac{\lambda+2\mu}{\mu}$$

where λ and μ are the Lamé parameters of the solid medium and c_a is the apparent acoustic phase velocity. If the airwave arrives nearly horizontal to the ground surface, then the apparent velocity will be equal to the sound speed. The $e^{-i\pi/2}$ indicates that the vertical ground velocity generated by the acoustic pressure wave has a 90° phase shift relative to the acoustic pressure wave. The 90° phase shift corresponds to the case when the sensors are collocated. As mentioned, the ability to distinguish signals requires that the sensors be separated such that wind noise is uncorrelated and incoherent. This separation creates an additional time shift between the signals which must be corrected in order for the 90° phase to become apparent [*Matoza and Fee*, 2014]. The additional phase can be removed if the sensor pair geometry, back-azimuth to the source, and apparent velocity are known. When the seismic and acoustic data are cross-correlated this shift is present as a time delay and may indicate coherent acoustic waves as opposed to noise. In applying this method, *Ichihara et al.* [2012] filtered the seismic and acoustic waveforms from 1 – 7 Hz to ensure that given the inter-sensor spacing the wind noise would not correlate. One challenge with the cross-correlation method is that the frequency band in which two signals correlate may be narrow and is unknown a priori. This requires a systematic search over many different frequency bands to find the one in which the signals correlate. To address this, *Matoza and Fee* [2014] looked at the coherence spectra of the unfiltered seismic and acoustic data to find frequencies at which the waveforms correlate.

Coherence provides an intuitive measure of how similar two time series are with respect to their frequency content, with 0 being dissimilar and 1 being identical. The coherence spectrogram is a

measure of this similarity taken in windows through time (similar to a spectrogram). In this same manner, *Matoza and Fee* [2014] analyzed the phase spectrogram, which is the phase between two time series at different frequencies also taken in windows through time. *Matoza and Fee* [2014] analyzed GCAs on nearly collocated acoustic and seismic stations, and looked at the coherence and phase delays in three different datasets: Mount St. Helens, Washington, USA; Tungurahua, Ecuador; and Redoubt, Alaska, USA. The method worked well with the Mount St. Helens data, detecting ~2000 seconds of coherent signal above the background seismic activity. Once the phase shift was corrected for the offset between stations, the phase difference between the seismic and acoustic was near 90°. At Tungurahua, the method again detected coherent signal, but it did not for the Redoubt dataset. The incoherence found in the Redoubt data is likely due to distinct acoustic and seismic sources [*Matoza and Fee*, 2014]. This highlights the fact that coupling does not always occur or is not always dominant/detectable. GCAs from the 2016 eruption at Pavlof Volcano, USA were also identified on EarthScope Transportable Array (TA) sites in Alaska using coherence [*Fee et al.*, 2017].

We note there are a variety of factors that influence the ability of an acoustic wave to couple to the ground. Frequency-dependent, near-surface geological site effects (as the transfer coefficient equation previously stated is for a homogeneous, solid half-space [*Ben-Menahem and Singh*, 2000]), incidence angle, and range dependence (because higher-frequency content is preferentially attenuated) are all thought to be important influences. Other factors include seismometer burial depth, topography, frequency content, and observation distance [*Edwards et al.*, 2007; *Madshus et al.*, 2005].

4.4 Infrasonic source back-azimuth determination (BAD) method

4.4.1 Distinguishing the infrasonic contribution to a seismic record

First we describe the method for distinguishing the infrasonic component of the seismic record (i.e. GCA) and identifying the 90° phase shift. Given the geometry of a source and nearly collocated seismometer and microphone, we can identify the signal from a specific source direction by correcting the phase due to the apparent sensor separation [*Matoza and Fee*, 2014]. We refer to this process as the "forward problem" and Figure 1 shows a schematic of the six necessary steps, as outlined in Matoza and Fee [2014]. In this example, a plane wave arrives

from a volcanic source to the southeast. To find the additional phase shift, we need to find the apparent distance between the two sensors. We define azimuth as the angle measured clockwise from north (0°) from one location to another and back-azimuth as the direction from which a wave originated, again measured clockwise from north. In step 1 we measure the azimuth from the seismometer (orange square) to the microphone (green circle), β, and in step 2 we determine the azimuth to the source, α (Fig. 1). Then we find the difference in these two azimuths, θ, which is the angle between the inter-sensor distance, d, and the apparent distance, d_0. We apply trigonometry to find d_0, one of the legs of a right-angled triangle (Fig. 1, Step 3). The apparent distance is used to calculate the travel time difference from the microphone to seismometer, which appears as a time shift, Δt. $\Delta t = d_0/c$, where c is the speed of sound assuming a plane wave traveling near parallel to the surface (Fig. 1, Step 4). Next, we shift the acoustic data by the calculated Δt (Fig. 1, Step 5), which effectively collocates the sensors relative to the incident wave and minimizes the phase offset due to sensor separation. Δt is related to phase through the equation $\varphi = 2\pi \times f \times \Delta t$, where φ is phase and f is frequency. Once Δt is applied to the acoustic data and the phase is calculated, the 90° phase should be present in the phase spectrogram (Fig. 1, Step 6). The presence of the 90° phase indicates the coherent wave is from the back-azimuth, α, which is equivalent to $\beta + \theta$.

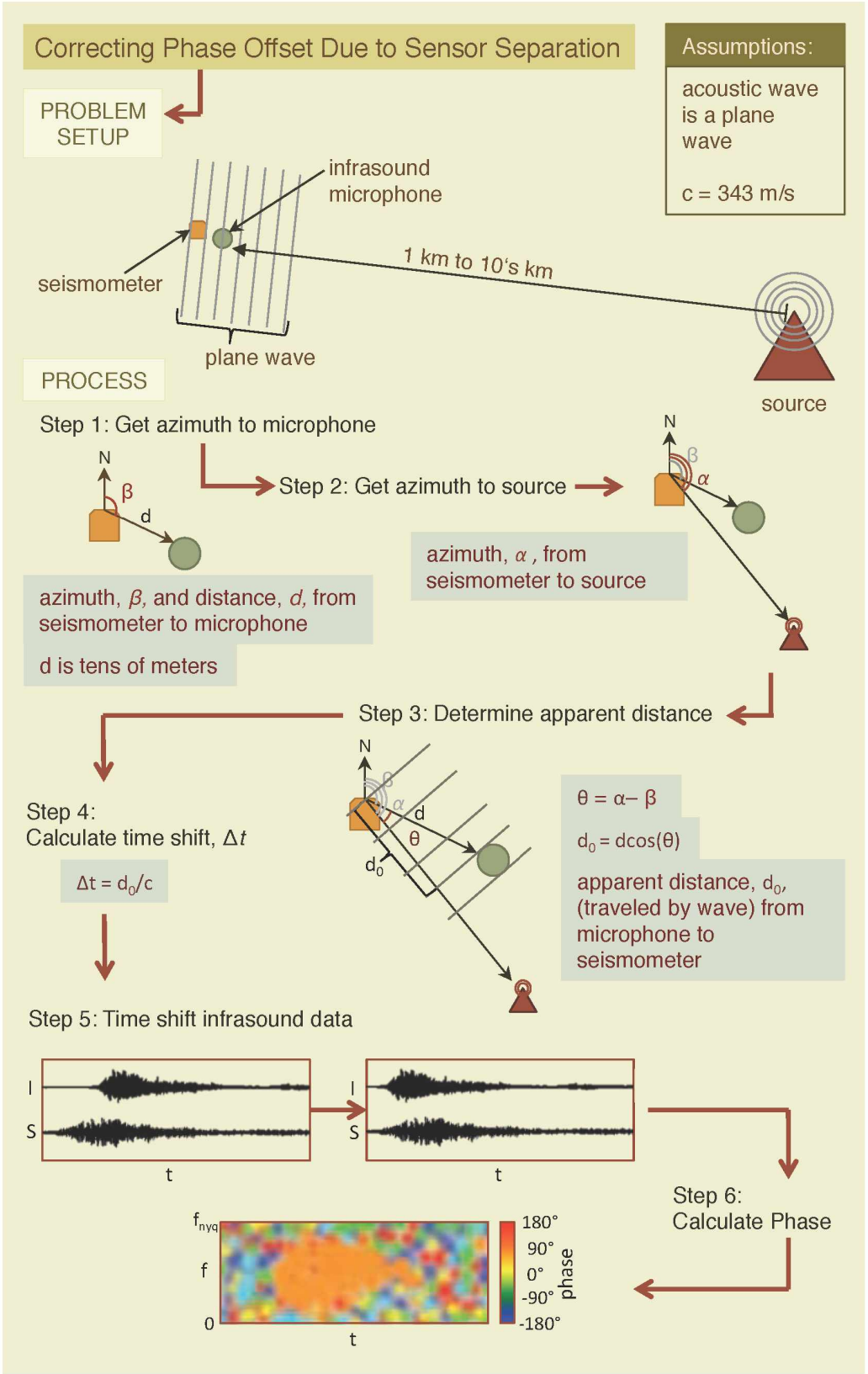

Figure 4.1 Infographic illustrating the steps to correct the phase offset between infrasound and seismic data for a recorded airwave due to sensor separation. Method is from Matoza and Fee [2014]. See text for more details.

4.4.2 Ground-couple Airwave Back-azimuth Determination method

Here we describe our methodology to determine the back-azimuth of an incident acoustic wave recorded on a seismo-acoustic sensor pair. The inter-sensor distance, d, and the azimuth from seismometer to the infrasonic microphone, β, are determined from the locations of the sensors (Fig. 2, Step 1). We can determine the times and frequencies in which the seismic and acoustic waveforms are similar by evaluating the coherence. If the seismic trace is dominated by a GCA, shown by the seismic-acoustic coherence, the phase should be 90°. This means the observed phase, ρ, is a sum of the 90° phase and the additional phase from the sensor separation, ρ_{d_0}. To determine the back-azimuth to the source, we need to find the time shift that minimizes the additional phase from the sensor separation. However, this time shift does not determine a unique back-azimuth as the same apparent distance, and thus time shift, can be found about the line connecting the seismometer and microphone, d (Fig. 2, Step 1). This non-unique solution exists for 2-element infrasound arrays as well. Thus, additional information is needed to resolve a unique solution, such as the particle motion from the seismometer. As GCAs normally have retrograde particle motion in the direction of propagation [*Aki and Richards*, 2002; *Ben-Menahem and Singh*, 2000; *Edwards et al.*, 2008; *Edwards et al.*, 2007], a rough estimate of the back-azimuth can be calculated [*Edwards et al.*, 2007; *Montalbetti and Kanasewich*, 1970; *Neuberg and Pointer*, 2000; *Vidale*, 1986; *Wang and Kaveh*, 1985] and used to determine a unique solution from the multiple back-azimuths derived in previous steps. Figure 2 and the following paragraphs describe this method in more detail.

In order to determine the back-azimuth from a seismo-acoustic pair, we assume the incident acoustic pressure wave is a plane wave traveling at the speed of sound in the atmosphere, ~343 m/s, the local sound speed at 20°C with negligible wind. We also assume the wave couples to the ground and the phase is 90° when the sensors are collocated. This assumption is supported by theory [*Ben-Menahem and Singh*, 2000] and observations [*Ichihara et al.*, 2012; *Matoza and Fee*, 2014]. Seismic and acoustic data are pre-processed by removing the instrument responses and high-pass filtering above 20 s to remove long-period noise and drift. We then calculate the azimuth from seismometer to microphone, β (Fig. 2, Step 1). For simplicity, and to maintain consistency throughout, we have chosen to apply this method relative to the seismometer, such

that azimuths are relative to the seismometer's location and north. The distance from the seismometer to the microphone is d. Next, we calculate the coherence spectrogram by taking coherence in windows of the infrasound and seismic data with 90% overlap (Fig. 2, Step 2). Window lengths are dependent on the signal length of interest. We chose window lengths to capture multiple waveform periods for broadband data and to allow for many windows over the duration of the signal. For example, we use a 4 s window for the synthetic dataset as the signal was ~5 s in duration, but we use a 10 s window for the MSH and Pagan datasets which are ~1850 s and ~30 s in duration, respectively. Next we calculate the peak coherence and use it to select a time window for further analysis (Fig. 2, Step 3). For each time step (column) of the coherence spectrogram, we take windows of the coherence relative to frequency with a 90% overlap and determine the mean for each window of frequency from zero to the Nyquist frequency. We use a window of ~1 Hz for the synthetic data and ~2 Hz for the MSH and Pagan data. Then we save the maximum mean coherence value from those windows and repeat for each coherence time step. Peak coherence values above a set threshold indicate coherent GCA arrivals; here we use a threshold of 0.8.

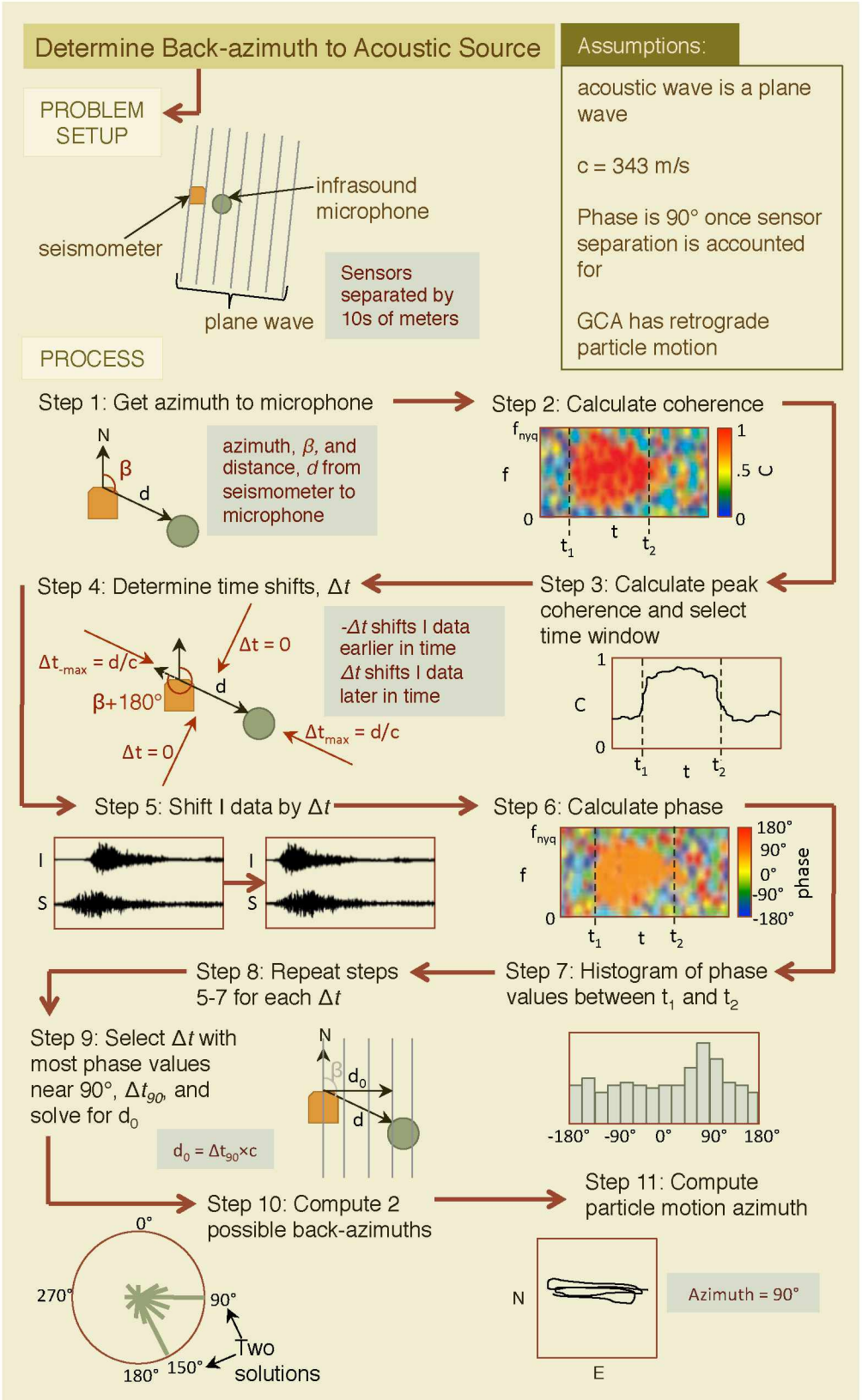

Figure 4.2 Infographic illustrating the steps to determine the back-azimuth to an acoustic source that has been recorded by nearly collocated seismic and infrasonic sensors. See text for more details.

The next step is to determine the time shifts, Δt, to search over for the two back-azimuth solutions (Fig. 2, Step 4). The maximum travel time between the seismic and infrasonic sensors is d/c, where the wavefront is perpendicular to d and the back-azimuth is either β or $\beta + 180°$. The minimum, then, is 0, where the wavefront is parallel to d and the back-azimuth is either $\beta + 90°$ or $\beta - 90°$. Thus, we search from $-\Delta t_{max} = -d/c$ to $\Delta t_{max} = d/c$, where each Δt has two possible back-azimuths and $-\Delta t_{max}$ to Δt_{max} covers azimuths 0° to 360°. We use an interval step of $dt/4$ as this gave the best results for the three datasets evaluated. Next we search for possible back-azimuths by calculating the phase spectrogram for each time shift. To do this we shift the infrasound data by the first Δt (Fig. 2, Step 5) and calculate the phase spectrogram between the seismic and time-shifted infrasound trace (Fig. 2, Step 6). Then we analyze the phase values by taking a histogram of phase values between t_1 and t_2 from zero to the Nyquist frequency (Fig. 2, Step 7). We set our bin widths at 3° from -180° to 180°. Next we save the number of values in bins closest to 90°; the bins of interest for our bin width is 87° to 90° and 90° to 93°. We repeat steps 5-7 for each Δt (Fig. 2, Step 8). As each Δt corresponds to two back-azimuths, searching from $-\Delta t_{max}$ to Δt_{max} is effectively a search over the possible back-azimuths from 0 to 360.

The Δt with the most values in the bins closest to 90°, Δt_{90}, is the Δt that minimizes the additional phase due to the sensor separation. For a given Δt that is not the maximum or minimum, there are four possible back-azimuths. We eliminate two of the four by the sign of Δt. If Δt is negative, then there is an infrasonic first arrival and if Δt is positive, then there is a seismic first arrival. That is, if $-\Delta t$, then the infrasound data has to be shifted later in time relative to the seismic data, and vice versa. We then use Δt_{90} to calculate the apparent distance, d_0, (Fig. 2, Step 9). Next we compute θ, the angle between d and d_0: $\theta = \cos^{-1}\left({}^{d_0}/_{d}\right)$. The possible back-azimuths, α, are $\alpha = \beta \pm \theta$ and $\alpha = \beta \pm 180 \pm \theta$, where β is the azimuth from seismometer to microphone. For the example illustrated in Figure 2, steps 9 and 10, there is an infrasonic first arrival, so $\alpha = \beta \pm \theta$. If it was a seismic first arrival, then the back-azimuths would be $\alpha = \beta \pm 180 \pm \theta$. To find a unique back-azimuth solution, we use the particle motion on the seismometer (Fig. 2, Step 11). We employ the Coherency Matrix method [*Vidale*, 1986]

to automatically compute the particle motion azimuth through time and in our testing find that it performs better than the covariance method [*Montalbetti and Kanasewich*, 1970; *Wang and Kaveh*, 1985]. We use a window length of 4 s for the synthetic data and 10 s for MSH and Pagan. Next, we select the particle motion back-azimuth at the time of peak coherence, compare it to the Δt search results and select the back-azimuth search result closest to the particle motion solution. The search result that is closest to the particle motion solution is the unique back-azimuth to the source. To check the particle motion is elliptical, we integrate the three-component seismic data to get displacement and then plot one second of Z vs. E, Z vs. N, E vs. N, and Z vs. E vs. N (3D plot) starting at the time of peak coherence.

4.5 Data

We use three datasets to evaluate the efficacy of our method: a synthetic dataset generated using finite-differences with a 40 m resolution DEM of Mount Pagan Volcano, CNMI; recorded data from Mount St. Helens Volcano; and recorded data from Mount Pagan. Figure 3 shows the synthetic data used, which were generated by a coupled Earth-atmosphere 3D finite difference code [*Haney et al.*, 2009]. The source was a Ricker wavelet with center frequency of 1.4 Hz, which gives an effective bandwidth of 0.08 to 3.87 Hz. The source location is just below the vent of Mount Pagan as found in *Lyons et al.* [2016] and the seismometer is 3000 m to the southwest, where the actual station PGBF is located. The synthetic seismic wavefield is sampled at 40 m nodes in the vertical plane extending 160 m above and below the seismometer. The synthetic acoustic wavefield is sampled at the same vertical nodes in addition to horizontal nodes at 5, 10, 15 and 20 m to the south, such that there is a 2-D plane of nodes. We used the synthetic seismo-acoustic data from the node two intervals above the seismometer to avoid irregularities in coupling along the earth-atmosphere boundary [*Matoza et al.*, 2009].

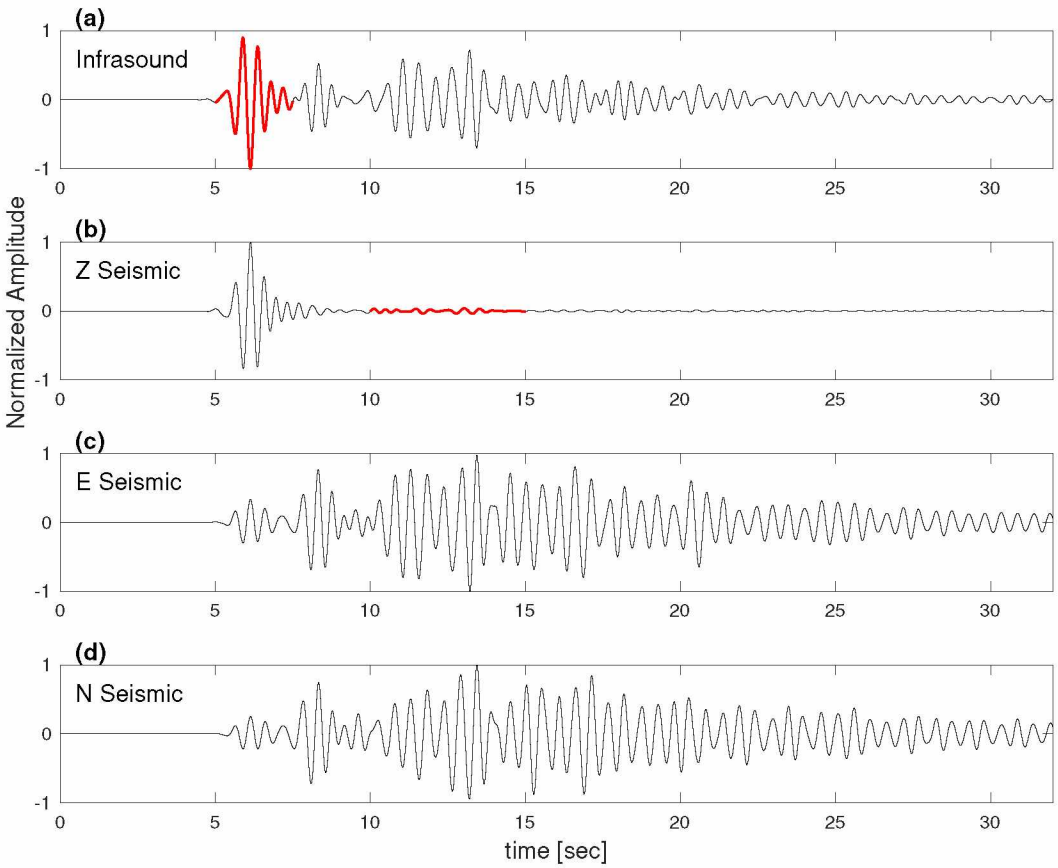

Figure 4.3 Synthetic, normalized, and unfiltered waveforms generated using a coupled Earth-atmosphere 3D finite-difference code: a) infrasound; b) vertical seismic; c) east seismic; d) north seismic. The explosion seismic wave reaches the seismometer at 4 s. This wave also generates an air-coupled ground-wave (ACG) (red portion in a). The airwave and GCA (red portion in b) arrives at ~10 s.

We use the seismo-acoustic data recorded at the Coldwater (CDWR) array from the 8 March 2005 phreatic explosion at Mount St. Helens Volcano [*Matoza et al.*, 2007]. CDWR had a 4-element, broadband (0.01-17 Hz) centered-triangular infrasound array of MB2000 aneroid microbarometers with an approximate aperture of 100 m. A Güralp CMG-40T broadband seismometer (0.033-50 Hz) was deployed a few meters from the central microbarometer. The seismo-acoustic data were sampled at 40 Hz. As in *Matoza and Fee* [2014], we use the second element of the infrasound array for GCA analysis, which is northeast of the seismometer by 14 m N and 51 m E. Only the vertical and radial seismic channels were recorded at CDWR. The peak seismic and acoustics amplitudes are ~2 μm/s and ~0.5-1 Pa, respectively, at 13.4 km.

For the Mount Pagan dataset, we use an explosion recorded on 26 July 2013 at the PGBF seismo-acoustic station installed by the U.S. Geological Survey in June 2013 [*Lyons et al.*,

2014]. PGBF has a 3-component, Güralp 6TD intermediate band (0.033-50 Hz) seismometer and a 6-element, collocated infrasound array of VDP-10 differential pressure transducers [*Thelen and Cooper*, 2015] with flat responses between 0.0125 and 25 Hz and a sensitivity of 10 mV/Pa. At the time of the explosion studied here, Pagan activity was dominated by continuous degassing from the summit vent that generated long-period seismic events and very-long-period infrasound events (10-50 per hour); explosions were infrequent [*Lyons et al.*, 2014; *Lyons et al.*, 2016]. The seismo-acoustic energy from the explosion is peaked between 0.25 and 5 Hz with signals lasting 20-30 seconds. Acoustic amplitudes are ~1-2 Pa at ~3 km with seismic amplitudes at ~6 μm/s.

4.6 Results

4.6.1 Synthetic dataset

We first apply our method to determine the back-azimuth to an infrasonic source using the synthetic data described in section 4. Figure 4 shows the (a) synthetic infrasound and seismic waveforms with the sensors separated by 15 m, (b) coherence spectrogram, (c) peak coherence, (d) raw phase spectrogram, and (e) time-shifted phase spectrogram. Note the high coherence values from 3.5 to ~7.5 seconds and ~10 to 15 seconds, which are also highlighted in the peak coherence through time (Fig. 4c). The initial high coherence is between the seismic explosion signal and the air-coupled ground wave; the second window is during the GCA. We added pink noise to the synthetics to eliminate high-coherence values prior to the explosion signal when the traces were both zero. Figure 4d shows the phase between the seismic and infrasonic traces and Figure 4e shows the phase between the seismic and time-shifted infrasound data, where the time-shift is defined as the one with the most phase values near 90°. Note the phase from Figure 4d to 4e shifts to a darker orange around ~8-14 s, closer to 90°. To avoid the high-coherence from ~3.5 to 7 s between the seismic explosion signal and the air-coupled ground wave, we applied our method to the data from 8 to 22 seconds (Fig. 5). Figure 5a shows the histograms for each time shift, where each horizontal row is a time shift, each column is a phase value, and the color scale represents the number of values in each bin. The dotted white line denotes 90° phase. Figure 5b shows the two back-azimuths in polar coordinates (rose diagram) associated with each time shift on the y-axis of Figure 5a. The length of each bar in the rose diagram indicates the total number of phase values in the bins close to 90° (i.e. 87° to 90° and 90° to 93°) (Fig. 5b). As the time-shifts each have two associated back-azimuths, the rose diagram in Figure 5b is symmetric about

the azimuth line, β. The two principal back-azimuths for the synthetic Pagan data are 49° and 311°. The coherence matrix method particle motion analysis finds a direction of 46.6° at the time of peak coherence, thereby suggesting 49° as the back-azimuth to source (via the phase shift in Fig. 5b). The actual back-azimuth to the synthetic Pagan source is 51.4° (Fig. 5c). To check the particle motion analysis and our assumption that the GCA has elliptical particle motion, we plot and analyze one second of 3D displacements (Fig. 6). The particle motion is elliptical and retrograde given the back-azimuth determined.

In addition to the 15 m sensor separation, we also tested the method at d = 5, 10 and 20 m. The search parameters and results are in Tables 1 and 2, respectively. For a GCA with energy between 0.2 and 2.2 Hz, the 15 m separation had a back-azimuth closest to the actual.

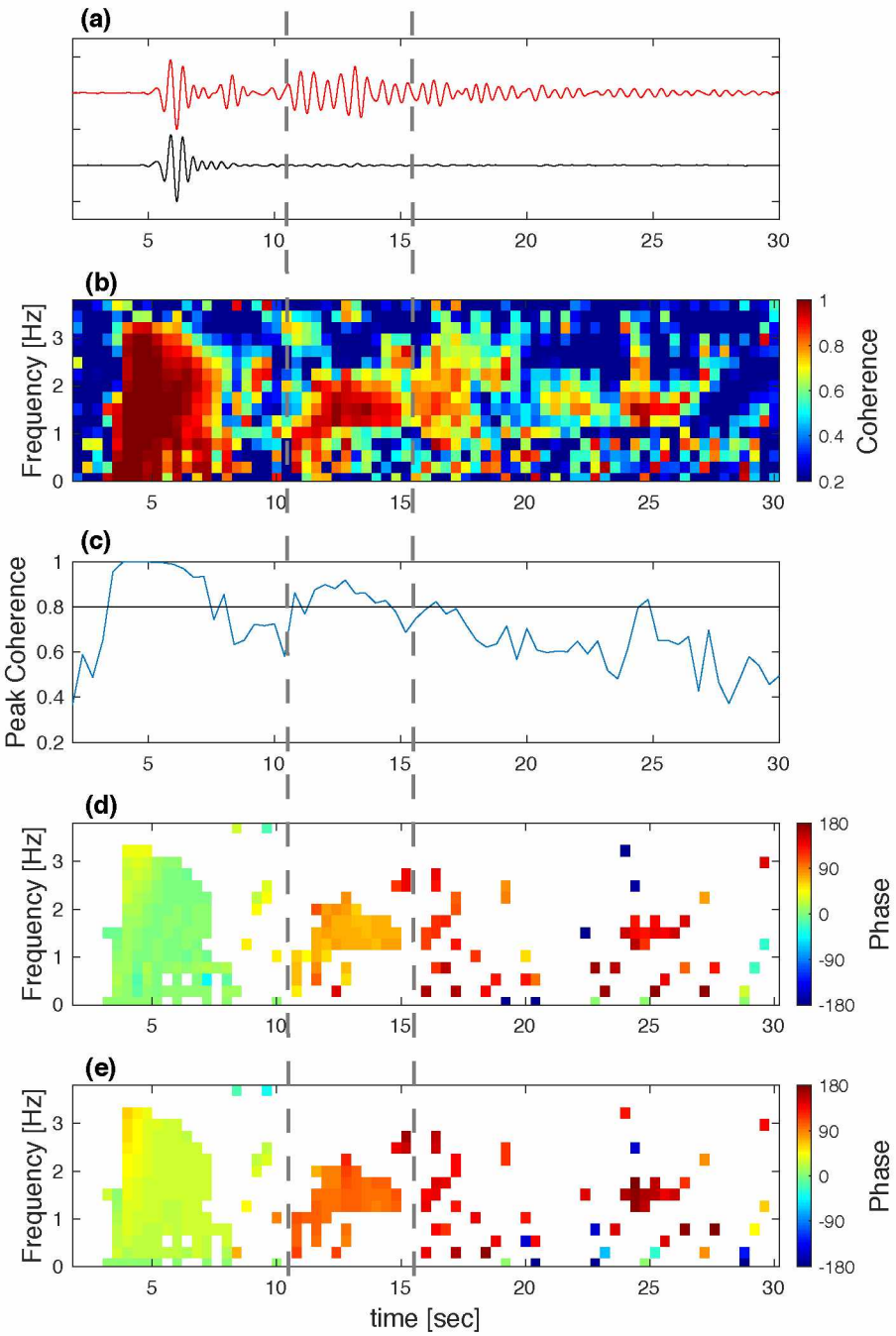

Figure 4.4 Pagan PGBF synthetic data with sensors separated by 15 m. a) Infrasound (red) and vertical seismic (black) traces filtered from 0.5 – 3.5 Hz. b) Coherence between synthetic infrasound and seismic data. c) Peak coherence through time; d) Phase between synthetic infrasound and seismic data from a); e) Phase found from time shifting the infrasound data until the majority of highly coherent data have a phase of 90°. For the coherence and phase calculations, we used a window length of 4 seconds with a 0.4 second step (90% overlap). The time between the vertical dashed lines highlights the airwave and GCA.

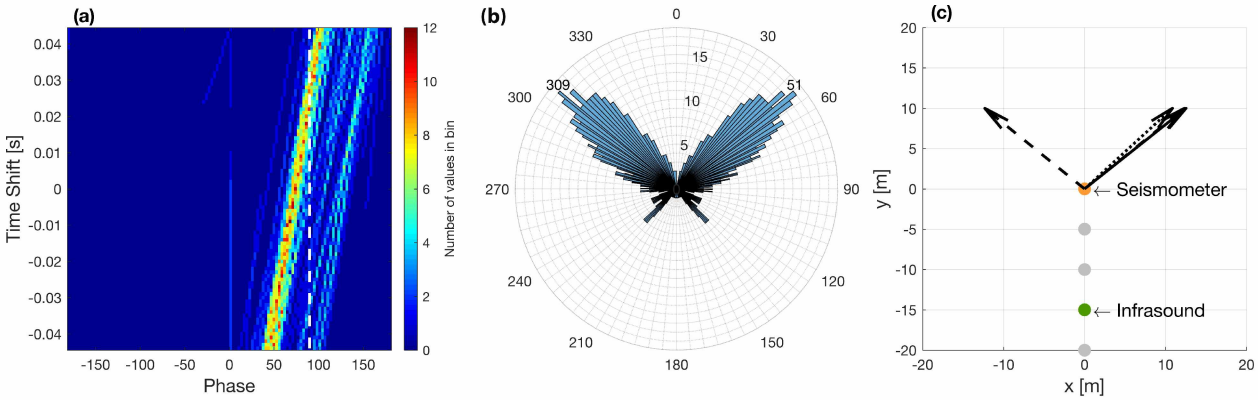

Figure 4.5 Synthetic phase search and rose diagram results. a) Image of histogram values from each time shift ($\boldsymbol{\Delta t}$) searched, with $\boldsymbol{\Delta t}$ plotted on the vertical and phase on the horizontal. The color scale indicates the number of phase spectrogram values in 3° bins from -180° to 180°. The vertical dotted white line highlights a phase of 90°. For each $\boldsymbol{\Delta t}$ there are two possible back-azimuths. b) Plots of the two possible back-azimuths and the number of phase values near 90° for each $\boldsymbol{\Delta t}$. The number of values near 90° includes the totals from bins 87° - 90° and 90° - 93°. c) Map view of the seismometer (orange) and infrasound microphone (green); the solid arrow shows the actual azimuth to the source while dashed and dotted lines show the back-azimuths from the phase search (also shown in b) and the back-azimuth from the particle motion analysis, respectively. Note the solid arrow hides the second dashed arrow pointing to the northeast. The gray circles show the other infrasound array element locations.

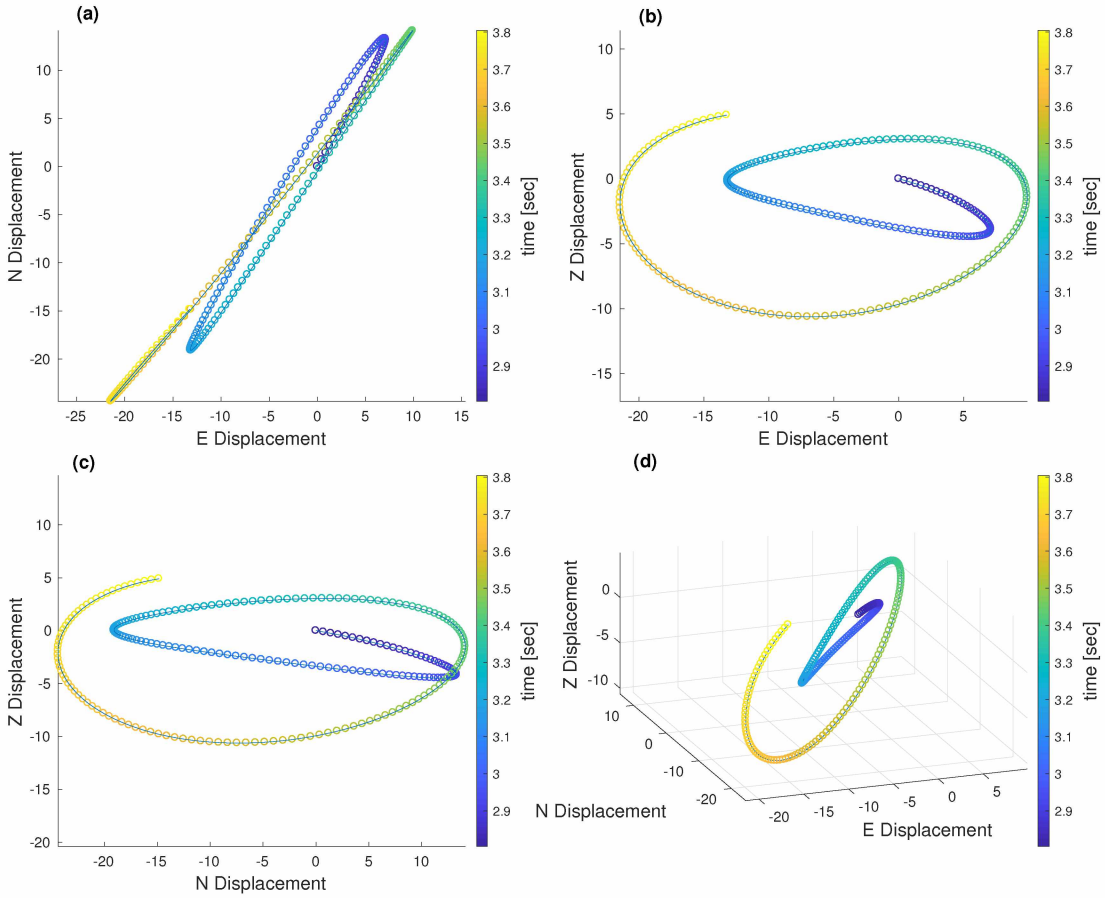

Figure 4.6 Particle motion for 1 second of a GCA recorded on the synthetic PGBF seismometer. Time is noted by the color of the circles. a) North versus East displacement; b) Vertical versus East displacement; c) Vertical versus North displacement; d) Vertical versus North versus East displacement.

4.6.2 Mount St. Helens

Next, we apply the method to a previously studied dataset: the MSH 8 March 2005 phreatic explosion. Figure 7 shows the same analysis as Figure 4 but for MSH. As shown in *Matoza and Fee* [2014], the seismic and infrasonic waveforms are more similar when filtered from 5 to 19 Hz (Fig.7a), and are coherent at higher frequencies (Fig. 7b). The peak coherence is above the 0.8 threshold from ~150 s to 2000 s (Fig. 7c). Figure 7d shows the original phase estimates flip between -180° and 180°, and 7e shows the phase after the time-shift found in the search is applied to the infrasound trace, which is close to 90°. Figure 8a shows a visual representation of the search results with phase from -180° to 180° across the x-axis and each time shift along the y-axis. The Δt with the most values near 90° is $\Delta t_{90} = 0.025$ in this example. We translate the time-shifts to back-azimuths (Fig. 8b), which indicates that there are two prominent back-azimuths at 155° and 354°. Unfortunately, this dataset only has the vertical and radial channels of seismic data, so we are unable to apply the particle motion analysis to find a unique solution. However, infrasound array processing results from *Matoza and Fee* [2014] found a back-azimuth of 153° and the actual back-azimuth is 154°, which is very close to one of our GCA BAD estimates. *Matoza and Fee* [2014] note a signal with high coherence prior to the MSH phreatic explosion that does not have 90° phase and PMCC finds it has a different back-azimuth. We applied our technique to that signal and one of our non-unique search results is within the back-azimuth range reported (labeled MSH-other in Tables 1 and 2).

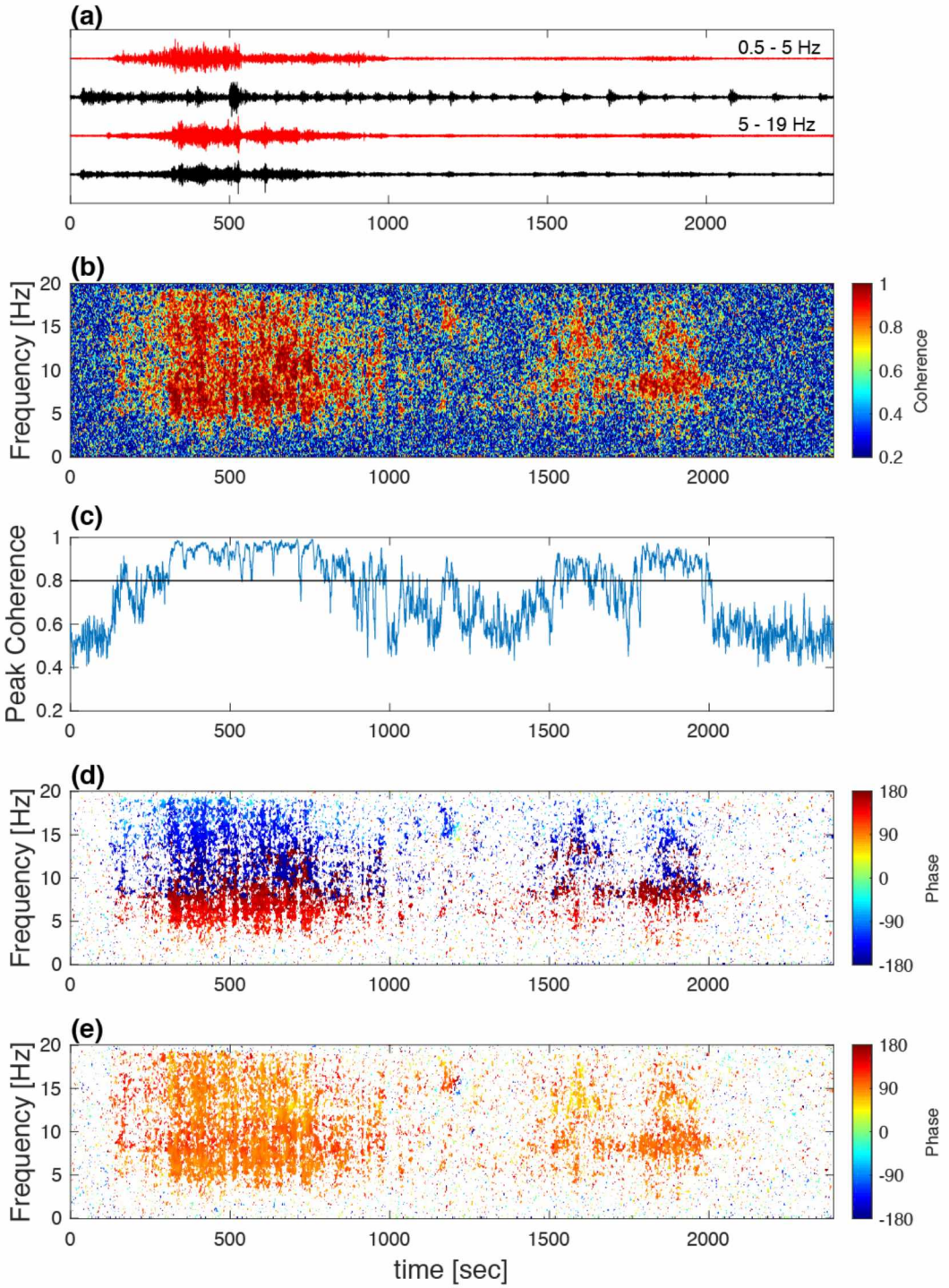

Figure 4.7 Mount St. Helens Coherence and Phase. a) Infrasound (red) and vertical seismic (black) traces filtered from 0.5 – 5 Hz (top) and 5 – 19 Hz (bottom); b) Coherence of infrasound and seismic data; c) Peak coherence through time; d) Phase between same infrasound and seismic data as in b; e) Phase found from time shifting the infrasound data until the majority of highly coherent data have a phase of 90°. For the coherence and phase calculations, we used a window length of 10 seconds with a 1 second step (90% overlap).

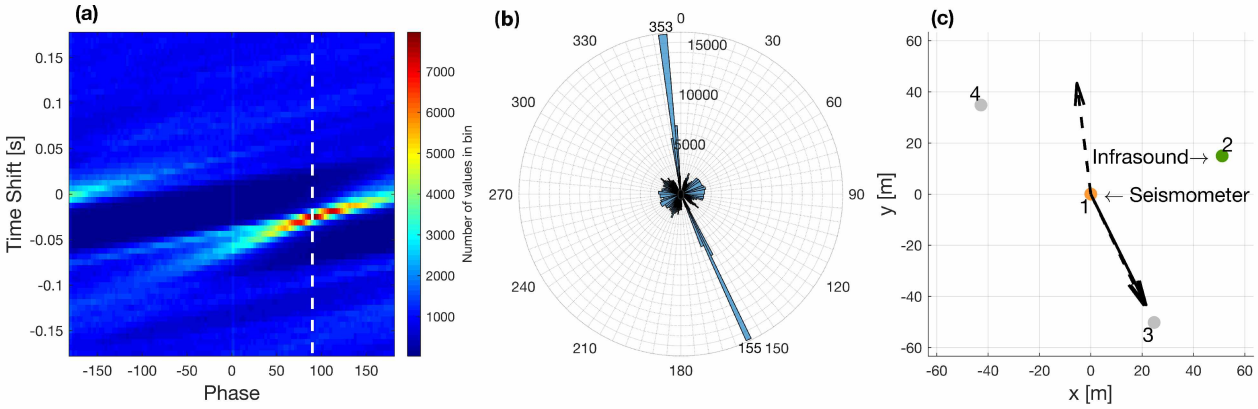

Figure 4.8 Mount St. Helens phase search and rose diagram result, similar to the synthetic example in Figure 5. a) Image of histogram values from each time shift. b) Rose diagram of the two possible back-azimuths and the number of phase values near 90° for each time shift. c) The arrangement of the seismometer (orange) and infrasound microphone (green); the solid arrow shows the actual azimuth to the source while dashed lines show the back-azimuths from the phase search (also shown in b). The gray circles show the other microphone locations. One of the two primary back-azimuths in b) agrees well with the actual back-azimuth in c).

4.6.3 Mount Pagan

Finally, we applied this technique to a recorded explosion from Pagan volcano with the six array elements deployed near the seismometer at PGBF. Here we examine data from the pairing of the seismometer and array element 2, noted as PGBF-2 in Tables 1 and 2. Figure 9a and b again highlight the similarity of the seismic and infrasonic traces when filtering out the lower frequencies where the traces are not coherent. The peak coherence is not as high as in the previous two cases, likely due to interference from the seismic explosion signal, but is still above 0.8 for a ~5 s consecutively starting at 50 s (Fig. 9c). Here again the time-shift found in the search highlights the 90° phase, but for a narrower frequency band from ~13-18 Hz (Fig. 9e). Figure 10a shows that the Pagan example has much fewer phase values than for the MSH example mostly due to the significantly short signal duration, ~30 s compared to ~1850s. Even given the lower number of values in the bins, the search finds a robust $\Delta t_{90} = 0.005\ s$ and corresponding dominant back-azimuths of 50° and 232° (Fig. 10b). The particle motion analysis determines an azimuth of 50°, thus suggesting 50° as the unique solution. Figure 10c shows the seismometer and infrasonic microphone arrangement and the solid arrow indicates the actual back-azimuth to the source, 50.6°. Figure 11 shows one second of particle motion starting at 51 s, the time of maximum peak coherence. The particle motion is clearly elliptical, particularly in Z vs E and N vs E (Fig. 11b,d).

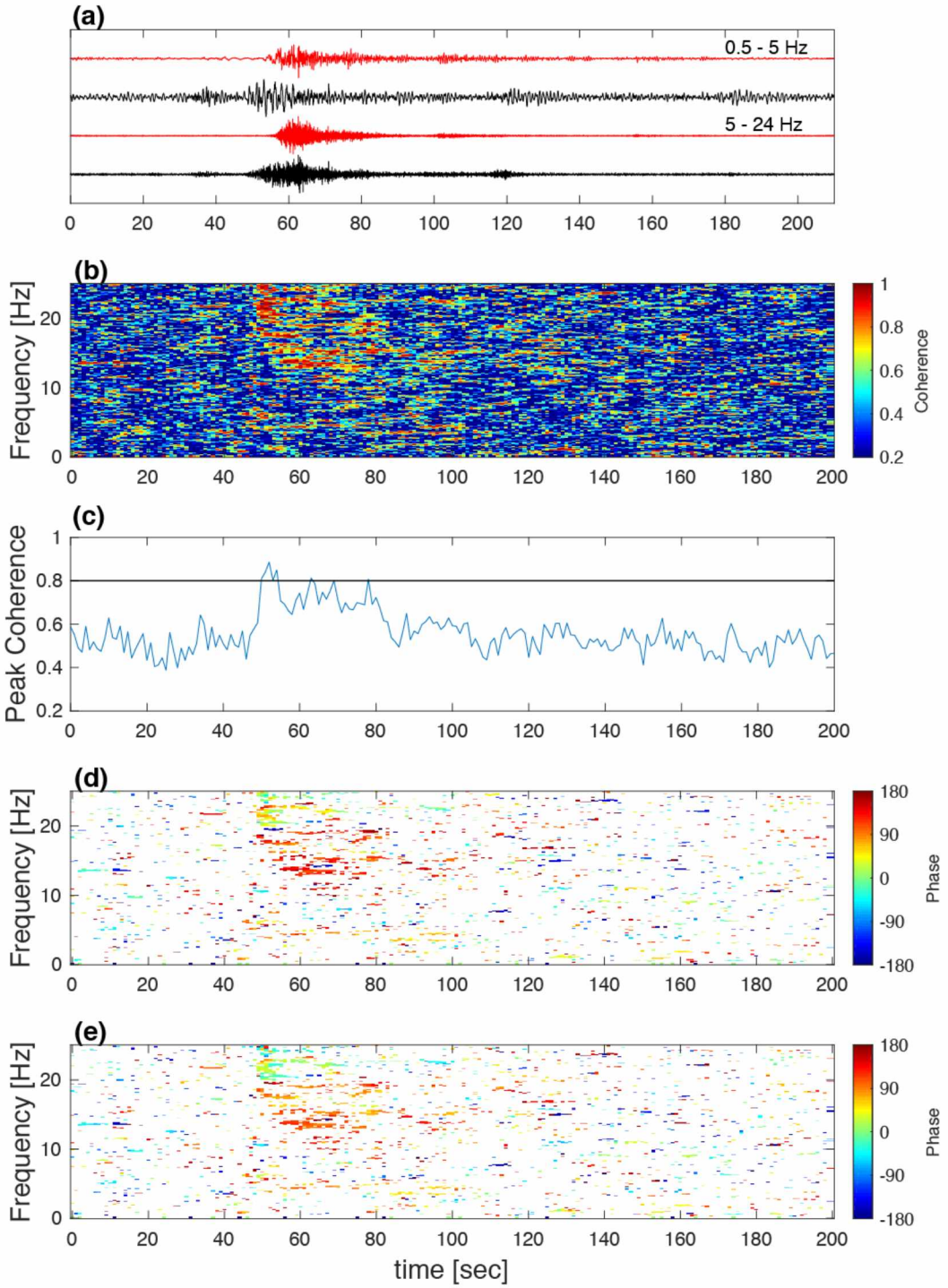

Figure 4.9 Pagan PGBF Coherence and Phase a) Infrasound (red) and vertical seismic (black) traces filtered from 0.5 – 5 Hz (top) and 5 – 24. Hz (bottom); b) Coherence of infrasound and seismic data. c) Peak coherence through time; d) Phase between same high-pass filtered infrasound and seismic data as in b; e) Phase found from time shifting the infrasound data until the majority of highly coherent data have a phase of 90°. For the coherence and phase calculations, we used a window length of 10 seconds with a 1 second step (90% overlap).

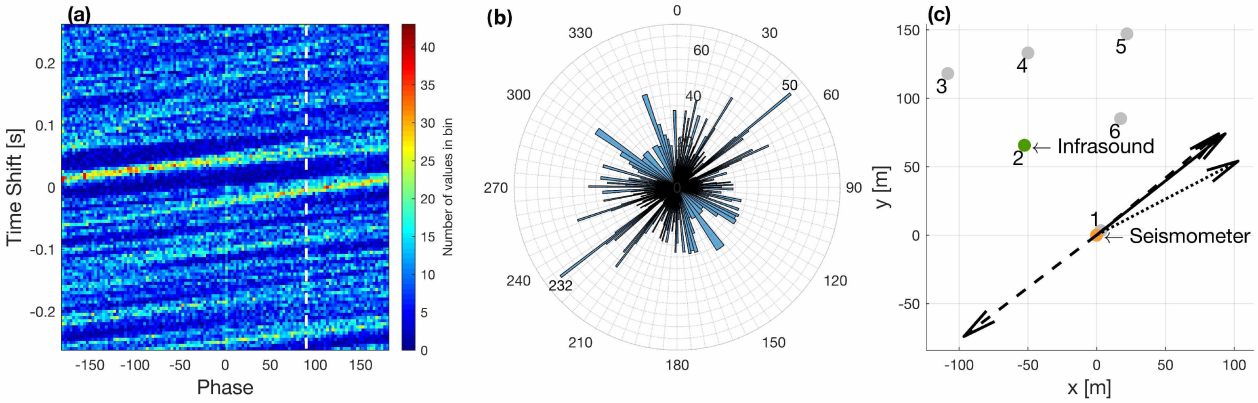

Figure 4.10 Pagan PGBF search and rose diagram result, similar to Figures 5 and 8. a) Image of histogram values from each time shift. b) Rose diagram of the two possible back-azimuths and the number of phase values near 90° for each time shift. c) The arrangement of the seismometer (orange) and infrasound microphone (green); the solid arrow shows the actual azimuth to the source while dashed and dotted lines show the back-azimuths from the phase search (also shown in b) and the back-azimuth from the particle motion analysis, respectively. The gray circles show the other infrasound array element locations. Note one of the two back-azimuth results in b) is consistent with the actual back-azimuth in c).

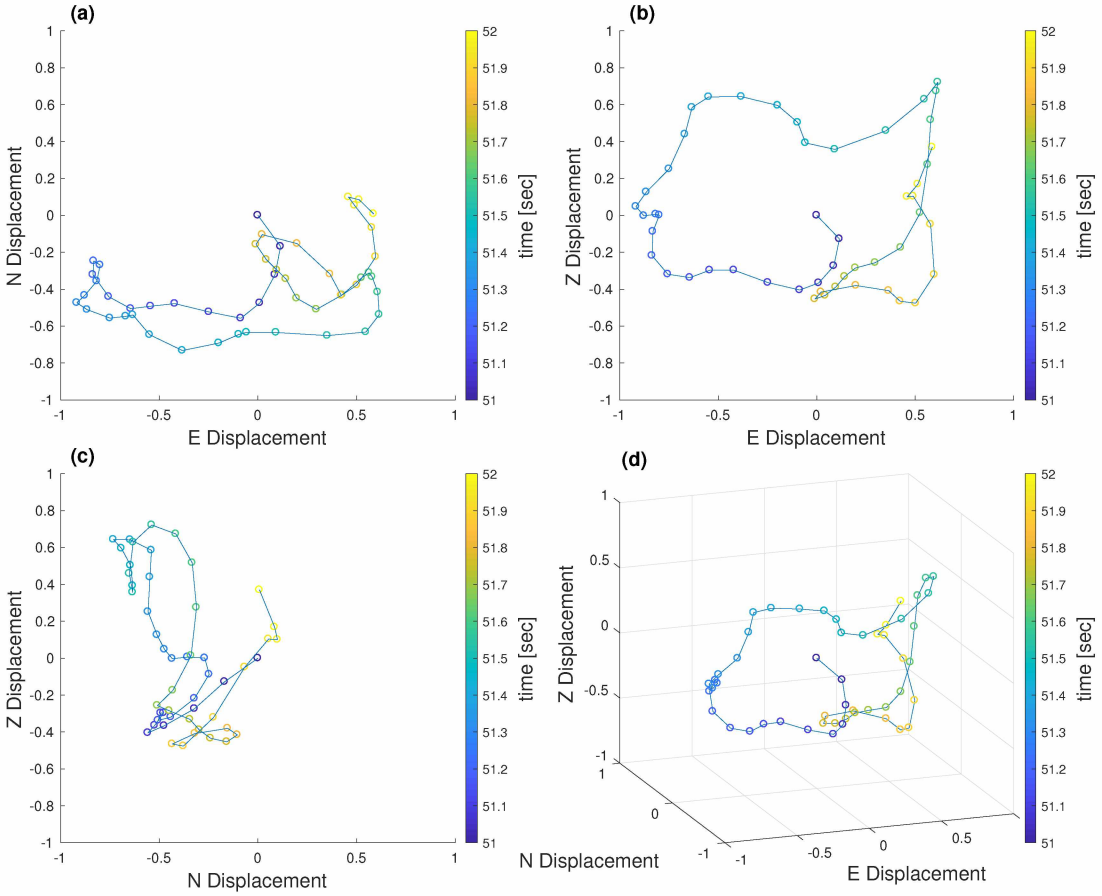

Figure 4.11 Particle motion for 1 second of a GCA recorded on PGBF seismometer. Time is noted by the color of the circles. a) North versus East displacement; b) Vertical versus East displacement; c) Vertical versus North displacement; d) Vertical versus North versus East displacement.

We further apply our method to each array element at the PGBF site. Array element 1, PGBF-1, ~4.6 m from the seismometer, had a very coarse result, in that from one time step to the next was about a 30° change in azimuth, and was ~34° off from the actual back-azimuth. The pairing with array element 6 (PGBF-6), about the same distance from the seismometer as element 2, gives a back-azimuth of 56°. The infrasonic array deployed with PGBF has three additional elements ~160 m from the seismometer. We tried our method with each of those elements, but they failed to find a robust back-azimuth as the peak coherence was below the 0.8 threshold. Infrasound array processing of this event using a least-squares technique yields a back-azimuth of ~51°. Table 1 summarizes the sensor arrangement and search parameters; Table 2 summarizes the results of the method. Bold text indicates the examples for which figures are included (see Table 2).

Table 4.1. Sensor arrangement and back-azimuth search parameters

Source	**d [m]**	**β**	**sps [Hz]**	**dt [s]**	**ts max [s]**	**ts step [s]**	**window [s]**	**c [m/s]**
Synthetic	5	180°	250	0.004	0.016	0.001	4	350
Synthetic	10	180°	250	0.004	0.032	0.001	4	350
Synthetic	15	180°	250	0.004	0.044	0.001	4	350
Synthetic	20	180°	250	0.004	0.06	0.001	4	350
MSH	52.9	74.6°	40	0.025	0.175	0.0063	10	343
MSH-other	52.9	74.6°	40	0.025	0.175	0.0063	10	343
PGBF-1	4.6	44.1°	50	0.02	0.02	0.005	10	343
PGBF-2	84.0	321.3°	50	0.02	0.26	0.005	10	343
PGBF-6	86.9	11.6°	50	0.02	0.26	0.005	10	343

Table 4.2. Back-azimuth determination results for the selected datasets. Search A and B are the two possible back-azimuths determined from the phase search. Particle motion is the back-azimuth determined from the coherency matrix method used to pick a unique back-azimuth. Result is the final back-azimuth determined from our GCA BAD method. Array processing is the back-azimuth determined from independent array processing. Actual is the back-azimuth calculated given the seismometer and source locations. Difference is the difference between the actual back-azimuth and the result from the GCA BAD method. Examples in bold text have figures included.

					Back-azimuth						
Source	d [m]	d_0 [m]	freq. [Hz]	duration [s]	Search A	Search B	Particle Motion	Result	Array Processing	Actual	Difference
Synthetic[b]	5	2.8	0.2 - 2.2	5	55.9°	304.1°	46.6°	55.9°	-	51.4°	-4.5°
Synthetic[b]	10	9.1	0.2 - 2.2	5	24.5°	335.5°	46.8°	24.5°	-	51.4°	26.9°
Synthetic	**15**	**9.8**	**0.2 - 2.2**	**5**	**49.2°**	**310.8°**	**46.6°**	**49.2°**	**-**	**51.4°**	**2.2°**
Synthetic	20	8.75	0.2 - 2.7	5	60.7°	299.3°	46.3°	60.7°	-	51.4°	-9.3°
MSH	**52.9**	**8.6**	**5 - 19**	**1850**	**155°**	**354°**	**-**	**155°**	**153°[a]**	**154°**	**-1°**
MSH-other	52.9	19.3	4 - 19	30	323.3°	186.0°	-	186.0°	185°-190°[a]	-	-
PGBF-1	4.6	3.4	13 - 24	30	85.9°	2.4°	64.5°	85.9°	51°	50.6°	-35.3°
PGBF-2	**84.0**	**1.7**	**13 - 24**	**30**	**50°**	**232°**	**50°**	**50°**	**51°**	**50.6°**	**0.6°**
PGBF-6	86.9	61.7	13 - 24	30	56.3°	327.0°	62.3°	56.3°	51°	50.6°	-5.7°

[a]From *Matoza and Fee [2014]*

[b]Lots of scatter

4.7 Discussion

In general, we find our GCA back-azimuth determination method works well for the examples chosen, especially given the variation in coherence across the examples, from near perfect (noise-added synthetic) to marginal (Pagan). For the successful cases, the actual and resulting back-azimuths differ by <1° to 5°. Our GCA BAD method also provides a better result than the particle motion analysis alone. Particle motion analysis has been shown to be a rough estimator for back-azimuth [*Montalbetti and Kanasewich*, 1970; *Vidale*, 1986] and applied here it works well as a tool to distinguish between the non-unique search results. For three of the four cases where the back-azimuth is not found (synthetic 5 and 10 m and PGBF-1), we attribute this failure to the sensor spacing being too small for the respective sample rate. Below we discuss the limitations and application of the GCA BAD method and suggest future work.

4.7.1 Practicalities of Application

4.7.1.1 Sensor spacing

Sufficient spacing between the seismic and infrasound sensor is key to the success of our method. A particular motivation for this investigation was to utilize the rich EarthScope TA dataset, since later phases of the deployment included infrasound instrumentation collocated with

seismic and other equipment [*de Groot-Hedlin and Hedlin*, 2014; *Walker et al.*, 2010]. Through the development of our method, we found that the sensors need to be separated by at least the equivalent distance a sound wave travels between recorded samples (dt, or $1\ /\ (sample\ rate)$); in other words d needs to be at least $dt \times c$. Otherwise the phase delay above 90° is unresolvable. For a sample rate of 40 Hz, which is common at TA deployments, dt is 0.025 s and at a speed of sound of 340 m/s the sensors would need to be separated by at least ~8.5 meters. Unfortunately, TA sensors are not sufficiently separated as the TA station summary pages list the same location for the seismometer and infrasonic microphone. In reality, the TA station sensors are separated slightly, for example one station is described to have a 2 m separation between the seismometer and the infrasound intake, which is at the end of a 3.6 m long hose (R. Busby, personal communication, Nov 2013). This corresponds to a total separation distance of 5.6 m, which is unfortunately 3 m shy of the needed minimum. Since our method relies on time shifting the data, if the sensors are deployed at less than a dt equivalent distance then all the time shifts will be sub sample rate. With sub-dt equivalent sensor spacing an accurate back-azimuth is not feasible, but an evaluation of the seismo-acoustic coherence is still a valuable tool as it can be used to distinguish GCAs and acoustic waves in the seismic record [*Fee et al.*, 2017; *Matoza and Fee*, 2014]. We recommend a sensor spacing of at least a dt equivalent, if not several, and as high a sample rate as is feasible.

To further illustrate this recommendation, we explore the relationship between the sample rate and the sensor spacing. The delay time, T, for a plane wave crossing two sensors is $T = (d \cdot \cos\theta)/c$, where d is the interstation spacing and c is the speed of sound. θ is the difference between the back-azimuth of the plane wave, α, and the azimuth from seismometer to microphone, β, such that $\theta = \alpha - \beta$, (shown in Fig. 1, steps 3 and 4). It then follows that, to have the sensors separated by at least a dt-equivalent distance, T/dt must be > 1. Following this relationship, $(d \cdot \cos\theta)/(c \cdot dt) > 1$. This inequality will never hold when the plane wave is exactly broadside to the two sensors, since in that case $\cos\theta = 0$. At the very least, dt should be chosen such that $d/(c \cdot dt) > 1$ such that the inequality is satisfied for some angles. In this situation, there will be an angular zone where the criterion is not met. This angular zone is bound by the critical angle, θ_c, defined as $\theta_c = \cos^{-1}\big((c \cdot dt)/d\big)$. This angular zone relative to a given sensor geometry is $\beta \pm \theta_c$. Figure 12a illustrates these relationships and sensor spacing

limitations with d plotted along the x-axis and sample rate (or $1/dt$) along the y-axis. The colors indicate the angle θ_c for a given sensor separation and sample rate. The white area towards the lower left is where the criterion fails and the boundary where it changes to white should be viewed as the absolute minimum spacing and sample rate necessary for our technique. Figure 12b shows how the critical angle relates to the seismo-acoustic sensor geometry. Note with increasing sensor separation and sample rate the critical angle increases, thus decreasing the angular zone highlighted by the red arrows in Figure 12b. The circles plotted in Figure 12a show the sensor spacing versus sample rate for the three different datasets evaluated. PGBF-1 falls in the area where the criterion fails, but the PGBF-2, -6 and MSH sensor geometries and sample rates are more ideal, which is reflected in their accurate back-azimuth results.

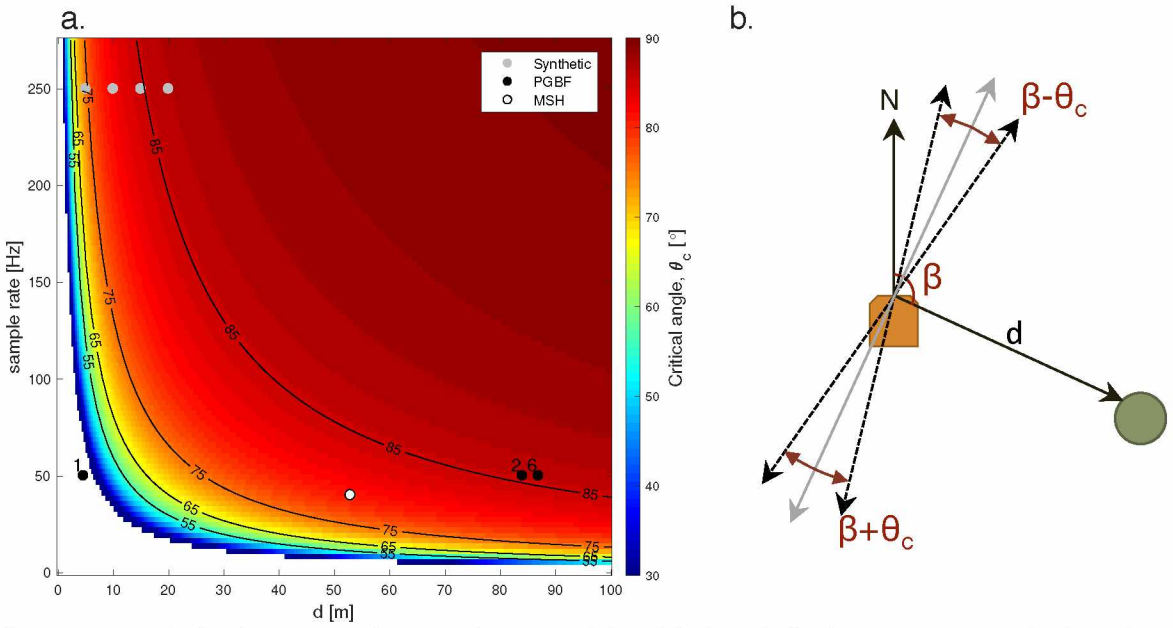

Figure 4.12 Analysis of sensor spacing, sample rate, and the critical angle for the GCA BAD method. a) The white area of the figure is where the sample rate and sensor spacing are too small and the GCA method fails. The color scale indicates how the critical angle changes with sensor geometry and sample rate. As sensor spacing and sample rate increase the resolvable back-azimuth resolution improves. The gray, black and white dots show the sensor spacing and sample rates for the synthetic, PGBF and MSH, respectively, cases evaluated. b) Shows the angular zone where the criteria are not met relative to seismometer (orange square) and infrasonic microphone (green circle) geometry. The dashed lines are $\beta \pm \theta_c$ and $\beta + 180° \pm \theta_c$ and the solid gray line is $\beta \pm 90°$. Between the two dashed lines is the angular zone where the criterion fails defined by the critical angle and highlighted by the red arrows extending out from the gray line.

Increased sensor spacing will also decrease the coherence and potentially the effectiveness of the method. In applying the GCA BAD method with each array element at PGBF, the lower coherence at the further array elements, $d = \sim 160$ m, limited the accuracy of the back-azimuth

estimate. This suggests an upper bound on sensor spacing due to loss of coherence. Investigations on coherence loss across infrasonic array elements have found that a decrease in signal-to-noise (SNR) ratio has a more significant impact on coherence loss than sensor spacing [*Christie and Campus*, 2009; *Green*, 2015]. For frequencies of 0.1 – 1 Hz, coherence remains high within 0.5 km sensor spacing and coherence loss is higher parallel to the wavefront than perpendicular to it [*Christie and Campus*, 2009; *Green*, 2015]. As GCA are usually observed at frequencies an order of magnitude higher than these studies, 1 – 20+ Hz, the spatial coherence range is likely less than observed by *Green* [2015]. Our observations at Pagan also show a significant loss of coherence from sensors separated by ~85 m to ~160 m, where there were no peak coherence values above the threshold of 0.8. The sensor spacing of ~85 m is about an order of magnitude lower than the 0.5 km spacing found in [*Green*, 2015]. We suggest a maximum sensor spacing of ~100 m, but ~50 m is likely better to maintain high coherence for waves arriving from a variety of back-azimuths. Further investigation into spatial coherence loss at higher frequencies is needed to improve this recommendation.

4.7.1.2 Measuring sensor locations

Highly accurate sensor locations are also key to the success of our method. For the MSH case, we had handheld and differential GPS coordinates and the x-y distances reported in *Matoza and Fee* [2014] from the seismometer to the infrasonic microphone. The differential GPS used had an accuracy of 50 cm [*Matoza et al.*, 2007], where handheld GPS's typically have 1-5 m precision in open areas with an unobstructed view of satellites [*Johnson and Barton*, 2004]. When we used the handheld GPS coordinates we determined a back-azimuth of ~158°; we improved our result by ~3° when we used the reported x-y distances. Using the differential GPS coordinates improved our result by an additional degree, ~154°. This confirms that when deploying instruments, it is important to obtain highly accurate GPS coordinates, and if those are not available to measure the x-y distance from seismometer to microphone.

4.7.1.3 Source distance and altitude

In the application of the GCA BAD method we assume an incidence angle near 90° from vertical, as our sound waves arrive from local (<~15 km) distances [*Ben-Menahem and Singh*, 2000; *Fee and Matoza*, 2013]. *Edwards et al.* [2007] observed the airwave and GCA across a

seismo-acoustic array from the shockwave resulting from atmospheric re-entry of the Stardust sample return capsule. They documented retrograde particle motion and a coherent GCA, suggesting our method could be applied to an infrasonic source at any altitude. Applying this GCA method to global infrasound monitoring efforts would be advantageous as the current network of arrays deployed is sparse. For the examples we investigated, the sources are at local distances such that the arrivals are likely direct and near 90° from vertical. When an infrasound wave arrives at the Earth's surface after being refracted near the tropopause, stratopause or mesopause it can have a lower incidence angle than near 90° [*Fee and Matoza*, 2013]. When this refracted wave travels across an infrasound array it will have a higher apparent (trace) velocity than the speed of sound due to the non-horizontal angle of incidence. Common trace velocities and incidence angles relative to vertical for the different arrivals are: 343 m/s and ~90°, for tropospheric, 330-350 m/s and <79° for stratospheric, and 400 m/s and 60° at 343 m/s for thermospheric [*Fee et al.*, 2013; *Matoza et al.*, 2011]. These incidence angles suggest the GCA BAD method would work for long-range infrasound, especially those ducted in the troposphere and stratosphere. Further investigation is needed to determine the effect of incidence angle on the GCA BAD method presented here.

Timing between the seismic and infrasonic arrivals is also key in determining the GCA back-azimuth. In comparing the Pagan and MSH examples we note that while the GCA method successfully determined back-azimuths for both, the Pagan data have lower coherence, hovering just over and under our threshold. This may be due to the presence of pure seismic phases even at higher frequencies. The PGBF array is ~3 km from the source. If the explosion wave travels at 5 km/s through the ground and 340 m/s through the atmosphere, the airwave will arrive ~8.2 s after the seismic wave. Since the explosion signal is ~30 s in duration, the seismic explosion signal and the GCA will overlap, thus lowering the coherence during the GCA. This suggests that deploying seismo-acoustic sensor pairs further from potential sources may enhance the GCA BAD method's effectiveness, but further investigation is needed.

4.7.1.4 Seismometer characteristics and deployment depth

The examples presented in this manuscript employed 3-component broadband seismometers, buried near the surface, as opposed to short period or borehole seismometers. Recent work has

shown a borehole seismometer recorded GCA signals from Sakurajima Volcano, Japan [*Ichihara*, 2016]. However, *Ichihara* [2016] reports that the borehole data and surface infrasound data did not correlate well. This suggests that our method may not work with seismometers buried at borehole depths, but further investigation is needed. While the seismic dataset we used was broadband, data from short-period seismometers should also work. The examples of GCAs in this manuscript and in *Matoza and Fee* [2014] are higher in frequency, above 5 Hz. There are, however, examples of energy at lower frequencies, such as the recent Pavlof Volcano eruption where there was coherence from ~0.8 to 8 Hz [*Fee et al.*, 2017]. In general, the frequency characteristics of GCAs reflect those of the incident airwave [*Edwards et al.*, 2008; *Edwards et al.*, 2007]. Much of the GCA energy in the Pavlof eruption would likely have been recorded on a short-period (~ 1 s) seismometer as well. The key characteristic of the seismometer is that it be 3-component to utilize the particle motion to resolve a unique back-azimuth.

4.7.2 Future directions and recommendations

The GCA back-azimuth determination method presented here could be applied to any seismo-acoustic pair, assuming the critical angle criteria (Section 5) have been met. Two suggested future research directions for this method that have yet to be explored in detail are: application to long-range infrasound and explosion source location. Our method determines the back-azimuth to a local infrasonic source. A desired next step is to resolve a source location. If nearly collocated seismo-acoustic sensor pairs were strategically deployed across a region, the GCA method could be applied at each pair and the back-azimuth used to triangulate a source location. Many seismic deployments include an infrasound sensor with each seismometer. Data from such deployments would be ideal for evaluating if the GCA BAD method works on a global scale. The GCA method could also be used to monitor volcanic activity on a regional scale. If seismo-acoustic sensor pairs were deployed throughout a volcanic region, as they increasingly are, with sensors spaced at several dt-equivalent lengths, coherence could be used to detect GCAs, indicating an acoustic source. The GCA method would then determine the back-azimuth, which could be linked to a known volcanic source. With a full seismo-acoustic network, triangulation could be used to determine which volcano is active at a given moment.

A logical dataset to apply this method to is the EarthScope TA; unfortunately, the seismic sensor and infrasound sensor at each site appear too close together. For TA deployments that have become permanent state or federal stations or any other seismo-acoustic deployments, it would be advantageous to move the infrasound microphone away from the seismometer by ~50 m and increase the sampling rate. Accurate reporting of relative station locations would also be important. These stations could then be used to detect and determine back-azimuths to myriad acoustic sources. *Edwards et al.* [2007] examined the local soil properties to estimate the local seismic velocity and energy coupling efficiency. A variety of deployments across a large region, such as the United States, with documentation of local geology and soil characteristics would allow for further investigation into factors that influence acoustic energy coupling to the ground. For seismic studies this could improve seismometer site selection in order to avoid geologic settings where acoustic energy more easily couples into the ground.

4.8 Conclusion

In this manuscript we present a method to robustly determine the back-azimuth to an infrasonic source using only one infrasonic microphone and one nearly collocated 3-component seismometer. The method exploits the phase difference between the infrasonic wave and GCA, along with the GCA particle motion, to determine a unique back-azimuth to the source. We observe high coherence between airwaves and GCAs from synthetic and volcanic sources. We test the technique using a synthetic dataset and apply it with success to two volcanic datasets with variable SNR and orders of magnitude difference in signal duration. Our GCA BAD method finds back-azimuths that are within <1° to 5° of the actual and the array processing determined back-azimuths. Key elements to successfully using this method are: 1) separating the seismometer and infrasonic microphone by several dt-equivalent lengths (the distance traveled by an acoustic wave during one digitized sample), but less than 100 m; 2) acquiring data at a high sample rate (e.g. >100 Hz); and 3) using a 3-component seismometer. Sensors separated by less than a dt-equivalent distance could still be used to detect acoustic sources, but a back-azimuth will not be successfully determined. This GCA BAD technique could be used to detect and help locate explosive acoustic sources, such as those from volcanoes and anthropogenic explosions. Future work should explore the optimal sensor separation distances and application to long-range acoustics sources.

4.9 Acknowledgements

We extend thanks to the Geophysical Institute of the University of Alaska Fairbanks, NSF EAR-1331084 and EAR-1614855 for support of this work. Mike West, Carl Tape, and Curt Szuberla provided helpful comments on the method and results. The MSH data are available upon request from Natural Resources Canada [http://www.nrcan.gc.ca/home]. The Mt. Pagan data are available by request through the USGS.

4.10 References

Aki, K., and P. G. Richards (2002), Plane Waves in Homogeneous Media and Their Reflection and Transmission at a Plane Boundary, in *Quantitative Seismology*, edited by J. Ellis, pp. 155-156, University Science Books, Sausalito, CA,

Ben-Menahem, A., and S. J. Singh (2000), *Seismic Waves and Sources*, 2nd ed., Springer, New York, http://dx.doi.org/10.1007/978-1-4612-5856-8

Cansi, Y. (1995), An automatic seismic event processing for detection and location: The P.M.C.C. Method, *Geophysical Research Letters*, *22*(9), 1021-1024, http://dx.doi.org/10.1029/95GL00468

Cansi, Y., and Y. Klinger (1997), An automated data processing method for mini-arrays, *Newsletter of the European-Mediterranean Seismological Center*, *11*, 2-4,

Christie, D. R., and P. Campus (2009), The IMS Infrasound Network: Design and Establishment of Infrasound Stations, in *Infrasound Monitoring for Atmospheric Studies*, edited, pp. 29-75, Springer Netherlands, http://dx.doi.org/10.1007/978-1-4020-9508-5_2

De Angelis, S., D. Fee, M. Haney, and D. Schneider (2012), Detecting hidden volcanic explosions from Mt. Cleveland Volcano, Alaska with infrasound and ground-coupled airwaves, *Geophysical Research Letters*, *39*(L21312), http://dx.doi.org/10.1029/2012gl053635

de Groot-Hedlin, C. D., and M. A. H. Hedlin (2014), Infrasound detection of the Chelyabinsk meteor at the USArray, *Earth and Planetary Science Letters*, *402*(C), 337-345, http://dx.doi.org/10.1016/j.epsl.2014.01.031

Edwards, W. N., D. W. Eaton, and P. G. Brown (2008), Seismic observations of meteors: Coupling theory and observations, *Rev. Geophys.*, *46*(4), 232-221, http://dx.doi.org/10.1029/2007RG000253

Edwards, W. N., D. W. Eaton, P. J. McCausland, D. O. ReVelle, and P. G. Brown (2007), Calibrating infrasonic to seismic coupling using the Stardust sample return capsule shockwave: Implications for seismic observations of meteors, *Journal of Geophysical Research: Solid Earth (1978–2012)*, *112*(B10306), 1-13, http://dx.doi.org/10.1029/2006JB004621

Fee, D., M. M. Haney, R. Matoza, C. A. L. Szuberla, J. Lyons, and C. Waythomas (2016), Seismic Envelope - Based Detection and Location of Ground - Coupled Airwaves from Volcanoes in Alaska, *Bulletin of the Seismological Society of America*, *106*(3), 1024-1035, http://dx.doi.org/10.1785/0120150244

Fee, D., M. M. Haney, R. S. Matoza, A. R. Van Eaton, P. Cervelli, D. J. Schneider, and A. M. Iezzi (2017), Volcanic tremor and plume height hysteresis from Pavlof Volcano, Alaska, *Science*, *355*(6320), 45-48, http://dx.doi.org/10.1126/science.aah6108

Fee, D., and R. S. Matoza (2013), An overview of volcano infrasound: From hawaiian to plinian, local to global, *Journal of Volcanology and Geothermal Research*, *249*, 123-139, http://dx.doi.org/10.1016/j.jvolgeores.2012.09.002

Fee, D., S. R. McNutt, T. M. Lopez, K. M. Arnoult, C. A. L. Szuberla, and J. V. Olson (2013), Combining local and remote infrasound recordings from the 2009 Redoubt Volcano eruption, *Journal of Volcanology and Geothermal Research*, *259*(C), 100-114, http://dx.doi.org/10.1016/j.jvolgeores.2011.09.012

Green, D. N. (2015), The spatial coherence structure of infrasonic waves: analysis of data from International Monitoring System arrays, *Geophysical Journal International*, *201*(1), 377-389, http://dx.doi.org/10.1093/gji/ggu495

Haney, M. M., K. van Wijk, L. A. Preston, and D. F. Aldridge (2009), Observation and modeling of source effects in coda wave interferometry at Pavlof volcano, *The Leading Edge*, *28*(5), 554-560, http://dx.doi.org/10.1190/1.3124930

Ichihara, M. (2016), Seismic and infrasonic eruption tremors and their relation to magma discharge rate: A case study for sub-Plinian events in the 2011 eruption of Shinmoe-dake, Japan, *J. Geophys. Res. Solid Earth*, *121*(10), 7101-7118, http://dx.doi.org/10.1002/2016JB013246

Ichihara, M., M. Takeo, A. Yokoo, J. Oikawa, and T. Ohminato (2012), Monitoring volcanic activity using correlation patterns between infrasound and ground motion, *Geophysical Research Letters*, *39*(L04304), 1-5, http://dx.doi.org/10.1029/2011gl050542

Johnson, C. E., and C. C. Barton (2004), Where in the World Are My Field Plots? Using GPS Effectively in Environmental Field Studies, *Frontiers in Ecology and the Environment*, *2*(9), 475-482, http://dx.doi.org/10.2307/3868336

Johnson, J. B., and S. D. Malone (2007), Ground-coupled acoustic airwaves from Mount St. Helens provide constraints on the May 18, 1980 eruption, *Earth and Planetary Science Letters*, http://dx.doi.org/10.1016/j.epsl.2007.03.001

Langston, C. A. (2004), Seismic ground motions from a bolide shock wave, *Journal of Geophysical Research*, *109*(B12309), 1-23, http://dx.doi.org/10.1029/2004JB003167

Lee, D.-C., J. V. Olson, and C. A. L. Szuberla (2013), Computationally robust and noise resistant numerical detector for the detection of atmospheric infrasound, *J. Acoust. Soc. Am.*, *134*(1), 862-868, http://dx.doi.org/10.1121/1.4807802

Lyons, J. J., M. M. Haney, D. Fee, and J. F. Paskievitch (2014), Distinguishing high surf from volcanic long-period earthquakes, *Geophysical Research Letters*, http://dx.doi.org/10.1002/2013GL058954

Lyons, J. J., M. M. Haney, C. Werner, P. Kelly, M. Patrick, C. Kern, and F. Trusdell (2016), Long period seismicity and very long period infrasound driven by shallow magmatic degassing at Mount Pagan, Mariana Islands, *J. Geophys. Res. Solid Earth*, *121*(1), 188-209, http://dx.doi.org/10.1002/2015JB012490

Madshus, C., F. Løvholt, A. Kaynia, L. Hole, K. Attenborough, and S. Taherzadeh (2005), Air-ground interaction in long range propagation of low frequency sound and vibration-field tests and model verification, *Applied acoustics*, *66*(5), http://dx.doi.org/10.1016/j.apacoust.2004.09.006

Matoza, R. S., and D. Fee (2014), Infrasonic component of volcano-seismic eruption tremor, *Geophysical Research Letters*, *41*(6), 1964-1970, http://dx.doi.org/10.1002/2014GL059301

Matoza, R. S., M. A. Garcés, B. A. Chouet, L. D'Auria, M. A. H. Hedlin, C. De Groot Hedlin, and G. P. Waite (2009), The source of infrasound associated with long - period events at Mount St. Helens, *J. Geophys. Res. Solid Earth*, *114*(B4), B04305, http://dx.doi.org/10.1029/2008JB006128

Matoza, R. S., M. A. H. Hedlin, and M. A. Garcés (2007), An infrasound array study of Mount St. Helens, *Journal of Volcanology and Geothermal Research*, *160*(3-4), 249-262, http://dx.doi.org/10.1016/j.jvolgeores.2006.10.006

Matoza, R. S., A. Le Pichon, J. Vergoz, P. Herry, J.-M. Lalande, H.-i. Lee, I.-Y. Che, and A. Rybin (2011), Infrasonic observations of the June 2009 Sarychev Peak eruption, Kuril Islands: Implications for infrasonic monitoring of remote explosive volcanism, *Journal of Volcanology and Geothermal Research*, *200*(1-2), 35-48, http://dx.doi.org/10.1016/j.jvolgeores.2010.11.022

Montalbetti, J. F., and E. R. Kanasewich (1970), Enhancement of Teleseismic Body Phases with a Polarization Filter, *Geophysical Journal of the Royal Astronomical Society*, *21*, 119-129,

Neuberg, J., and T. Pointer (2000), Effects of volcano topography on seismic broad-band waveforms, *Geophysical Journal International*, *143*(1), 239-248, http://dx.doi.org/10.1046/j.1365-246x.2000.00251.x

Olson, J. V., and C. A. Szuberla (2008), Processing Infrasonic Array Data, in *Handbook of Signal Processing in Acoustics*, edited by D. Havelock, S. Kuwano and M. Vorlander, pp. 1487-1496, Springer, New York, NY,

Olson, J. V., and C. A. L. Szuberla (2005), Distribution of wave packet sizes in microbarom wave trains observed in Alaska, *J. Acoust. Soc. Am.*, *117*(3), 1032-1036, http://dx.doi.org/10.1121/1.1854651

Shields, D. F. (2005), Low-frequency wind noise correlation in microphone arrays, *The Journal of the Acoustical Society of America*, *117*(6), http://dx.doi.org/10.1121/1.1879252

Smart, E., and E. A. Flinn (1971), Fast Frequency-Wavenumber Analysis and Fisher Signal Detection in Real-Time Infrasonic Array Data Processing, *Geophysical Journal International*, *26*(1-4), 279-284, http://dx.doi.org/10.1111/j.1365-246X.1971.tb03401.x

Smith, C. M., S. R. McNutt, and G. Thompson (2016), Ground-coupled airwaves at Pavlof Volcano, Alaska, and their potential for eruption monitoring, *Bulletin of Volcanology*, *78*(52), 1-12, http://dx.doi.org/10.1007/s00445-016-1045-0

Tauzin, B., E. Debayle, C. Quantin, and N. Coltice (2013), Seismoacoustic coupling induced by the breakup of the 15 February 2013 Chelyabinsk meteor, *Geophys. Res. Lett.*, *40*(14), 3522-3526, http://dx.doi.org/10.1002/grl.50683

Thelen, W. A., and J. Cooper (2015), An analysis of three new infrasound arrays around Kīlauea Volcano*Rep. 2014-1253*.

Vidale, J. E. (1986), Complex polarization analysis of particle motion, *Bulletin of the Seismological society of America*, *76*(5), 1393-1405,

Walker, K. T., M. A. H. Hedlin, C. De Groot Hedlin, J. Vergoz, A. Le Pichon, and D. P. Drob (2010), Source location of the 19 February 2008 Oregon bolide using seismic networks and infrasound arrays, *Journal of Geophysical Research*, *115*(B12329), 1-17, http://dx.doi.org/10.1029/2010JB007863

Wang, H., and M. Kaveh (1985), Coherent signal-subspace processing for the detection and estimation of angles of arrival of multiple wide-band sources, *IEEE Transactions on Acoustics, Speech, and Signal Processing*, *33*(4), 823-831, http://dx.doi.org/10.1109/TASSP.1985.1164667

Wilson, K. D., R. J. Greenfield, and M. J. White (2007), Spatial structure of low-frequency wind noise, *The Journal of the Acoustical Society of America*, *122*(6), http://dx.doi.org/10.1121/1.2786608

Chapter 5

General Conclusion

Acoustics is "the science of the production, transmission, and effects of sound" (Parker, 1994). In turn, volcano infrasound is the science of the production (source), transmission (path), and effects of low frequency sound from volcanoes. The details of the prior chapters show how we have advanced the field by adding knowledge and a new tool focused in the production and transmission of volcano infrasound. In the work at Sakurajima Volcano Japan, we evaluated the effectiveness of the semblance source location method in the presence of significant topographic features and found the results to be consistently offset from the actual source locations by ~420 m. From this we know topography needs to be accounted for when performing infrasonic source location. We show that even in the presence of large obstructions, semblance can be a useful tool for determining time of volcanic activity.

Next, we investigated an acoustic source that had yet to be characterized in detail, a gas-jetting fumarole, at an observation angle not usually feasible, 56.7° from vertical. This was of value as vigorous fumaroles have been observed to make sounds similar to jet noise. We found the ~2.5 m fumarole in the floor of Naka-dake crater of Aso Volcano, Japan to have time series and spectral characteristics akin to jet noise. A jet noise source is of interest to the volcano infrasound community as large volcanic eruptions have been observed to have infrasonic spectral characteristics similar to jet noise from jet and rocket engines and laboratory jets (Matoza et al., 2009; Matoza et al., 2013). This similarity between volcanic and manufactured jet noise spectra is potentially useful, as jet noise has been extensively studied with empirical equations derived relating jet parameters to jet noise (Tam, 1998). With the fumarole acoustic characteristics, we then used thermal images to measure the jet temperature and estimate the jet diameter and an assumed Strouhal number to estimate the jet's velocity, ~79 – 132 m/s. From the estimated jet velocity and diameter, along with published gas data, we estimated the volatile flux. These estimates allowed us to put a gas-jetting fumarole in the broader context of other observed or simulated volcanic jets and similar volcanic environments. This work suggested that gas-jetting fumaroles are a reasonable analog to study to better understand large volcanic eruption, but that local topography should be taken into account using more detailed modeling.

Finally, we developed a new, minimalist technique to determine the back-azimuth to an acoustic source using a single infrasound sensor and a 3-component seismometer that takes advantage of a phenomenon that occurs along an acoustic wave's path, a ground-coupled airwave. We utilize the additional phase, as it will be different depending on the back-azimuth of the incident airwave, and the particle motion from the 3-component seismic data to determine a unique back-azimuth. The results from synthetic and well-constrained volcanic sources are within <1° - 5° of the actual and traditional array processing determined back-azimuths. Our new technique could be particularly useful where resources are limited and where seismo-acoustic sensor pairs are already deployed.

Through the research detailed in this dissertation, we have improved our understanding of the applicability of the semblance source location method; characterized a gas-jetting fumarole, and related it to large, volcanic eruptions; and developed a new technique to determine the back-azimuth to an acoustic source using a single seismo-acoustic pair. This research has thus added to our knowledge of volcano infrasound production and transmission.

Chapter 6

Future Work

The general goals of volcano observatories are to detect and characterize volcanic unrest, determine likelihood and size of eruption, and inform public agencies to mitigate the expected hazard. Volcano observatories use a variety of geophysical techniques to monitor volcanoes in near-real time to mitigate the threats volcanoes pose to local and global communities. Subsurface changes are primarily detected using seismometers, continuous GPS, tiltmeters, local gas sensors and sampling, and satellite remote sensing. An increase in subsurface fluid (i.e. magma and volatiles), pressure or temperature can result in increased seismicity, ground deformation and an increase or change in volatile content. Complementing these observational methods, infrasound-sensitive microphones detect subaerial volcanic activity from gas jetting to explosions. As each of the chapters has its respective recommendations and future work, here I describe the future work I will conduct for my postdoctoral fellowship. The aim of my postdoctoral project is to examine the short- and long-term volatile budgets of basaltic volcanic systems by comparing shallow volume input from broadband, tilt-affected seismic data with volume output from infrasound and gas data at Stromboli Volcano, Italy. Linking subsurface to subaerial processes will be particularly helpful for hazard mitigation as we can better constrain expected volatile output from monitored volume input. Three-component, broadband seismometers are sensitive to tilt (Aoyama and Oshima, 2008). As such, we will deploy a seismo-acoustic network and gas measurement instruments (MultiGas, UV camera, and Fourier-transform infrared spectroscopy) at Stromboli Volcano, Italy in summer 2018. Basic questions still exist in volcano monitoring; such as do larger tilt amplitudes result in larger peak infrasound amplitudes and volatile flux? This is a significant question to answer as it relates volcano-monitoring observations to quantifiable hazards. A quantitative comparison and integration of estimated volumes from infrasound and tilt data has not been done before. For the few studies that compare tilt and infrasound data, the investigations usually do not extend beyond evaluating an explosion's sequence of events (Iguchi et al., 2008; Yokoo et al., 2013).

Recent advancements in infrasonic (Kim and Lees, 2014; Kim et al., 2015; Fee et al., 2017) and seismic (Tape and Tape, 2012; Waite and Lanza, 2016) waveform inversions show that quantification and comparison of subaerial and subsurface processes is feasible. As such, we will

utilize seismic, infrasound and gas observations to quantify volatile volume input and output for small explosions (10s to 100s of meters above the vent) at Stromboli Volcano, Italy. Infrasound determined volume flux is incorporated in this study of volatiles, as it is robust to environmental changes (e.g. clouds, lack of daylight, and plume direction change from light wind) that can hinder gas detection methods. The project objectives are: (1) determine the relationship between seismic-derived tilt and infrasound data; (2) conduct independent tilt-affected seismic and infrasonic waveform inversions to characterize the respective sources (Kim et al., 2015; Waite and Lanza, 2016); (3) compare tilt-derived volume input to infrasound waveform inversion and gas flux volume outputs. Through meeting these objectives we aim to advance our ability to determine the size of eruption prior to its occurrence by quantitatively examining tilt infrasound and gas data.

Chapter 7

General References

Aoyama, H. and Oshima, H., 2008. Tilt change recorded by broadband seismometer prior to small phreatic explosion of Meakan-dake volcano, Hokkaido, Japan. Geophysical Research Letters, 35(L06307): 1-7. 10.1029/2007GL032988

Asimow, P.D., 2000. Melting the Mantle. In: H. Sigurdsson (Editor), Encyclopedia of Volcanoes. Academic Press, San Diego, CA, pp. 55-68.

Ben-Menahem, A. and Singh, S.J., 2000. Seismic Waves and Sources. Springer, New York.

Blackburn, E.A., Wilson, L. and Sparks, R.S.J., 1976. Mechanisms and dynamics of strombolian activity. journal of the Geological Society, 132: 429-440. https://doi.org/10.1144/gsjgs.132.4.0429

Buckingham, M.J. and Garcés, M.A., 1996. Canonical model of volcano acoustics. J. Geophys. Res., 101(B4): 8129-8151. http://dx.doi.org/10.1029/95JB01680

Carey, S. and Bursik, M., 2000. Volcanic Plumes. In: H. Sigurdsson (Editor), Encyclopedia of Volcanoes. Academic Press, San Diego, CA, pp. 527-544.

Cashman, K.V., Sturtevant, B., Papale, P. and Navon, O., 2000. Magmatic Fragmentation. In: H. Sigurdsson (Editor), Encyclopedia of Volcanoes. Academic Press, San Diego, CA, pp. 421-430.

Cerminara, M., Esposti Ongaro, T. and Neri, A., 2016. Large Eddy Simulation of gas-particle kinematic decoupling and turbulent entrainment in volcanic plumes. Journal of Volcanology and Geothermal Research: 1-29. doi: 10.1016/j.jvolgeores.2016.06.018

Chouet, B.A., 1996. Long-period volcano seismicity: its source and use in eruption forecasting. Nature, 380: 309-316. http://dx.doi.org/10.1038/380309a0

Chouet, B.A. and Matoza, R.S., 2013. A multi-decadal view of seismic methods for detecting precursors of magma movement and eruption. Journal of Volcanology and Geothermal Research, 252: 108-175. http://dx.doi.org/10.1016/j.jvolgeores.2012.11.013

Cioni, R., Marianelli, P., Santacroce, R. and Sbrana, A., 2000. Plinian and Subplinian Eruptions. In: H. Sigurdsson (Editor), Encyclopedia of Volcanoes. Academic Press, San Diego, CA, pp. 477-494.

Cowan, J., 2014. Building Acoustics. In: T.D. Rossing (Editor), Springer Handbook of Acoustics. Springer, Berlin, pp. 403-442.

De Angelis, S., Fee, D., Haney, M. and Schneider, D., 2012. Detecting hidden volcanic explosions from Mt. Cleveland Volcano, Alaska with infrasound and ground-coupled airwaves. Geophysical Research Letters, 39(L21312). http://dx.doi.org/10.1029/2012gl053635

Edwards, W.N., Eaton, D.W., McCausland, P.J., ReVelle, D.O. and Brown, P.G., 2007. Calibrating infrasonic to seismic coupling using the Stardust sample return capsule shockwave: Implications for seismic observations of meteors. Journal of Geophysical Research: Solid Earth (1978–2012), 112(B10306): 1-13. http://dx.doi.org/10.1029/2006JB004621

Fee, D., Garcés, M., Orr, T. and Poland, M., 2011. Infrasound from the 2007 fissure eruptions of Kīlauea Volcano, Hawai'i. Geophys. Res. Lett., 38(L06309): 1-5. 10.1029/2010GL046422

Fee, D., Garces, M. and Steffke, A., 2010a. Infrasound from Tungurahua Volcano 2006–2008: Strombolian to Plinian eruptive activity. Journal of Volcanology and Geothermal Research, 193(1-2): 67-81. http://dx.doi.org/10.1016/j.jvolgeores.2010.03.006

Fee, D., Haney, M.M., Matoza, R., Szuberla, C.A.L., Lyons, J. and Waythomas, C., 2016. Seismic Envelope ‐ Based Detection and Location of Ground ‐ Coupled Airwaves from Volcanoes in Alaska. Bulletin of the Seismological Society of America, 106(3): 1024-1035. http://dx.doi.org/10.1785/0120150244

Fee, D., Izbekov, P., Kim, K., Yokoo, A., Lopez, T.M., Prata, F., Kazahaya, R., Nakamichi, H. and Iguchi, M., 2017. Eruption mass estimation using infrasound waveform inversion and ash and gas measurements: Evaluation at Sakurajima Volcano, Japan. Earth and Planetary Science Letters, 480: 42-52. 10.1016/j.epsl.2017.09.043

Fee, D. and Matoza, R.S., 2013. An overview of volcano infrasound: From hawaiian to plinian, local to global. Journal of Volcanology and Geothermal Research, 249: 123-139. http://dx.doi.org/10.1016/j.jvolgeores.2012.09.002

Fee, D., Matoza, R.S., Gee, K.L., Neilsen, T.B. and Ogden, D.E., 2013a. Infrasonic crackle and supersonic jet noise from the eruption of Nabro Volcano, Eritrea. Geophysical Research Letters, 40(16): 4199-4203. http://dx.doi.org/10.1002/grl.50827

Fee, D., McNutt, S.R., Lopez, T.M., Arnoult, K.M., Szuberla, C.A.L. and Olson, J.V., 2013b. Combining local and remote infrasound recordings from the 2009 Redoubt Volcano eruption. Journal of Volcanology and Geothermal Research, 259(C): 100-114. http://dx.doi.org/10.1016/j.jvolgeores.2011.09.012

Fee, D., Steffke, A. and Garces, M., 2010b. Characterization of the 2008 Kasatochi and Okmok eruptions using remote infrasound arrays. Journal of Geophysical Research, 115. http://dx.doi.org/10.1029/2009jd013621

Gonnermann, H.M. and Manga, M., 2007. The Fluid Mechanics Inside a Volcano. Annu. Rev. Fluid Mech., 39(1): 321-356. 10.1146/annurev.fluid.39.050905.110207

Head, J.W. and Wilson, L., 1989. Basaltic pyroclastic eruptions: Influence of gas-release patterns and volume fluxes on fountain structure, and the formation of cinder cones, spatter cones, rootless flows, lava ponds and lava flows. Journal of Volcanology and Geothermal Research, 37(3-4): 261-271. https://doi.org/10.1016/0377-0273(89)90083-8

Ichihara, M., Takeo, M., Yokoo, A., Oikawa, J. and Ohminato, T., 2012. Monitoring volcanic activity using correlation patterns between infrasound and ground motion. Geophysical Research Letters, 39(L04304): 1-5. http://dx.doi.org/10.1029/2011gl050542

Iguchi, M., Yakiwara, H., Tameguri, T., Hendrasto, M. and Hirabayashi, J.-i., 2008. Mechanism of explosive eruption revealed by geophysical observations at the Sakurajima, Suwanosejima and Semeru volcanoes. Journal of Volcanology and Geothermal Research, 178: 1-9. 10.1016/j.jvolgeores.2007.10.010

Kim, K., Fee, D., Yokoo, A. and Lees, J.M., 2015. Acoustic source inversion to estimate volume flux from volcanic explosions. Geophysical Research Letters, 42(13): 5243-5249. doi: 10.1002/2015GL064466

Kim, K. and Lees, J., 2014. Local Volcano Infrasound and Source Localization Investigated by 3D Simulation. Seismological Research Letters. doi: 10.1785/0220140029

Kim, K. and Lees, J.M., 2011. Finite-difference time-domain modeling of transient infrasonic wavefields excited by volcanic explosions. Geophysical Research Letters, 38(L06804). doi: 10.1029/2010gl046615

Kim, K., Lees, J.M. and Ruiz, M., 2012. Acoustic multipole source model for volcanic explosions and inversion for source parameters. Geophysical Journal International, 191: 1192-1204. doi: 10.1111/j.1365-246X.2012.05696.x

Lacanna, G. and Ripepe, M., 2013. Influence of near-source volcano topography on the acoustic wavefield and implication for source modeling. Journal of Volcanology and Geothermal Research, 250: 9-18. doi: 10.1016/j.jvolgeores.2012.10.005

Lighthill, M.J., 1952. On sound generated aerodynamically. I. General theory. Proceedings of the Royal Society of London A: Mathematical, Physical and Engineering Sciences, 211(1107): 564-587. 10.1098/rspa.1952.0060

Lighthill, M.J., 1963. Jet noise. Aiaa J, 1(7): 1507-1517. 10.2514/3.1848

Matoza, R.S., Fee, D., Garcés, M.A., Seiner, J.M., Ramón, P.A. and Hedlin, M.A.H., 2009. Infrasonic jet noise from volcanic eruptions. Geophysical Research Letters, 36(8). doi: 10.1029/2008gl036486

Matoza, R.S., Fee, D., Neilsen, T.B., Gee, K.L. and Ogden, D.E., 2013. Aeroacoustics of volcanic jets: Acoustic power estimation and jet velocity dependence. Journal of Geophysical Research, 118: 6269–6284. doi: 10.1002/2013JB010303

Matoza, R.S., Green, D.N., Le Pichon, A., Shearer, P.M., Fee, D., Mialle, P. and Ceranna, L., 2017. Automated detection and cataloging of global explosive volcanism using the International Monitoring System infrasound network. J. Geophys. Res. Solid Earth, 122(4): 2946-2971. 10.1002/2016JB013356

Morrissey, M.M. and Mastin, L.G., 2000. Vulcanian Eruptions. In: H. Sigurdsson (Editor), Encyclopedia of Volcanoes. Academic Press, San Diego, CA, pp. 463-475.

Parfitt, E.A. and Wilson, L., 2008. Fundamentals of Physical Volcanology. Blackwell Publishing, Malden, MA.

Parker, S.P., 1994. McGraw-Hill dictionary of scientific and technical terms. In: S.P. Parker (Editor), New York, NY.

Perfit, M.R. and Davidson, J.P., 2000. Plate tectonics and Volcanism. In: H. Sigurdsson (Editor), Encyclopedia of Volcanoes. Academic Press, San Diego, CA, pp. 89-113.

Pierce, A.D., 2014. Basic Linear Acoustics. In: T.D. Rossing (Editor), Springer Handbook of Acoustics. Springer, Berlin, pp. 29-115.

Pyle, D.M., 2000. Sizes of volcanic eruptions. In: H. Sigurdsson (Editor), Encyclopedia of Volcanoes. Academic Press, San Diego, CA, pp. 263-269.

Rossing, T.D., 2014. Introduction to Acoustics. In: T.D. Rossing (Editor), Springer Handbook of Acoustics. Springer, Berlin, pp. 1-7.

Russell, D.A., Titlow, J.P. and Bemmen, Y.-J., 1999. Acoustic monopoles, dipoles, and quadrupoles: An experiment revisited. Am. J. Phys., 67(8): 660-664. 10.1119/1.19349

Sparks, R.S.J., 1978. The dynamics of bubble formation and growth in magmas: a review and analysis. Journal of Volcanology and Geothermal Research, 3(1-2): 1-37. https://doi.org/10.1016/0377-0273(78)90002-1

Stein, S. and Wysession, M.E., 2003. An Introduction to Seismology, Earthquakes, and Earth Structure. Blackwell Publishing, Malden, MA.

Taddeucci, J., Sesterhenn, J., Scarlato, P., Stampka, K., Del Bello, E., Fernandez, J.J.P. and Gaudin, D., 2014. High-speed imaging, acoustic features, and aeroacoustic computations of jet noise from Strombolian (and Vulcanian) explosions. Geophysical Research Letters, 41(9): 3096-3102. doi: 10.1002/2014GL059925

Tam, C.K.W., 1995. Supersonic Jet Noise. Annu Rev Fluid Mech, 27: 17-43. doi: 10.1146/Annurev.Fl.27.010195.000313

Tam, C.K.W., 1998. Jet Noise: Since 1952. Theoretical and Computational Fluid Dynamics, 10: 393-405. doi: 10.1007/s001620050072

Tam, C.K.W. and Burton, D.E., 1984. Sound Generated by Instability Waves of Supersonic Flows .1. Two-Dimensional Mixing Layers. J Fluid Mech, 138(Jan): 249-271. doi: 10.1017/S0022112084000112

Tam, C.K.W. and Chen, P., 1994. Turbulent Mixing Noise from Supersonic Jets. Aiaa J, 32(9): 1774-1780. doi: 10.2514/3.12173

Tam, C.K.W., Golebiowski, M. and Seiner, J.M., 1996. On the Two Components of Turbulent Mixing Noise from Supersonic Jets. Aiaa J: 1-19. doi: 10.2514/6.1996-1716

Tam, C.K.W., Viswanathan, K., Ahuja, K.K. and Panda, J., 2008. The sources of jet noise: experimental evidence. J Fluid Mech, 615: 253-292. doi: 10.1017/S0022112008003704

Tape, W. and Tape, C., 2012. A geometric setting for moment tensors. Geophysical Journal International, 190(1): 476-498. 10.1111/j.1365-246X.2012.05491.x

Tauzin, B., Debayle, E., Quantin, C. and Coltice, N., 2013. Seismoacoustic coupling induced by the breakup of the 15 February 2013 Chelyabinsk meteor. Geophys. Res. Lett., 40(14): 3522-3526. http://dx.doi.org/10.1002/grl.50683

Vergniolle, S. and Mangan, M., 2000. Hawaiian and Strombolian Eruptions. In: H. Sigurdsson (Editor), Encyclopedia of Volcanoes. Academic Press, San Diego, CA, pp. 447-461.

Waite, G.P. and Lanza, F., 2016. Nonlinear inversion of tilt-affected very long period records of explosive eruptions at Fuego volcano. J. Geophys. Res. Solid Earth, 121(10): 7284-7297. 10.1002/2016JB013287

Woulff, G. and McGetchin, T.R., 1976. Acoustic Noise from Volcanoes: Theory and Experiment. Geophysical Journal of Research, 45: 601-616. doi: 10.1111/j.1365-246X.1958.tb05346.x

Yokoo, A., Iguchi, M., Tameguri, T. and Yamamoto, K., 2013. Processes Prior to Outbursts of Vulcanian Eruption at Showa Crater of Sakurajima Volcano. Bulletin of the Volcanological Society of Japan, 58(1): 163-181. 10.18940/kazan.58.1_163

Appendix

The following statements are from coauthors, which are not committee members, granting permission for including published and submitted manuscripts in this dissertation.

UNIVERSITY of ALASKA

Kathleen McKee <kfmckee@alaska.edu>

permission

Colin Rowell <rowell.colinr@gmail.com> Tue, Nov 7, 2017 at 10:11 AM

To: Kathleen McKee <kfmckee@alaska.edu>

To Kathleen, her PhD Committee, and the UAF graduate school:

I, Colin Rowell, heartily, happily, and without reservation, give permission to Kathleen McKee to use the following paper in her dissertation for which I am a coauthor.

McKee, K., D. Fee, C. Rowell, and A. Yokoo (2014), Network-based evaluation of the infrasonic source location at Sakurajima Volcano, Japan, *Seismological Research Letters*, *85*(6), 1200-1211, https://doi.org/10.1785/0220140119

Regards,
Colin

Congrats, tip o' the hat and whatnot, hope I can get an electronic copy to peruse sometime :)
[Quoted text hidden]

--
Colin Rowell
PhD Student, Geophysics
Dept. Earth, Ocean, and Atmospheric Sciences
University of British Columba
crowell@eoas.ubc.ca

UNIVERSITY of ALASKA

Kathleen McKee <kfmckee@alaska.edu>

permission

Akihiko Yokoo <yokoo.akihiko.5a@kyoto-u.ac.jp> Tue, Nov 7, 2017 at 4:16 PM

To: Kathleen McKee <kfmckee@alaska.edu>
Cc: David Fee <dfee1@alaska.edu>

Congratulation Kathleen! I believe that a brilliant future lies before you.
Thank you,
Yokoo

To whom it may concern,

I, Akihiko Yokoo, give permission to Kathleen McKee to use the following papers in her dissertation for which I am a coauthor.

McKee, K., D. Fee, C. Rowell, and A. Yokoo (2014), Network-based evaluation of the infrasonic source location at Sakurajima Volcano, Japan, Seismological Research Letters, 85(6), 1200-1211, https://doi.org/10.1785/0220140119
McKee, K., D. Fee, A. Yokoo, R. S. Matoza, and K. Kim (2017), Analysis of gas jetting and fumarole acoustics at Aso Volcano, Japan, Journal of Volcanology and Geothermal Research, 340, 16-29, https://doi.org/10.1016/j.jvolgeores.2017.03.029

Regards,
Yokoo

> 2017/11/08 4:03、Kathleen McKee <kfmckee@alaska.edu> のメール：
[Quoted text hidden]

UNIVERSITY of ALASKA

Kathleen McKee <kfmckee@alaska.edu>

Permission

Robin Matoza <rmatoza@ucsb.edu> Tue, Nov 7, 2017 at 12:04 PM
To: Kathleen McKee <kfmckee@alaska.edu>
Cc: David Fee <dfee1@alaska.edu>

To whom it may concern,

I, Robin Matoza, give permission to Kathleen McKee to use the following papers (on which I am a co-author) in her dissertation:

McKee, K., D. Fee, A. Yokoo, R. S. Matoza, and K. Kim (2017), Analysis of gas jetting and fumarole acoustics at Aso Volcano, Japan, Journal of Volcanology and Geothermal Research, 340, 16-29, https://doi.org/10.1016/j.jvolgeores.2017.03.029

McKee, K., D. Fee, M. Haney, R. S. Matoza, and J. J. Lyons, (submitted), Infrasound signal detection and back-azimuth estimation using ground-coupled airwaves on a seismo-acoustic sensor pair, Journal of Geophysical Research: Solid Earth

Please do not hesitate to contact me if I can provide any further information.

Sincerely,
Robin

--
Robin Samuel Matoza
Assistant Professor
Department of Earth Science
University of California, Santa Barbara
Phone: +1 (805) 893-3452
http://www.geol.ucsb.edu/faculty/matoza

UNIVERSITY of ALASKA

Kathleen McKee <kfmckee@alaska.edu>

permission to include journal article in dissertation

Lyons, John <jlyons@usgs.gov> Tue, Nov 7, 2017 at 10:16 AM
To: Kathleen McKee <kfmckee@alaska.edu>

To whom it may concern,

I, John Lyons, give permission to Kathleen McKee to use the following paper in her dissertation for which I am a coauthor.

McKee, K., D. Fee, M. Haney, R. S. Matoza, and J. J. Lyons, (submitted), Infrasound signal detection and back-azimuth estimation using ground-coupled airwaves on a seismo-acoustic sensor pair, Journal of Geophysical Research: Solid Earth

Regards,
John

--

John J. Lyons
Research Geophysicist
U.S. Geological Survey
Alaska Volcano Observatory
Anchorage, AK 99508
Tel.: 907-786-7422
Fax: 907-786-7425
Email: jlyons@usgs.gov
ORCID: 0000-0001-5409-1698
